Global and Planetary Change 219 (2022) 103983

Contents lists available at ScienceDirect

Global and Planetary Change

journal homepage: www.elsevier.com/locate/gloplacha

Research Article

Eocene to middle Miocene contourite deposits in Cyprus: A record of Indian Gateway evolution

F.J. Hernández-Molina [a,*], H. Hüneke [b], F.J. Rodríguez-Tovar [c], Z.L. Ng [a], E. Llave [d], A. Mena [e], A. Gibb [b], D. Chiarella [a], S. Sammartino [f], A. de la Vara [g]

[a] Dept. Earth Sciences, Royal Holloway University London, Egham, Surrey TW20 0EX, UK
[b] Institut für Geographie und Geologie, Universität Greifswald, D-17487 Greifswald, Germany
[c] Departamento de Estratigrafía y Paleontología, Universidad de Granada, 18002 Granada, Spain
[d] Instituto Geológico y Minero de España, 28003 Madrid, Spain
[e] Dpto. Xeociencias Mariñas e O.T., Universidade de Vigo, 36310 Vigo, Spain
[f] Physical Oceanography Group - Oceanic Engineering Institute, University of Málaga, Campus de Teatinos s/n, 29071 Málaga, Spain
[g] Senior Europa S.L.–Kveloce I + D + i: Plaza de la Reina 19, Escalera A, 1°, 46003, Valencia, Spain

ARTICLE INFO

Editor: Dr. Fabienne Marret-Davies

Keywords:
Deep-marine sedimentation
Bottom currents
Contourites
Cenozoic
Cyprus
Indian Gateway

ABSTRACT

Bottom current deposits (contourites) form in association with modern-day or ancient oceanic gateways. A paucity of examples in the ancient record and the lack of consensus on diagnostic criteria for differentiating them from other deepwater deposits limit our understanding of how they may record past global oceanic circulation, tectonic events and gateway evolution. This work describes an exceptional example of Eocene to middle Miocene deep-marine deposits located both onshore and offshore deepwater environments around the island of Cyprus. Multidisciplinary approaches were used to discriminate contourite facies associations, propose a sedimentary model, and interpret the relations with regional tectonics and the evolution of the nearby Indian Gateway. Contourite deposits appear in late Eocene to middle Miocene intervals interstratified with pelagic/hemipelagic sediments, turbidites and mass-transport deposits (MTDs). These deepwater deposits developed along a slope basin located on the upper plate of an active margin, evolving from a wide basin formed during a period of tectonic quiescent into a series of shallowing-upward, segmented sub-basins affected by compressional stress. The present study proposes a sedimentary model in which two contourite depositional systems developed: first in the Eocene (dominated by finer-grained contourites), and then during the latest Oligocene to middle Miocene (dominated by coarser-grained contourites). Both systems were buried by extensive marl deposits and record the respective influence of deep (circulating NW) and intermediate (circulating SE) water masses. The long-term evolution of the contourites reflects tectonic events that enhanced subduction processes south of Cyprus as well as exchange between the Neotethys Ocean and the Indian and Atlantic Oceans —until the final closure of the Indian Gateway by the end of the middle Miocene, when a new circulation pattern was established with the formation of the Mediterranean Sea.

The contourites described here represent bi-gradational sequences that normally form in association with contouritic drifts, sometimes having the asymmetric top-cut sequence characteristics of plastered drifts and contourite terraces. The coarser (sandy) contourites, formed from the latest Oligocene to middle Miocene, consist of three packages associated with compressive and flexural phases. They pertain to I) Chattian (late Oligocene); II) Aquitanian/Burdigalian (early Miocene) and III) Langhian (middle Miocene). Evidence of enhanced bottom current episodes occurs toward the top of these packages before they are buried by later dominant marl deposits. The sandy contourites thus formed during the compressive phases, whereas the predominately finer-grained units formed during later flexural phases. The intermittent turbidites and MTDs (developed during compressional phases in combination with pelagic/hemipelagic sediments) represent the sediment supply for the contourite deposits after their winnowing and / or reworking. Our research found that the diagnostic criteria for discriminating ancient bottom current deposits from other deepwater deposits are related primarily to variations in sedimentary processes, current behaviour and its velocity, sedimentation rates and paleoenvironmental conditions. This highlights the importance of primary sedimentary structures, microfacies and ichnological

* Corresponding author.
E-mail address: javier.hernandez-molina@rhul.ac.uk (F.J. Hernández-Molina).

https://doi.org/10.1016/j.gloplacha.2022.103983
Received 21 June 2022; Received in revised form 26 October 2022; Accepted 28 October 2022
Available online 9 November 2022

features in making determinations at the sedimentary facies scale. Due to their common occurrence, sedimentary thickness (30-40 m), potential porosity and permeability, sandy contourites can form deepwater reservoirs for energy geosciences.

In summary, this work demonstrates the role of plate tectonics and oceanic gateways in driving the paleo-oceanic circulation that, in turn, controls sedimentary processes and shapes the morphology of oceanic basins and continental margins. It also allows for comparison with other present-day and ancient continental margin deposits. Future high-resolution approaches and analyses of other geological settings could help resolve the sedimentary architectures of similar deepwater systems in terms of episodic tectonic processes —involving compressive-flexural stress variations. They control the Earth's surface environment (sea-level, climate and oceanic circulation) over time by influencing sediment supply, packages of strata and types of contourite deposits.

1. Introduction

Ocean basins are connected by gateways, relatively narrow passages (e.g., Drake Passage, Strait of Gibraltar) of varying depth that control surficial, intermediate or deep-water circulation, and by extension, the spatial and temporal distribution of deep-water deposits (Kennett, 1982; Smith and Pickering, 2003; Knutz, 2008; Straume et al., 2020; Bahr et al., 2022). Gateways play a critical role in the exchange of water, heat, salt and nutrients between ocean basins and smaller sub-basins such as the Mediterranean. In the geological past, paleo-gateways governed paleo-circulation and marine basin dynamics (e.g., Indian Gateway or the Central American Seaway). Thus, the opening and deepening of gateways and paleo-gateways have strongly influenced the tectono-stratigraphic and sedimentary evolution of basins, affecting global ocean circulation, poleward temperature gradients, polar climate, exchange and vertical structure of water masses, sedimentary processes,

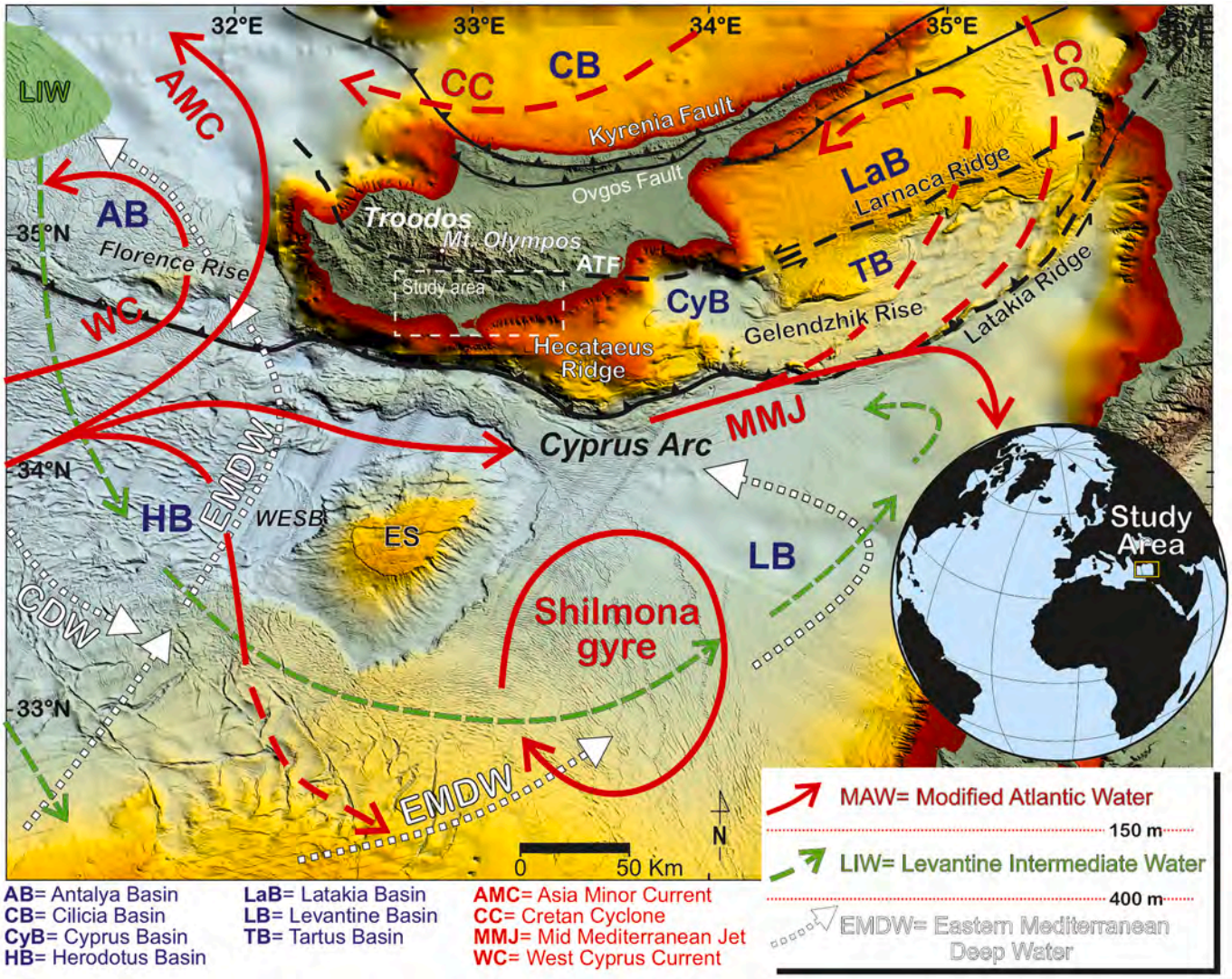

Fig. 1. Regional location of Cyprus indicating the main tectonic elements, local names and present day surface, intermediate and deepwater circulation. The white dash box indicates the onshore study area but a regional investigation offshore south of Cyprus has been also executed (*see supplementary information*). ES= Eratosthenes Seamount WESB= West Eratosthenes sub-basin. The deep waters are determined by the Eastern Mediterranean Deep Water (EMDW) or Levantine Deep Water (LDW). The EMDW consists of waters from the Adriatic Sea and Cretan Deep Water (CDW) from the Aegean Sea.

distribution of biota, and evolution/extinction events (Berggren, 1982; Zachos et al., 2001; Potter and Szatmari, 2009; Sijp et al., 2014; Straume et al., 2020; Bahr et al., 2022). Despite the significance of gateways, uncertainty persists concerning geological and oceanographic/paleoceanographic processes that occur within and around them. A better understanding of long-term tectonic controls on gateway geometry and depth could help elucidate water exchange between oceanic basins, decode geological and oceanographic processes, and establish links between environmental change and basin development.

Areas adjacent to gateways usually undergo the highest bottom current velocities (Thran et al., 2018) and thus develop pronounced bottom current (contourite) erosional and depositional features (Rebesco et al., 2014). Since the formal definition of contourites by Heezen et al. (1966), several modifications have been proposed to arrive at the current consensual definition of "sediments deposited or substantially reworked by the persistent action of bottom currents" (e.g., Stow et al., 2002a; Rebesco et al., 2014). Contourite deposits are usually interbedded with other deep-water sediment types, e.g., gravitational, hemipelagic or pelagic deposits (Stow and Smillie, 2020; de Castro et al., 2021a; de Weger et al., 2021). Their recognition and distinction mainly depends on their morphology and sedimentary stacking pattern, derived from bathymetric and seismic data. Recent research has proposed more robust diagnostic criteria for contouritic facies associations (Alonso et al., 2016; Brackenridge et al., 2018; de Castro et al., 2020, 2021a, 2021b; Stow and Smillie, 2020; Yu et al., 2020; Hüneke et al., 2021; de Weger et al., 2021).

The lack of good analogues for contourite deposits in the ancient record (Hüneke and Stow, 2008; Rebesco et al., 2014) currently poses a challenge for contourite interpretation. Such records could help constrain facies associations for different geological settings and shed light on long-term mechanistic factors behind their formation. Cenozoic deposits from Cyprus are one exception to the general lack of ancient examples (Robertson, 1976, 1977; Kähler and Stow, 1998; Stow et al., 2002b; Rodríguez-Tovar et al., 2019a, 2019b; Hüneke et al., 2021). Over the past decade, "The Drifters" Research Group at Royal Holloway University of London has executed detailed and multidisciplinary research on these deposits from Cyprus (Fig. 1). The objectives of the present research are: a) to characterise facies associations of deep-marine systems and identify contourite deposits, b) compare these deposits with other examples recognised in modern deep-marine environments and construct a sedimentary model, and c) determine why, when and how these deposits formed by assessing long-term tectonic history and the formation and evolution of the nearby Indian Gateway (IG).

2. Geological and stratigraphic settings

Cyprus, both onshore and offshore, rests within a complex tectonic area, in the broad zone of convergence between the African and Eurasian plates (Figs. 1 and 2). The Island of Cyprus lies north of the Cyprus trench, which represents the southern expression of an east-west-striking subduction zone dipping towards the north beneath Cyprus (the Cyprean Arc) and has influenced this zone since the late Cretaceous (Robertson, 1998a,b; Edwards et al., 2010; Reiche and Hübscher, 2015; Papadimitrioua et al., 2018).

Subduction of the African plate beneath the Eurasian plate, with the formation and uplift (obduction) of the Troodos Massif ophiolites, occurred during the late Cretaceous (Cyprus Geological Survey, 2005). This was followed by sea-floor spreading in a supra-subduction setting (Pearce et al., 1984) and complex juxtaposition with the Mamonia complex (Fig. 2), which ended by the Maastrichtian. Radiolarian mudstone umber (Peradehi Formation), late Campanian bentonitic clays (Kannaviou Formation) and debrites interbedded with angular clasts in a sand and clay matrix (Kathikas Formation) formed during and after this tectonic phase. The Lefkara Formation (Fm.) formed as deep-marine sediments from the latest Cretaceous to the late Oligocene (Robertson, 1976; Kähler and Stow, 1998, Fig. 2). These deposits indicate a progressive sinistral rotation of the Troodos microplate of 90° over 25 Ma from the late Cretaceous to the early Eocene (Clube and Robertson, 1986).

Gradual shallowing during the Paleocene —especially from late Oligocene (~23 Ma) to middle Miocene (15 Ma) — occurred coevally with the development of sedimentary sub-basins and with the diachronous deposition of the Pakhna Fm. (Fig. 2). This formation consists of deep- to shallow-marine deposits (including reefs) that show upward shallowing- and coarsening trends related to the uplift of Troodos Massif ophiolites. Tectonic activity involves the northward subduction of the Cyprean Arc during the Miocene collision between the African and Eurasian plates (Eaton and Robertson, 1993; Cyprus Geological Survey, 2005; Kinnaird, 2008; Edwards et al., 2010). By the end of the middle Miocene (15-10 Ma), the region underwent folding and thrusting in the north, with the emplacement of Kyrenia terrane, juxtaposition of the Troodos and Mamonia terranes in the south (Robertson, 1990), and the emergence of Troodos ophiolite (Cyprus Geological Survey, 2005, 2017; Edwards et al., 2010). The Messinian deposits (Kalavasos Fm.) regionally overlie the Pakhna Fm. and are covered by Pliocene-Quaternary deposits (Nicosia, Athalassa, Kakkaristra, Apalos and fan-conglomerate Fms.) (Robertson et al., 1991, 1995; Kinnaird, 2008; Edwards et al., 2010; Manzi et al., 2016). Abrupt and significant uplift and climatic changes at the base of the Quaternary generated erosion and deposition of the fanglomerates (Cyprus Geological Survey, 2005).

The studied sections, in southern Cyprus (Fig. 2A), correspond to the Lefkara and Pakhna Fms.; they are part of the circum-Troodos sedimentary successions (Edwards et al., 2010), currently located within the upper plate of a northward-dipping active subduction zone (Jackson and McKenzie, 1984; Eaton and Robertson, 1993).

The Lefkara Fm. is characterised by deep-marine sediments (Fig. 2) consisting of chalks, marly chalks, marls, radiolarian-rich calcilutites and cherts deposited from the late Cretaceous to Oligocene – early Miocene at a paleodepth of 2 to 3 km (Robertson, 1976; Kähler and Stow, 1998). The Lefkara Fm. is better developed to the south and east of the Troodos Massif, where it reaches up to 750 m in sedimentary thickness (Cyprus Geological Survey, 2005, 2017). This formation can be subdivided into four stratigraphic units (Gass, 1960; Robertson, 1976; Kähler and Stow, 1998). A lower marl unit features thin-bedded pinkish-grey marls and marly chalks with occasional chert nodules. It commonly fills depressions along the volcanic paleo-surface of the Troodos Massif ophiolites. This marly unit was considered by Robertson (1976) as deposited from the upper Maastrichtian to early Eocene (~67-56 Ma) but later Kähler (1994) and Kähler and Stow (1998) established it onset by the end of the Paleocene / beginning of the Eocene. A second unit (early to middle Eocene, ~56-41 Ma) has white chalks with extensive chert horizons. A third unit (middle Eocene to Oligocene and early Miocene, ~41-23 Ma) consists of massive, chert-free, white chalks that transition into marl-rich horizons. Finally, an upper marl unit (Oligocene to early Miocene) consists of grey marls and marly chalks. Previous authors report the occurrence of contourite deposits in the two younger units (Robertson, 1976; Kähler and Stow, 1998; Stow et al., 2002b). The contact between the Lefkara Fm. and the younger Pakhna Fm. varies from sharp and diachronous (conformable) to unconformable, depending upon location, and appears as a shift from white to more yellowish or lightly brownish coloured rocks (Edwards et al., 2010).

The Pakhna Fm. reaches about 350–400 m in sedimentary thickness and contains chalks, marly chalks, bioturbated silty marls to siltstones, calcarenites and conglomerate lithologies. The latter two lithologies become more dominant in the upper part of the formation (Fig. 2). The Pakhna Fm. deposition began with the onset of northward subduction beneath Cyprus (Eaton and Robertson, 1993) and the uplift of the Troodos Massif ophiolites during the Miocene, when several basins developed (Eaton and Robertson, 1993; Edwards et al., 2010; Cyprus Geological Survey, 2017). The two sub-basins in southern Cyprus —the Khalassa and Maroni sub-basins— are bound by major tectonic

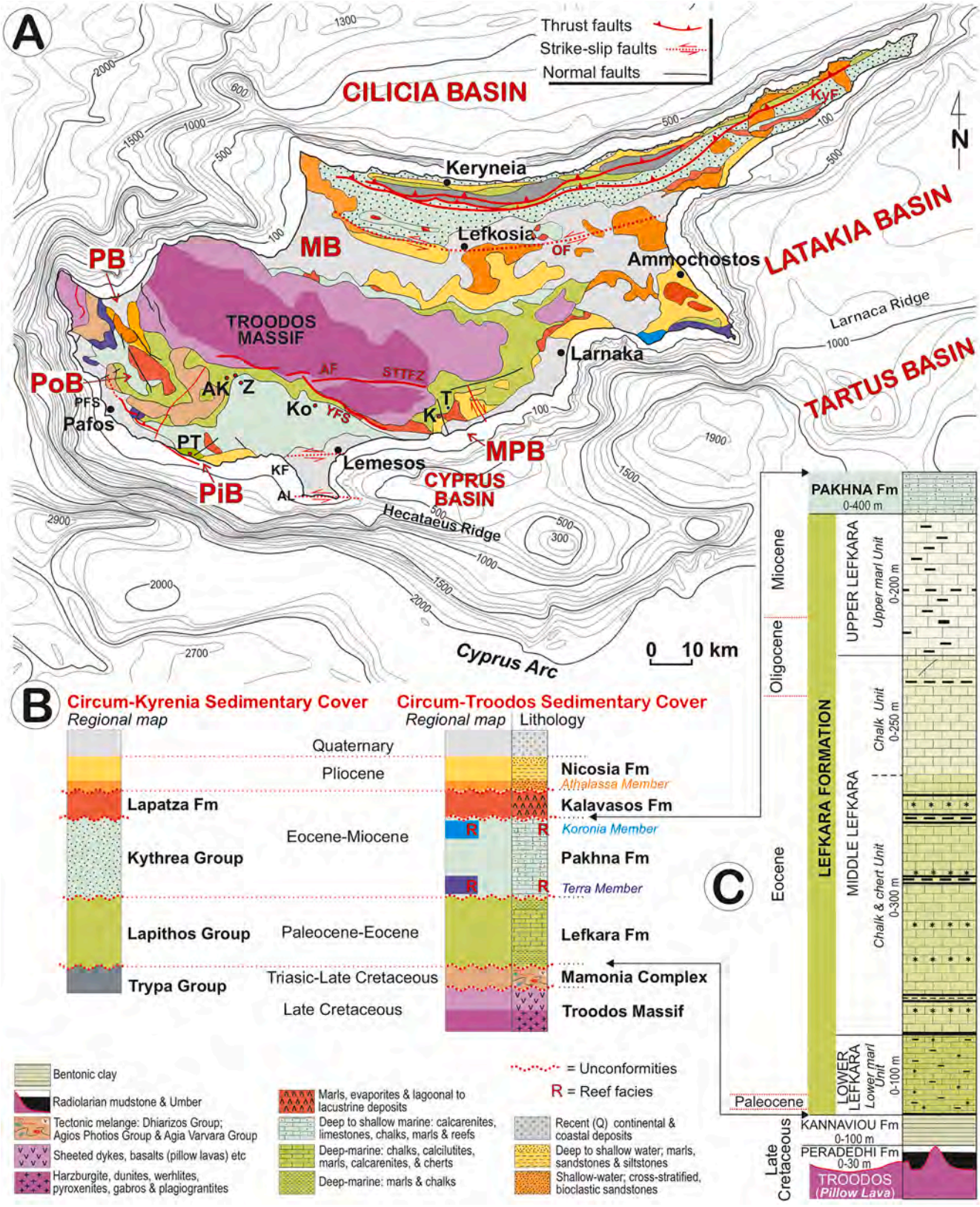

Fig. 2. A) Regional geology including the location of onshore outcrops (PT, AK, Z, Ko and K) south of the Troodos Massif. Regional seafloor bathymetry with 50 m contour intervals showing the complex morphology of the continental slope along the upper plate of the Cyprus Arc (adapted from Hall, 1994). *Studied sections:* AK= Agios Konstantinos; K= Kalavasos; Ko= Korfi; PT= Petra-Tou Romiou; Z= Zenon. *Sedimentary basin:* MB=; Mesaoria Basin; MPB=, Maroni-Psematismenos Basin; PB=; Polis Basin; PiB=, Pissouri Basin; and PoB= Polemi Basin. *Structures:* AL= Akrotiri lineament; AF= Arakapas Fault; KF= Kolossi Fault; KyF= Kythrea Fault; OF=, Ovgos Fault; PFS= Paphos Fault System; STTFZ= South Troodos Transform Fault Zone; YFS= Yerasa Fault System. *Other:* T= Tokhni. B) Regional stratigraphy of Cyprus. C) Simplified sedimentary log for the late Cretaceous to middle Miocene adapted from Robertson and Hudson (1974) and Robertson (1976) as slightly modified by Kähler and Stow (1998).

structures (Eaton and Robertson, 1993). Within this complex tectonic setting, hemipelagic sediments accumulated in basin centres; but closer to the margins, turbidites and mass transport deposits (MTDs) become more abundant. This formation is interpreted to consist of two units (Eaton and Robertson, 1993; Edwards et al., 2010). A lower unit containing marly chalk interbedded with yellowish calcarenites gradually transitions to interbedded sandstone beds with marls. The upper unit hosts thin to medium bedded chalks, marls, limestones, sandstones and siltstones. Reef facies appear at all levels, yet most commonly at the bottom (Terra Member) and top (Koronia Member) of the formation (Fig. 2), indicating shallow water environments in parts of the basin even during the early Miocene (Edwards et al., 2010; Cyprus Geological Survey, 2017).

3. Oceanographic setting

Cyprus lies in the eastern basin of the Mediterranean, in the Levantine Sea, where three main water masses are identified (Wüst, 1961; Robinson et al., 1991, 2001; Malanotte-Rizzoli et al., 1999; Millot, 1999; Kamel and Maiyza, 2000; Hamad et al., 2005; Millot and Taupier-Letage, 2005). The surface waters (Fig. 1) are Modified Atlantic Water (MAW) confined to up to 150 m water depth (wd) with salinity of 37.2-37.8 psu and temperature 15-17 °C. The Mid Mediterranean Jet (MMJ) in the Levantine area receives comparatively less salty (fresher) water influx from the MAW (Atlantic source) through the straits of Sicily and bifurcates as sub-basin-scale gyres and cores.

Intermediate water consists of Levantine Intermediate Water (LIW) flowing between 150-400 and 500 m wd (Fig. 1) with 38.73 – 38.78 psu salinity and a 15-16 °C temperature range. The LIW forms seasonally in the Levantine Basin, as winter-related convection events cause density increases through advective salinity preconditioning by the cold, saline and dense Asia Minor Current (AMC) in the northern Mediterranean around the Rhodes gyre. The LIW either circulates within the basin or as westward egress to the Atlantic through the straits of Sicily. The deep waters are determined by the Levantine Deep Water (LDW) or Eastern Mediterranean Deep Water (EMDW), which flows deeper than 400/500 m wd (Fig. 1) and shows typical salinity of 38.7 psu and temperature of 13.4 °C. The EMDW consists of waters from the Adriatic Sea and Cretan Deep Water (CDW) from the Aegean Sea. Final establishment of the present-day configuration of three main water masses (MAW, LIW and the LDW) occurred with the final closure of the Indian Gateway and the beginnings of the Mediterranean Sea in the middle Miocene (Hamon et al., 2013; de la Vara and Meijer, 2016).

4. Methodology

4.1. Field work: studied outcrops and sections

Most of the information and data presented in this paper come from field observations made in eight campaigns from 2014 to 2021. Among the range of localities visited, just four locations (Fig. 2) were studied in detail and included in this work. They are Petra Tou Romiou (PT), Agios Konstantinos [AK; which includes the Zenon (Z) outcrops], Korfi (Ko) and Kalavasos (K). The Petra Tou Romiou outcrops (34°3944.7′ / 32°3917.93′) are described in greater detail due to their exceptional preservation of the bottom current deposits, and because they are a key

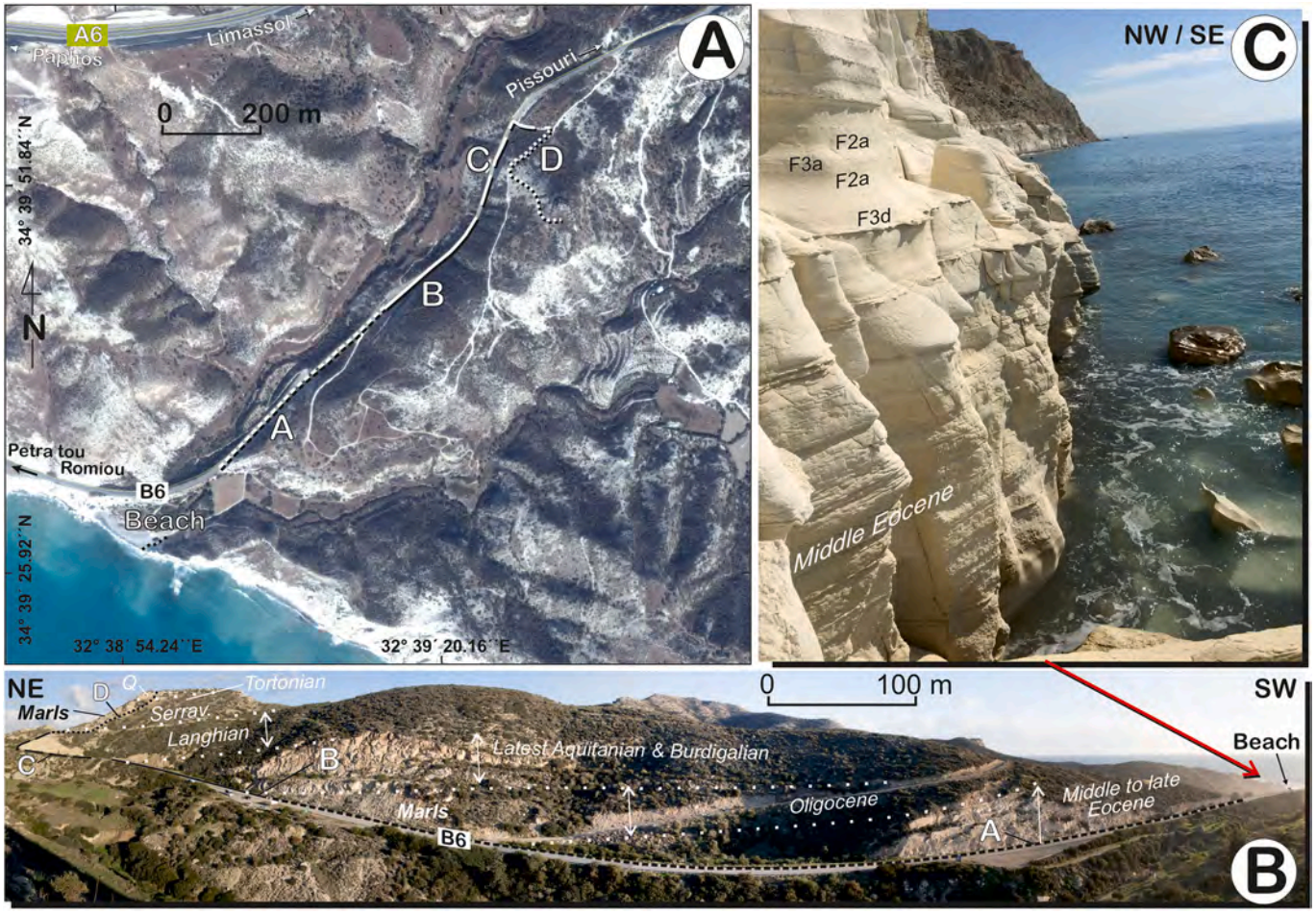

Fig. 3. A) Location for the Petra-Tou Romiou outcrops, indicating the "beach" and A through D sections. B) Panorama of the outcrops along road B6 showing the different sections, key stratigraphic boundaries and ages. C) General view of the beach section with sedimentary facies from the upper Lefkara Fm.

reference for comparison with other locations. They lie 4 km WSW of Pissuori village (Fig. 3), along road B6 towards Petra Tou Romiou (close to the Aphrodite's Rock), trending NE and consisting of five sections (Beach, A, B, C, and D). The Beach Section represents the lowest section cropping out (34°3926.79′ / 32°3856.18′), while sections A, B and C lie stratigraphically above it. Research into the Agios Konstantinos outcrop focused on two sections where both the marly deposits (Zenon section) and the overlying Pakhna Fm. (Agios Konstantinos section) are well exposed. The Zenon section occurs between Omodos and Mandria villages, just about 1.5 km N of Omodos (34°5139.81′ / 32°4826.71′); the Agios Konstantinos section is located about 1 km SE from Agios Nikolaos village (34°5111.93′ / 32°4529.99′) along road F615 in the direction to Arsos. The Korfi outcrop is situated about 1.5 km NE from Korfi village (34°4810.21N / 32°5840.24E). The Kalavasos outcrop is found about 1 km SE of Kalavasos village along the E106 road (34°4555.68′ / 33°1800.36′), trending NW and consisting of three sections (A, B, and C). Section A is located at 33°4558.67′ / 33°1758.8′. Sections B and C lie stratigraphically above the previous one, being located at 34°4552.53′ / 33°1804.24′.

Sedimentary logs of outcrops include the description of lithologies, sedimentary facies and facies associations, along with thicknesses, sedimentary structures, colour, fossils, biogenic composition and ichnological features. Textural descriptions of carbonate sedimentary rocks used the Dunham classification system (Dunham, 1962). Special attention was given to the description of diagenetic features and orientations of major structural features. Sedimentological analysis focused on sedimentary structures related to bottom currents. Cross-sets were classified following the criteria of Anastas et al. (1997). Cross-stratified and cross-laminated strata yielded 32 measurements of paleocurrent directions.

4.2. Ichnological analysis

Ichnological analysis of outcrops served to identify a number of trace fossils based on ichnological features such as shape, configuration, orientation, length, width and diameter of the burrows, burrow margins, and infill material. Samples of large, well preserved trace fossils were prepared and further analysed for cross-cutting relationships. These features allowed for ichnotaxonomy at ichnogenus and, sometimes, ichnospecies levels. Ichnological analysis was conducted on two well-differentiated spatial scales. Large-scale ichnological analysis at the outcrop focused on trace fossil assemblages and distribution of ichnological features. The relative abundance of ichnotaxa was characterized throughout the entire section, recording variations between packages of facies. Ichnological features were also analysed at meso- to small-scales bed-by-bed, documenting variations in ichnofabric features such as bioturbation degree, cross-cutting relationships, and tiering structure, among others.

4.3. Microfacies and petrographic analysis

We determined microfacies and dominant mineral components in thin-section samples from key stratigraphic horizons. Around 150 rock samples were collected for regular and large thin sections. The regular thin sections (28x48 mm; both stained and non-stained) were prepared and analysed at the Spanish Geological Survey (IGME, Spain) and the Department of Earth Sciences, Royal Holloway University of London (RHUL, UK). Larger thin sections (100x75 mm) were made at the Institut für Geographie und Geologie, Universität Greifswald (Germany). Petrographic analysis of these thin sections was carried out using a Nikon Microphot-FX optic microscope equipped with a Nikon FX-35A camera, or by scanning at high resolution using an Epson Perfection V700 Photo scanner. Thin sections were analysed using the textural classification of Dunham (1962) with modifications for the description of microfacies types as recommended by Flügel (2010). Additional petrophysical analysis of 46 select outcrop samples was performed by Blackbourn Geoconsulting using a Nikon Optiphot-pol petrographic microscope with an integral Canon EOS-50D camera system. A 300-point modal analysis dataset was generated from 13 select samples.

Porosity was estimated by means of JMicrovision software from image analysis of thin section slides, for which purpose pore spaces were stained in blue using an optical microscope. Additional petrophysical analysis of several samples by Geolabs Ltd. (UK) measured triaxial permeability, porosity and particle density parameters. Porosity was estimated based on in-house buoyancy and volume tests (Anovitz and Cole, 2015; Ng, 2017). Compaction due to diagenesis was estimated to be as much as two-thirds (2/3) of sedimentary thickness in the Lefkara Fm. (Stow et al., 2002b), causing a major decrease in porosity, fragmentation of grains and pressure dissolution.

4.4. Biostratigraphy

We collected 40 samples from marly deposits in order to determine foraminifera and nannoplanckton assemblages throughout the sections (Table S1) for biostratigraphic analysis. Specialists from RPS Energy, PalaeoVision Ltd. and the University of Salamanca (Spain) performed biostratigraphic analysis and age determinations. The chronological framework was based on micropaleontology of both planktonic and benthic foraminifera and nannofossils. Biozonal interpretations followed the Gradstein et al. (2012) time scale. Age diagnostic samples contained abundant planktonic foraminifera and nannofossils, although some specimens showed poor preservation. Broken, crushed, overgrown/recrystallized, etched and cemented samples sometimes suffered as well from reworking, which obscured age estimates. Notwithstanding, this study generated more accurate and precise age estimates for samples and sections than previous works. They helped correlate the sedimentary sections and guide the paleo-environmental reconstruction. The identity and relative abundance of foraminifera assemblages moreover helped to constrain the relative water-depth of deposition.

4.5. Mineralogical and chemical composition

Six selected samples of the dominant lithologies listed above were analysed by X-ray diffraction (XRD) (Tables 3 and 4) and scanning electron microscopy - energy dispersive spectroscopy (SEM-EDS). Most XRD and SEM analyses were undertaken by the International Centre for Diffraction Data (ICDD) at Royal Holloway University of London (RHUL, UK). X-ray fluorescence was performed with a Phillips PW3020 X-ray diffractometer. Blackbourn Geoconsulting performed XRD on 11 samples and SEM on 4 samples, respectively at the X-Ray Mineral Services Ltd. (UK) and the Department of Geosciences at the University of Edinburgh (UK). XRD analysis provided qualitative mineral identification and background stripping. The EDS-SEM analyses recorded mineral and chemical composition.

4.6. Other complementary analyses

A regional seismic stratigraphic analysis of offshore areas around Cyprus used seismic data curated by Spectrum Geo Ltd (now TGS, UK) and analysed with the Paradigm® SeisEarth® Multi-survey Interpretation Platform (Figs. S1 and S2 in supplementary material). Seismic stratigraphic analysis identified seismic facies and units following conventional methods and basic criteria proposed by Mitchum et al. (1977) and Catuneanu et al. (2009). Interpretation focused on coeval sedimentary units with onshore Lefkara and Pakhna Fms. Isobaths (time structure) maps were generated for the main discontinuities, and sedimentary thickness maps for the main seismic units.

Regional paleocurrent reconstructions and their relation to the Indian Gateway were developed by the Physical Oceanography Group, University of Málaga (Spain), following de la Vara and Meijer (2016) (Fig. S3 in supplementary material). Reconstructions demonstrated how plate tectonics and the Indian Gateway determined the exchange and

dynamics of water masses to establish the prevailing paleoceanographic regime, proving essential to understand the identified main paleoceanograhic changes.

4.7. Nomenclature

This work adopts the nomenclature for sedimentary facies (F) that we proposed previously in Hüneke et al. (2021) and expands their description and interpretation based on the new results. Bottom current-controlled depositional and erosional features are recognised. We use the term "contourites" *sensu* Stow et al. (2002a), Faugères and Stow (2008) and Rebesco et al. (2014), to indicate a range of sediments affected by different types of currents. We adopted the classification schemes for contouritic drifts of McCave and Tucholke (1986), Faugères et al. (1999), Rebesco et al. (2014) and Hernández-Molina et al. (2022).

5. Results

The Lefkara and Pakhna Fms. appear within the four studied sections predominantly as marls, calcilutites (whitish and greenish), calcarenites, calcirudites, cherts and limestones (Table 1).

5.1. Petra Tou Romiou (PT)

5.1.1. Beach section

It reaches about 20 m in thickness and corresponds to white chalk beds having regular alternations of calcilutites with persistent thin calcarenite beds in the Lefkara Fm. (Figs. 3C, 4 and 5). They strike 220°E and dip 10°SSW on average. Beds exhibit upward coarsening and thickening sequences of about 3 to 5 m (yellow inverted triangles in Fig. 5A). Units appear whitish or light brownish in colour and display occasional pressure dissolution features.

The calcilutite beds reach 30 to 50 cm in thickness and correspond to Facies F2a (Table 1). They have a diffuse mottled appearance resulting from intensive bioturbation, and occasional horizontal lamination. The numerous stratigraphic levels show distinct trace fossils (Table 2), which are typically filled by calcareous sediment of differing grain size or of slightly different colour. These levels alternate with finer-grained calcarenite beds showing sharp or gradational boundaries and occasional bi-gradational sequences (Fig. 5A and C). Microfacies consist of foraminiferal (globigerinid) wackestones (Table 1) in which bioclastic components predominate. Ubiquitous planktonic foraminifera represent at least 10-20% of components. Other bioclasts include radiolarians, siliceous sponge spicules, bivalve fragments and recrystallised foram tests, representing about 10-13% of components. Benthic foraminifera, thin-shelled brachiopods and molluscs occasionally appear. Lime mud and recrystallised foraminiferal material make up 70-75% of the mostly homogeneous matrix, which consists primarily of amorphous calcite and subordinate silica. The matrix is a carbonate mud of nannofossil micrite composed of coccoliths and recrystallised calcite. Irregular, darker-coloured laminae appear within the matrix and probably represent a depositional fabric enhanced by stylolitisation. Together with the surrounding matrix, bioclasts were recrystallised into a somewhat coarser crystalline calcite, and thus show diffuse boundaries. Traces of phosphatic material suggest vertebrate skeletal fragments.

Finer-grained calcarenites correspond to Facies F3a (Table 1). They range from less than 5 cm to about 8 cm, but vary laterally in sedimentary thickness over distances of several meters (Fig. 5A). Calcarenites appear whitish in colour and show gradational boundaries with calcilutites (Facies F2a or F2b). They locally show relict parallel- to cross-lamination along their upper surfaces, which are extensively bioturbated (Fig. 5C). Dominant microfacies include packstones to wackestones and occasional grainstones. Well preserved bioclasts consist of planktonic foraminifera (mainly globigerinids), radiolarians and siliceous sponge spicules in a muddy and/or micrite matrix and a particle-supported fabric. These facies contain higher proportions of forams than F2a, having at least 70-75% of the bioclasts and about 9% of other bioclastic material. In F3a there is some slight banding, distinguished by layers in which the forams are mostly fragmented, while those shown in the field-of-view illustrated here are mostly intact. The lime mud represents only about 15-18% of the sediment. It is homogenous, with a nearly pure calcite composition (up to 99%), minor quartz (~1%), and traces of illite+mica clays (Tables 3 and 4). At some stratigraphic levels, calcarenite beds exhibit lateral changes in thickness over a distance of several meters (Fig. 5A). They may pinch out laterally or become replaced by a pressure dissolution seam. As reported by Rodríguez-Tovar et al. (2019b), here the calcarenite appears only as infill within biogenic traces in the calcilutite below.

Coarse-grained calcarenite beds show clear, sharp bases and normal grading in the lower part (Fig. 5B). This transitions upward into parallel and low-angle cross-lamination, terminating with a heavily bioturbated wave top surface. Lithoclasts appear at the base. They correspond to F3d (Table 1) and may gradually transition into calcilutites. Some coarser-grained beds span about 3 to 10 cm in thickness, with amalgamated internal beds that appear darker (light grey to dark brown) in colour. These deposits are continuous, yet may show lateral changes in thickness over a distance of several meters, or even disappear, and have different ichnoassemblages than the calcilutite beds (Table 2). Microfacies consist of packstone and grainstones with exclusively planktonic (well-preserved) foraminifera (globigerinids) (Table 1).

5.1.2. Section A

Section A lies stratigraphically above the previous section (Figs. 3A, C and 4). Altogether this section spans about 60 m in thickness and consists primarily of alternating chalks (calcilutites) and calcarenite beds (Fig. 4, Facies F3a and F3d, Table 1). Beds strike 65° E and dip 7° ENE/E on average. Chert beds with very good lateral continuity appear in the upper part of the chalks (Figs. 4 and 6D). Below the chert beds, deformed deposits (Facies F5) and normal fault structures are clearly visible in the section (Fig. 6A and B). The upper part of section A (Fig. 4) hosts a thick (~20 m) interval of grey marls (Facies F1, Table 1) with calcilutites (Figs. 3B, 4 and 6E). This represents the upper marl unit of the Lefkara Fm.

Calcilutites (F2a) and calcarenites (F3a and F3d) from this section do not differ from those described for the previous beach section (including bi-gradational sequences, Fig. 6C), and they belong to the same third unit of the Lefkara Fm. Ichnological analysis of section A did not encounter major differences with respect to ichnofossils of the beach section (Table 2). Calcarenites of facies F3a and F3d become thicker, however —some beds reaching 1 m in thickness. Paleocurrent measurements associated with facies F3a indicated average directions of N320 / 350 (NW) (Fig. 4).

5.1.3. Section B

This section corresponds to the lower part of the Pakhna Fm. It spans about 35-40 m in thickness (Figs. 3A, B and 4) and unconformably overlies the older marls (Fig. 3B), bounded by an erosional/irregular surface. Dominant lithologies include calcilutites, calcirudites, calcarenites and occasional marls (Figs. 4 and 7) that correspond to facies F2a, F2b, F3a, F3b, F3c, F3e and F4 in Table 1. These beds form several meters of upward coarsening and thickening sequences (Fig. 7G). The predominant colour of the unit is yellowish or lightly brownish; beds strike about 85°E and dip 7°ENE/E on average. Section B shows a decrease in trace fossil diversity and abundance (Table 2).

Calcilutites appear as thick (30 – 50 cm) whitish beds (Facies F2a) and thin (several centimeters) greenish beds (Facies F2b, Fig. 7A and B, Table 1). Facies F2a consists of a lime mud matrix that appears orange-brown, resembling facies from underlying sections, and marking a higher proportion of detrital clays. Greenish calcilutites (F2b) are more common in the upper part of the record. As indicated by XRD analysis (Tables 3 and 4), its microfacies —though similar to the whitish calcilutites (F2a)— are enriched in illite and quartz with proportion of 2-3%.

Table 1
Table including the identified sedimentary facies, structures, microfacies, ichnofacies and inferred depositional processes.

Facies types			Sed. Structures		Microfacies		Ichnology		Depositional process
F1	MARLS		Lamination				Intensive bioturbation		PELAGIC / HEMIPELAGIC
F2a	CALCILUTITES (Chalks)	Whitish	Primary sedimentary structures not recognised. Occasionally, parallel lamination. Biogenic structures (e.g. burrows)		Foram. (Globigerinid) wackestones (planktonic foraminifers are ubiquitous). Other rare biogens: smaller benthic foraminifers, thin-shelled brachiopods and molluscs. The lime mud is nannofossil micrite (calcareous nannoplankton; coccoliths)		Intensive bioturbation, sometimes burrows difficult to be differentiated from the host sediment. Diffuse mottled appearance	Calcareous pelagic or muddy contourites (reworking of pelagic sediments)	PELAGIC / CONTOURITE
F2b		Greenish	As above		As above Enriched in illite and quartz, with contents of 2-3%		Intensive bioturbation, but easier differentiation of discrete burrows. Diffuse mottled appearance	Calcareous muddy contourites (reworking of pelagic sediments and clays from altered ophiolites)	
F2c		Light to dark grey	Primary sedimentary preserved. Layers, lamination, occasional cross lamination or wavy bedding		Foram. (Globigerinid) wackestones. Clear layering of packed of planktonic foraminifers with mud dominated layers		Intensive bioturbation	Alternation of pelagic deposits with calcareous muddy contourites (reworking of pelagic sediments)	
F3a	CALCARENITES	Whitish beds with gradational boundaries	Central part of a bi-gradational sequence (C3) Faint wavy lamination		Foram. (Globigerinid) packstones to wackestones (packed biomicrites and poorly washed biosparites). The globigerinid tests are well preserved		Heavily bioturbated. Diffuse bioturbational mottling. Discrete biogenic structures	Bioclastic sandy bottom-current deposits (reworking of pelagic sediments)	CONTOURITES
F3b		Whitish beds with internal wavy layering	Bed boundaries are indistinct and show gradual transition to whitish and greenish calcilutite. Banded.	a) Non-compacted layers= homogeneous or bioturbationally-mottled texture; well-preserved parallel and cross lamination is locally preserved. Even more rarely, bed-form related relic morphologies.	Globigerinid packstones-grainstones with varying [low] amounts of shallow-water bioclasts. Biogenic activity clearly influenced the preserved fabric.	a) Non-compacted layers= Globigerinids are the main constitutes, with well-preserved tests. Fragmented shallow-water bioclasts of similar grain size (and a layer-specific amount) may occur.		Bioclastic sandy bottom-current deposits (reworking and redistribution of pelagic sediments and turbidites); formed during a) short-term flow acceleration causing intensification of rippled-bed traction; b) short-term flow deceleration causing dumping of suspended sediment	
				b) Compacted interlayers=pressure-dissolution seams		b) Compacted interlayers= fragmented and flattened test prevail within the compacted laminae. Higher content of fine-grained materials such as micrite and clay minerals.	Diffuse bioturbational mottling and scarce discrete biogenic traces occur		
F3c		Greenish beds with internal wavy layering	See above		See above Enriched in illite, with contents of 2-3%		See above	Bioclastic sandy bottom-current deposits (reworking of pelagic sediments, turbidites & altered ophiolites)	
F3d		Sharp-based beds	Sharp-based / gradual top boundary into calcilutites (F2). Normal grading. Well-preserved primary traction structures (parallel & cross lamination)		Foram. (Globigerinid) packstones and grainstones. Planktonic foraminifers occur almost exclusively (Globigerinacea). Particle-supported fabrics.		Upper part of the bed intensively bioturbated by discrete traces	Fine-grained turbidites sourced from slope settings. Reworked and dislocated pelagic sediments only	TURBIDITES
F3e		Sharp-based beds with normal grading	Sharp-based / planar and gradual upper boundary or sharp and irregular upper surface Distinct normal grading, wavy lamination in upper part.		Larger-benthic-foraminifera globigerinid packstone (more rarely by grainstones). The bioclastic fraction shows a balanced ratio of planktonic (well-preserved) foraminifers and (fragmented) shallow-water materials of similar grain size. The latter		Discrete biogenic structures are recognized	Turbidites sourced from shallow marine carbonate and upper slope settings	

(*continued on next page*)

Table 1 (*continued*)

Facies types		Sed. Structures	Microfacies	Ichnology	Depositional process
			include larger benthic foraminifera. Intraclasts at the base of the normally-graded beds (globigerinid wackestones).		
F4	CALCIRUDITES	Sharp-based beds with massive texture	Planar and sharp base / the top may be either sharp or gradual to whitish or greenish calcilutites (F2) or truncated by calcarenites (F3b,c), forming normal grading	Larger-benthic-foraminifera corallinacean rudstone. The rudstones consist of bioclastic materials from shallow-water sources, < 10% of the planktonic foraminifers (Globigerinacea). Extraclasts occur mainly within the lowermost part of the beds. Larger elongated bioclasts are parallel to bedding.	Discrete traces difficult to be observed	Coarse-grained turbidites sourced from shallow marine carbonate environments

Lime mud comprises up to 60-65% of widely recrystallised to microcrystalline calcite. The units also exhibit small amorphous particles and some larger crystals made up mostly of calcite, with minor silicon and other components indicative of clays. Bioclasts consist of up to 20-35% of forams, which show better preservation (lesser degrees of recrystallisation) than those observed from the beach and A sections. Other bioclast types represent <4%, while benthic forams are <1% of material. XRD analysis detected about 97% calcite and about 1.3% of silt grade quartz and traces of clays (Tables 3 and 4). Facies F2a commonly associates with F3b and represents the fine-grained fraction of bi-gradational sequences hosting an abundance of trace fossils (Table 2) that show a prevalence of deposit feeder behaviour. Facies F2b trace fossils are sometimes filled by facies F4 and F3d / F3e material.

Calcirudites correspond to facies F4 (Table 1). Massive calcirudite beds reach thicknesses of up to 50 cm (Fig. 7A), though but thinner beds may also occur. The beds exhibit sharp, planar bases and massive texture, but also comprise normal grading (Fig. 7A). Internal laminations may occur. At times the top exhibits a sharp or gradational transition to whitish (F2a) or greenish (F2b) calcilutites. Sharp upper boundaries continue into calcarenite beds with wavy laminations (F3b, F3c) that directly cover massive calcirudite beds of F4 (Fig. 7A). Carbonate lithoclasts occur mainly within the lowermost part of the beds, with larger elongated bioclasts parallel to bedding. Microfacies consists of larger-benthic-foraminifera corallinacean rudstone, which signals bioclastic material from shallow-water sources (Table 1), including *Amphistegina, Heterostegina, Operculina,* and *Miogypsina.* Planktonic foraminifera (globigerinids) represent less than 10%.

Calcarenite beds (Table 1) representative of this section appear in facies F3a, F3b, F3c and F3e (Fig. 7A, B, C and E). Facies F3a resembles those of previous sections, appearing as thin beds with gradational boundaries in contact with calcilutites (F2a). They comprise the central part of a bi-gradational sequence with faint wavy lamination and significant bioturbation. Microfacies consist of foraminiferal (globigerinid) packstones-wackestones (packed biomicrites and poorly washed biosparites) in which globigerinid tests appear well preserved (Fig. 8, Table 1).

Facies F3b (Table 1) appears commonly in this section, typically as central part of bi-gradational sequences (Fig. 7B and C). Bed boundaries are indistinct and show a transition to whitish (F2a) or greenish (F2b) calcilutites. Microfacies are characterised by foraminiferal (globigerinid) packstones-grainstones with minor quantities of shallow-water bioclasts (Table 1). Biogenic activity clearly influenced the preserved fabric. These calcarenite beds exhibit lenticular bedding with internal, wavy layering and distinct banding and ichnoassemblages (Table 2) between compacted and non-compacted layers (Fig. 7B, C and D):

i) *Non-compacted layers*. These calcarenitic layers reach only a few cm (1.5-4) in thickness and locally preserve parallel- and cross-lamination. They may show rarer, larger cross-stratification in bedform (small dune-like) related morphologies (Fig. 7E). Measured paleocurrents in these layers indicate an average N160 (SE) flow direction. Microfacies analysis identified packstones or grainstones surrounded by a lime mud matrix. Planktonic forams (globigerinid) comprise between 40% and 70% of bioclasts, with only about 1-2% of other bioclast types. A homogeneous or bioturbationally-mottled texture also includes well-preserved tests. Samples may display fragmented shallow-water bioclasts (larger benthic forams, bivalves, calcareous algae, echinoids) of similar grain size (and layer-specific amounts). Lamination appears as variation in the average size of individual forams. The planktonic forams observed in the samples described here typically range in size from about 0.125 to 0.250 mm (fine sands). Smaller forams are concentrated in thinner bands, while larger forms predominate in other parts. Proportions of lime mud and matrix decline (<30/40%) in parts dominated by the recrystallisation of foram tests and lime mud to microcrystalline calcite (Fig. 9). This microfacies locally shows an orange-brown colour. XRF

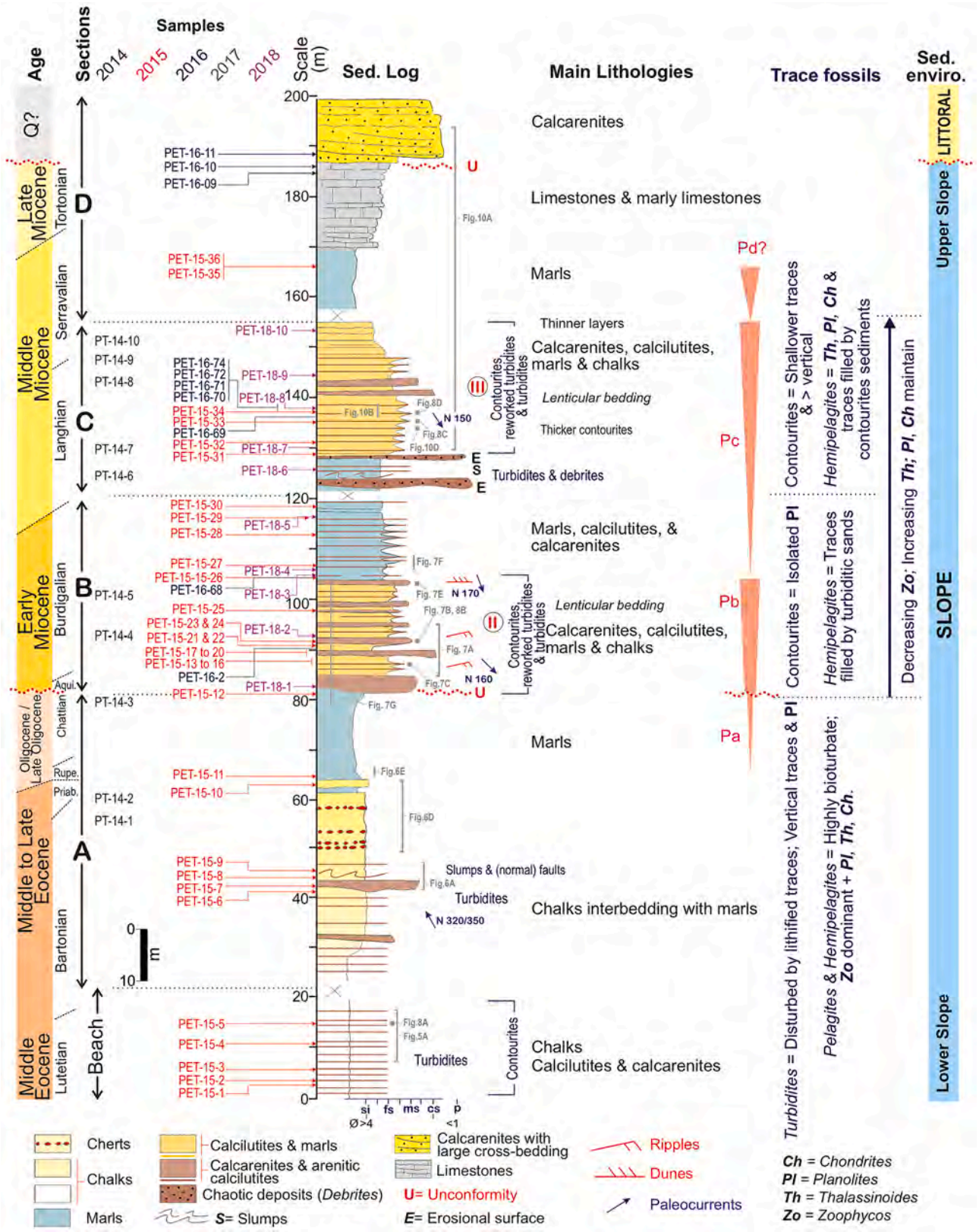

Fig. 4. Sedimentary log for the Petra Tou Romiou outcrops, including the beach and A through D sections, showing lithologies, samples, paleocurrents, dominant trace fossils and sedimentary environment interpretation. The stratigraphic position of sandy contourite packages II and III is highlighted, as are the four packages of strata (P) within the latest Oligocene to middle Miocene deposits (inverted red triangles). Pa) late Oligocene – base of Aquitanian; Pb) Aquitanian / Burdigalian; Pc) Burdigalian to Langhian and Pd) Serravallian to Tortonian.

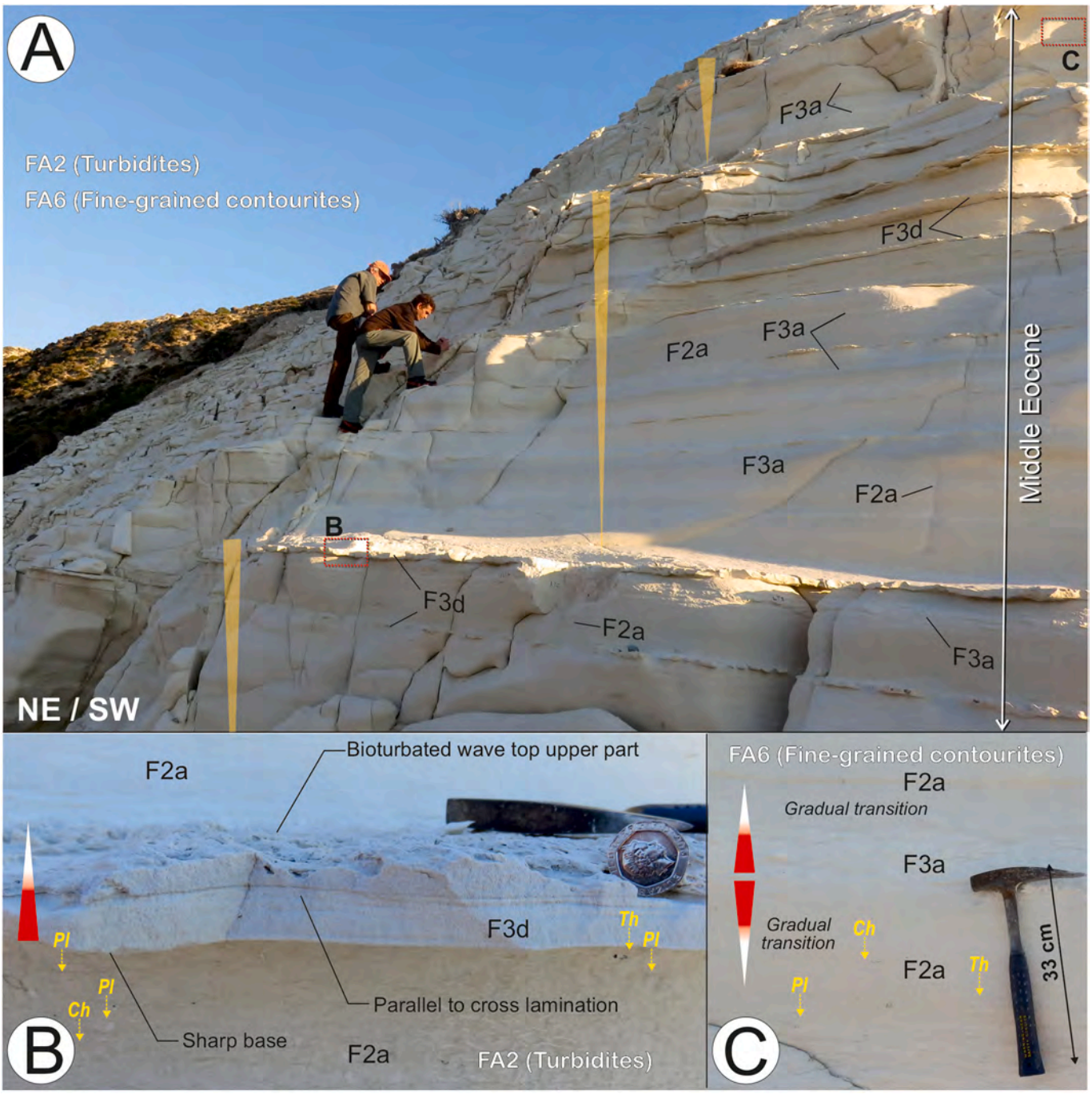

Fig. 5. Main lithologies for the beach section (Lefkara Fm.) at Petra Tou Romiou: A) Sedimentary facies of exposed white chalk beds with regular alternations of calcilutites (F2) and persistent, thin calcarenite (F3) beds from the Lefkara Fm. Short-term coarsening and thickening upward sequences are indicated by inverted yellow triangles at points where turbidites (F3d) and fine-grained contourite (F3a) deposits become more dominant in upper parts of the section. B) Example of facies F3d interpreted as distal turbiditic deposits (FA2) with normal grading, horizontal and wavy laminations. C) Example of sedimentary facies interpreted as fine-grained contourites (FA6) with typical symmetric bi-gradational sedimentary sequences from calcilutites (F2a) to calcarenites (F3a) and to calcilutites (F2a) with gradual transitions.

analyses (Table 3) identified calcite with lesser silicon (Si), aluminium (Al) and other peaks consistent with clays. Nitrogen (N) appears in a relatively high proportion in some samples (as PET-13, Fig. 4). XRD analysis (Table 4) detected up to 95% calcite, <5% illite+mica clay, <1.9% quartz in fine silt fraction, 0.4% dolomite, and about 0.5% illite-smectite clay and traces of kaolinite in some samples.

ii) *Compacted interlayers* appear thinner (<1 cm), with a homogeneous or a diffuse, bioturbated mottled texture and scarce discrete biogenic traces. Fragmented and flattened foram tests predominate within the matrix, and pressure-dissolution seams are frequent. Lime mud appears dark brown in colour probably due to higher content (2-3%) of fine-grained materials, e.g., micrite, detrital clays and possible degraded mica within interlayers (Fig. 7D). Relative to non-compacted layers, XRD analysis of some parts detected a lower percentage of calcite (75-80%), higher illite+mica clay content (<15 %), slightly higher quartz (<4 %) in the fine silt fraction, 0.8% dolomite, and traces of phosphatic material (probably fish remains)

Table 2
Dominant ichnofacies on the studied outcrops and sections in the Lefkara and Pakhna Fms. based on this work and previous research on trace fossils.

Outcrops	Sections		Ichnofacies	Facies	References
Petra Tou Romiou	*Beach*		Dominant ***Ch*** isp. and ***Pl*** isp., frequent ***Th*** isp. and ***Zo*** isp., and rare ***Ta*** isp, assigned to the *Zoophycos* ichnofacies	F2a & F3a	Rodríguez-Tovar et al., 2019b Miguez-Salas and Rodríguez-Tovar, 2019a Miguez-Salas and Rodríguez-Tovar, 2021
			Presence of ***Ar,*** ?***Di***, ***Rh***-like, ***Th*** and borings	F3d	Miguez-Salas and Rodríguez-Tovar, 2021
	A		Low/moderate diversity, with ***Ch***, ***Pl***, ***Th*** and ***Zo***	F2a & F3a	Miguez-Salas and Rodríguez-Tovar, 2019a Rodríguez-Tovar et al., 2020
	B	*Lower part*	A decrease in trace fossil diversity and abundance, including the gradual disappearance of ***Zo***	F2a & F3b	Miguez-Salas and Rodríguez-Tovar, 2019b
			Abundance of ***Ch***, ***Pl***, ***Th,*** and some vertical trace fossils		*This work*
			Non-compacted layers: ***Pl*** in specific horizons just below calcarenitic beds and ***Th*** interrupting successive calcarenite beds		
		Upper part	***Ch***, ***Pl*** and ***Th*** with a significant increase in the abundance of vertical trace fossils	F2a & F1	Miguez-Salas and Rodríguez-Tovar, 2019b This work
	C		Diverse and abundant trace fossils, with larger specimens. ***Ch***, ***Pl*** and ***Th*** with ***Te***, ***Gy*** and ***Op***. Predominance of vertical burrow components.		Miguez-Salas and Rodríguez-Tovar, 2019b
			Progressive increase in ***Th***, ***Pl*** and ***Ch*** that would indicate a general shallowing-upward trend in section C relative to section B.		*This work*
	D		*Not considered*		
Agios Konstantinos	*Zenon*		As in the upper part of section A at Petra Tou Romiou		*This work*
	Agios Konstantinos		***Ch***, ***Pl***, ***Th*** and ***Zo*** in the lower part		Miguez-Salas et al., 2019
			A transition from ***Zo*** to ***Te*** in the upper part, together with ***Sy***		Rodríguez-Tovar et al., 2020
			Some specimens of *Helminthorhaphe* (graphoglyptids) in turbiditic layers		
Korfi	————		***Ch***, ***Pl***, and ***Zo*** and numerous vertical traces		*This work*
Kalavassos	*A*		***Ch*** and ***Pl***		*This work*
	B		***Zo***, ***Pl***, ***Ch*** and ***Th***		*This work*
	C		*Not considered*		

Abbreviations: *Ar= Arenicolites, Ch= Chondrites; Di= ?Diplocraterion; Gy= Gyrolites; Op= Ophiomorpha; Pl= Planolites; Sy= Syringomorpha cyprensis; Ta= Taenidium; Te= Teichichnus; Th= Thalassinoides; Zo= Zoophycos.*

(Table 3). Pure calcite also contained significant percentages of silicon and aluminium, with variable potassium, iron and magnesium indicating the presence of clay minerals. Both matrix and bioclasts show significant recrystallisation into microcrystalline calcite, the calcite crystals infilling or lining the interior of otherwise open foram tests. Evidence of dissolution of foram tests appears in some interlayers.

Calcarenite facies F3b gave porosity values of 10.3% (PET13), 13.7% (PET19) and 10.7% (PET21). Sample PET-15-24c (Fig. 4) gave an apparent porosity of 27.8%, a total porosity of 27.9%, and a permeability coefficient of 1.9 10^{-10} m/s equivalent to about 190 md.

Facies F3c generally resembled F3b (Fig. 7A) but exhibited more greenish beds with internal wavy layering and illite contents of 2-3%. Greenish calcarenite beds with internal wavy layering are more abundant in the upper part of the section (Figs. 3B, 7). The illite concentrate within the compacted layers to confer the greenish colouration. Silt- and sand-sized quartz grains also appear locally in thin sections.

Facies F3e exhibits sharp-based beds with distinct normal grading and sharp or gradual upper boundaries occurring in the middle and upper part of section B (Fig. 3B). Bed thickness does not typically exceed 20 cm. Microfacies consist of Larger-benthic-foraminifera globigerinid packstone (more rarely by grainstones). Calcilutite intraclasts appear at the base of normally-graded beds. The bioclastic fraction consists of planktonic (well-preserved) foraminifera and fragmented, fine-grained, shallow-water bioclasts including larger benthic foraminifera. Discrete biogenic structures are recognised.

The upper part of section B (Fig. 4) shows an increase in marly beds (F1) and a shift to brownish/reddish calcilutites interstratified with whitish calcilutites (Fig. 7F), calcarenites and calcirudites. Facies F3b shows distinct banding between non-compacted and compacted layers, but with thicker compacted layers or replacement by brownish/reddish calcilutites (Fig. 7F). The calcilutitic deposits host a significant increase in the abundance of vertical trace fossils (Fig. 4 and Table 2) and like the previously described units, they show a predominance of deposit feeder behaviour.

5.1.4. Section C

This section lies stratigraphically above section B and reaches thicknesses of about 35-40 m (Figs. 3, 4 and 10). Beds strike 52°E and dip 7°NE/ENE on average. The section hosts the Pakhna Fm. with dominant lithologies of calcilutites (facies F2a, F2b and F2c), calcarenites (facies F3a, F3b, F3c and F3e), and less frequent marls (facies F1) (Table 1, showing bigradational sequences with central intervals similar to —yet thicker than— those of F3a and F3b (50 cm) in section B, becoming thinner again in the upper part of the section (Figs. 4 and 10). Bedsets of several meters exhibit upward coarsening and thickening sequences (Fig. 10A). Both chaotic and deformed deposits (facies F5) appear at the base of the section (Fig. 4).

Calcilutites (F2) span about 15 cm thickness on average (Fig. 10B).

Table 3
X-ray diffraction analysis for the whole rock indicating weight % by mineral phase.

Sample name	Illite/Smectite	Illite+Mica	Kaolinite	Chlorite	Quartz	K Feldspar	Plagioclase	Calcite	Dolomite	Halite	Pyrite	Total
Pet-15-4b	0.0	TR	0.0	0.0	0.9	0.0	0.0	99.1	0.0	TR	0.0	100
Pet-15-24c	0.5	2.6	TR	0.0	1.9	0.0	0.0	95.0	0.0	0.0	0.0	100
Pet-15-27a	0.0	0.0	TR	0.0	1.3	0.0	0.0	97.0	0.0	1.6	0.0	100
Pet-15-33b	0.0	TR	0.0	0.0	1.5	0.0	0.0	98.5	0.0	0.0	0.0	100

TR = trace amounts.

Table 4
X-ray diffraction analysis for the <2 μm.

Sample name	Wt. %	Illite/smectite				Illite			Kaolinite			Chlorite			Calcite	
	<2μm	% A	% B	Order	% Illite	% A	% B	Crys	% A	% B	Crys	% A	% B	Crys	% A	% B
Pet-15- 4b	9.0	0.0	0.0			TR	TR	P	0.0	0.0		0.0	0.0		100.0	9.0
Pet-15-24c	7.9	6.0	0.5	RI/O	50-60	32.8	2.6	P	TR	TR	P	0.0	0.0		61.3	4.9
Pet-15-27a	12.5	0.0	0.0			0.0	0.0		TR	TR	P	0.0	0.0		100.0	12.5
Pet-15-33b	13.9	0.0	0.0			TR	TR	P	0.0	0.0		0.0	0.0		100.0	13.9

A = Weight % relevant size fraction; B = Weight % bulk sample. Mixed-layer Ordering: RI= Randomly Interstratified; O= Ordered Interstratification. Crystallinity: P= Poorly Crystallised. TR= trace amounts.

Foram bioclasts represent about 35-38% (other bioclasts about 0.3%), while the surrounding lime mud represents about 60-65% of the sediment. Pervasive wispy lamination in the lime mud matrix exhibits a slightly reddish-brown colour probably resulting from iron oxides and weathering of detrital clays. Microfacies analysis identified wackestones comprising a lime mud matrix resembling that described for other facies. However, some samples (PET33a) underwent extensive dolomitization (Figs. 8 and 9) and contain relatively high dolomite and quartz proportions. The lime mud consists mostly of calcite, although it also contains visible rhombic crystals of dolomite, especially within foram tests. Facies F2b moreover contains subordinate detrital clays and silt-sized quartz grains.

Facies F3b shows less distinct banding between non-compacted and compacted layers. The thickness of the non-compacted layers resembles that observed in section B, whereas the compacted interlayers appear thinner or are normally absent (Fig. 10B and C). Microfacies analysis identified wacketones to packstones including a lime mud matrix (Table 1). Planktonic foraminiferal bioclast content varies slightly, typically representing 40-45% (other bioclasts about 1.3%) and the surrounding lime mud <62%. XRD analysis detected some 98.5% calcite, 1.5% quartz and traces of clay minerals. The lime mud matrix is quite homogeneous with amorphous calcite, though coccoliths also appear (Fig. 9). Non-compacted layers from F3b in section C sometimes resemble the one described in section B (PET33b); but in other cases (PET34b) their texture is less grain-supported than equivalent facies in section B. Some microfacies having a relatively high content of lime mud matrix occur within the transition between packstones and wackestones (Table 1). Facies at the top of F3b locally show cross-stratification in bed forms (small dune-like) (Fig. 10D). Paleocurrents measured in facies F3b and F3a exhibit an average trend of N150° (SE), similar to those collected in section B.

Section C hosts diverse and abundant trace fossils, being different in Facies F3a and F3b with respect to F2a (Fig. 4 and Table 2). Traces indicate a prevalence of filter and deposit-feeding strategies.

5.1.5. Section D

This last section consists of a relatively thick interval (~15-20 m) of light grey to whitish marls (Figs. 3 and 4), which correspond to Facies F1 (Table 1). Beds strike 56°E and dip 4°NE on average. Thin (~15-30 cm) limestone beds above comprise about 15 m total thickness. At the top of the section, coarse-grained Quaternary calcarenites unconformably overlie the previous limestones (Figs. 4 and 10A). These calcarenites are bounded by a clear basal erosional unit with large-scale cross-stratifications migrating south and hosting abundant shallow marine fossils. The limestones and the above Quaternary deposits fell outside the scope of this work and were not studied in detail.

5.1.6. Age

Previous authors who studied the Lefkara and Pakhna Fms. at the Petra Tou Romiou location (Kähler and Stow, 1998; Stow et al., 2002b) only reported general chronostratigraphic ages. Consensus assigns the white chalk and upper marl units from the middle and upper Lefkara Fm. to Eocene, Oligocene and Miocene times. The top of the Pakhna Fm. is Miocene, but the boundary between the two formations remains cryptic. Eighteen samples, collected and dated from the sections described above, serve to constrain their relative stage ages (see detailed chronostratigraphic results in Table S1 of supplementary material).

Biostratigraphic results indicate a Lutetian (~45-42 Ma, middle Eocene) age for the beach section and Lutetian to Priabonian (~42-36 Ma, middle to late Eocene) age for section A (Fig. 4, Table S1). These units underwent some degree of early Eocene reworking. Two samples collected from the base and the top of the first thick marly deposits in the uppermost horizons of section A (Fig. 4) suggest a late Rupelian-early Chattian (~29.5 to 27 Ma, Oligocene) to Chattian (~27- 23 Ma, late Oligocene) age, yet they contain reworked Eocene to Paleogene planktonic and benthic foraminifera. Samples from section B reveal that the basal part of this section is latest Aquitanian – early Burdigalian (early Miocene) or from ~ 21 to 19.5 Ma (Fig. 4 and Table S1). Most deposits from section B are Burdigalian in age or between ~ 19.5 and 16 Ma (early Miocene); its upper part could be even lower Langhian or between ~ 16 and 15 Ma. Section C is Langhian (early Miocene) to Serravallian (middle Miocene), or between ~ 15 and 12 Ma. All samples from sections B and C show substantial reworking of older Neogene, Paleogene and even Cretaceous microfossils. Section D marl sediments are Serravallian in age or between 12.77 and 11.54 Ma (Fig. 4). Limestone deposits at the top of section D and below Quaternary shallow marine deposits are Tortonian in age (~11.6 - 8 Ma).

5.2. Agios Konstantinos (AK)

This area hosts clear examples of both the Lefkara and Pakhna Fms., the former overlying the Troodos Massif. This Agios Konstantinos section has not been logged in detail, though previously studied by Kähler (1994). The upper Lefkara hosts the same facies as the Petra Tou Romiou locality. Thick deformed units reflect the tectonic influence of the massif (the Yerasa lineament, Fig. 2). A marly unit appears atop the Lefkara Fm. (Figs. 11 and 12A) just below the Pakhna Fm.

5.2.1. Zenon Section (Z)

Here the section reaches roughly 15 to 20 m thickness (Fig. 11). Marls (Facies F1, Table 1) predominate but calcilutites also persist (Fig. 12A). These deposits correlate with the upper unit of the Lefkara Fm. and are therefore stratigraphically equivalent to marls from the upper part of section A at Petra Tou Romiou. The contact with the overlain Pakhna Fm. is covered and was not described.

5.2.2. Agios Konstantinos Section (AK)

Beds strike 110°E and dip 5°/10°E. Exposures of this section reach thicknesses of ~120 m (Fig. 11) and correspond to the lower part of the Pakhna Fm. The section lies stratigraphically above the Zenon section marls (Fig. 12A), although the contact between the two remains covered. Dominant lithologies include marls, calcilutites, calcarenites and calcirudites (Figs. 12B, C and 13). The sediments are predominantly yellowish or light brown and mainly correspond to facies F2a, F2c, F3a, F3b, F3d, F3e, F4 and F5 (Table 1 and 2). These facies occur throughout the section, whereas marls (F1, Table 1) predominate in the middle part of the section from 30 to about 90 m (Fig. 11). In the lower and upper parts, marly beds are absent or very thin.

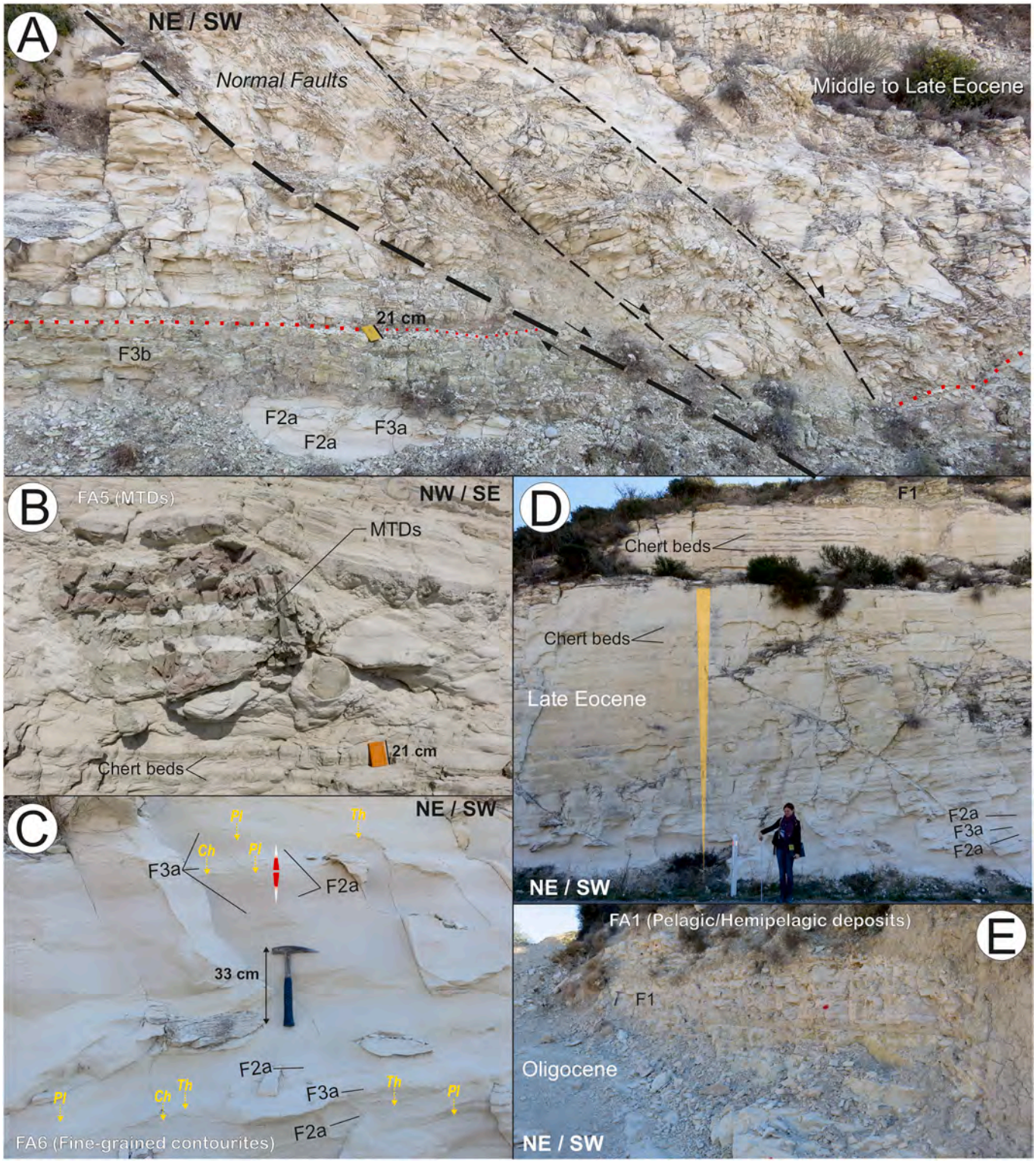

Fig. 6. Main lithologies for section A (Lefkara Fm.) at Petra Tou Romiou composed of alternating chalks (calcilutites) and calcarenite beds: A) Local normal fault structures; B) Local mass transport deposits (MTDs, FA5) in the third unit of the Lefkara Fm. (middle Eocene to Oligocene and early Miocene) composed of sediments of the second unit of the Lefkara Fm. (early to middle Eocene) corresponding to white chalks with extensive chert horizons; C) Example of sedimentary facies interpreted as fine grained contourites (FA6) with typical symmetric bi-gradational sedimentary sequences from calcilutites (F2a) to calcarenites (F3a) and to calcilutites (F2a) with gradual transitions; D) Chalk and chert beds with very good lateral continuity at the top of section A. Short-term coarsening and thickening upward sequences are shown with an inverted yellow triangle; E) Interval of grey marls (FA1) with calcilutites corresponding to the upper marls unit of the Lefkara Fm.

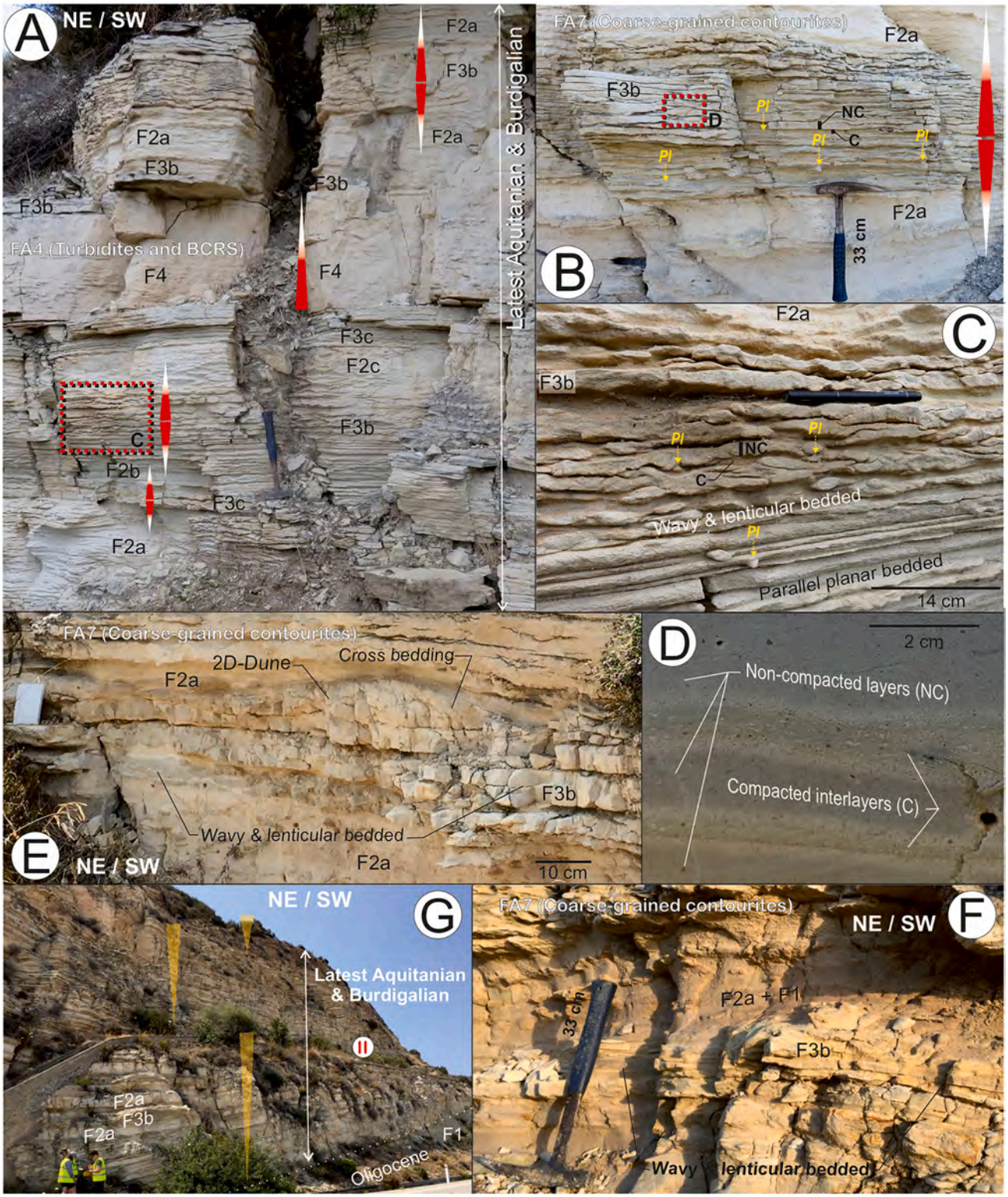

Fig. 7. Main lithologies for section B (Pakhna Fm.) at Petra Tou Romiou: A) Sedimentary facies with alternating calcilutites (F2a) and persistent calcarenite (F3a, F3b and F4) beds from the Lefkara Fm. (FA4 and FA7); B) Example of sedimentary facies interpreted as coarser-grained contourites (FA7) with typical symmetric bi-gradational sedimentary sequences from calcilutites (F2a) to calcarenites (F3b) and to calcilutites (F2a); C) Central division (F3b) of the symmetric bi-gradational sedimentary sequences with parallel planar and wavy to lenticular beds; D) Detail of the non-compacted layers (NC) and compacted interlayers (C) described in the sandy contourites (FA7) associated with the central division (F3b) of the bi-gradational sedimentary sequences (location in B); E) Example of asymmetric bi-gradational sedimentary sequences (FA7) from calcilutites (F2a) to calcarenites (F3b) and to calcilutites (F2a). Bedforms from the central division evolve from parallel planar, to wavy to lenticular beds, showing cross-stratification interpreted as sandy ripples that evolved into small dunes; F) Examples of facies in the upper part of section B with an increase of marls as well as a change in colour, with visible yellowish marls /reddish calcilutites, grey calcilutites and occasional calcarenites (FA7); G) Short-term thickening upward sequences identified in section B are indicated with inverted yellow triangles. Here, the contact between the Lefkara and Pakhna formations is highlighted with a dotted white line.

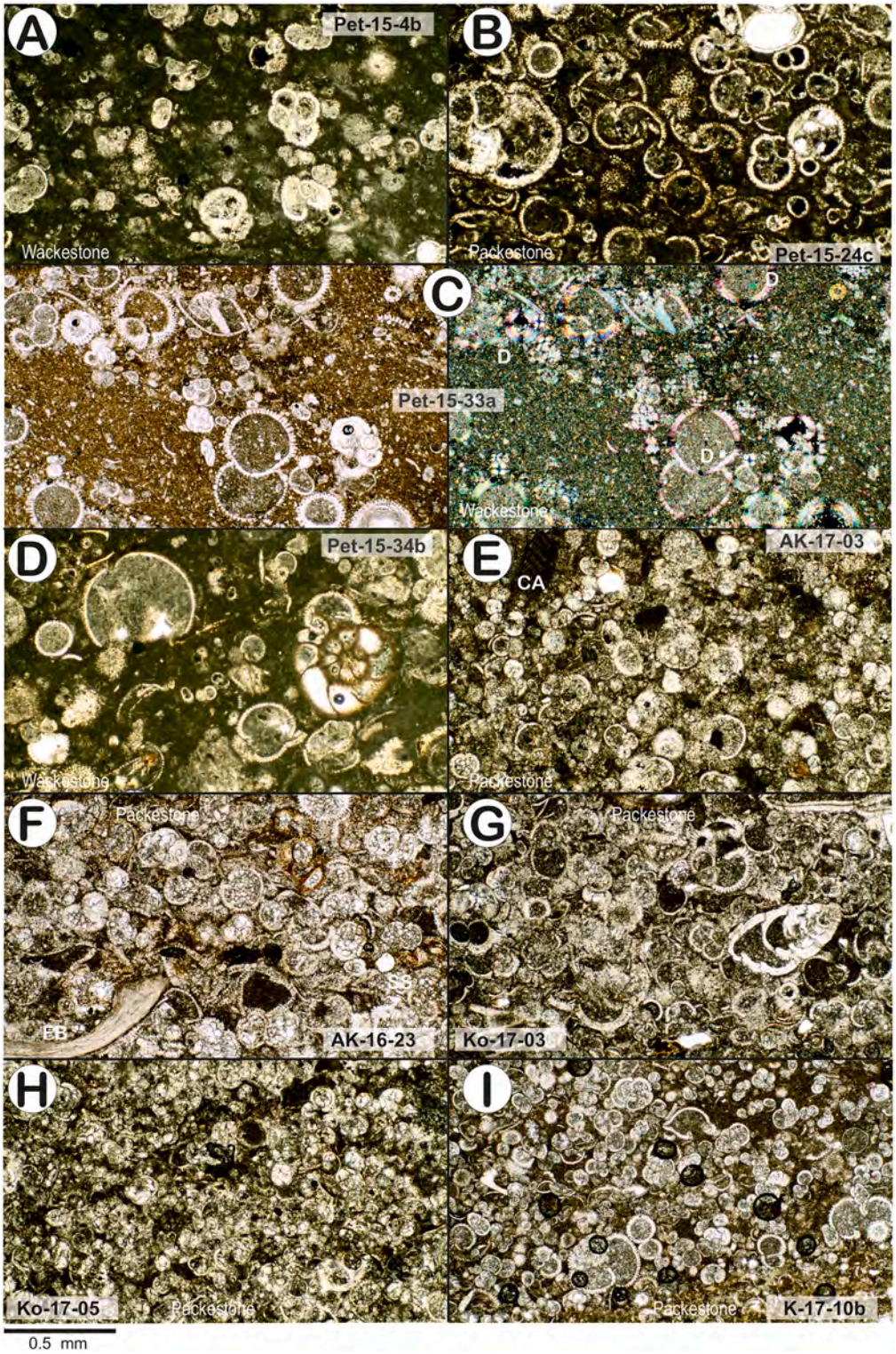

Fig. 8. Examples of microfacies within calcarenite deposits interpreted as sandy contourites at Petra Tou Romiou (A to D), Agios Konstantinos (E-F), Korfi (G-H) and Kalavasos (I). Position of the examples in Figs. 4, 9, 12, 14 and 19. A) Facies F3a with wackestone facies for finer-grained contourites. Bioclastic material resembles pelagic/hemipelagic deposits (F2a); B) Facies F3b with packstones dominated by planktonic foraminifera (and <2% other bioclasts) within a lime mud matrix (33%); C) Facies F2a transition to F3b wackestone, extensively dolomitized, including foram tests replaced by dolomite(D); D) Facies F3b with a wackestone-dominated lime mud matrix (62%) and <40 % planktonic foraminifera and other bioclasts. Note a benthic foram on the right; E) Facies F3b with packstone fabric having planktonic foraminifera and including fragments of calcareous algae (CA); F) Facies F3b with packstones of forams and other bioclasts as fragmented bivalves (FB), echinoids, sponge spicules (SS), etc.); G and H) Facies with packstones showing mostly planktonic foraminifera within a lime mud matrix and with some benthonic foraminifera; I) Facies F3a with packstone to wackestone fabric, mostly with planktonic foraminifera within a lime mud matrix and affected by significant dolomitization. Dark circles are air bubbles within the mounting resin. The examples from A, D, E, F, G and H offer evidence that bioclasts are affected by recrystallisation into finely crystalline calcite.

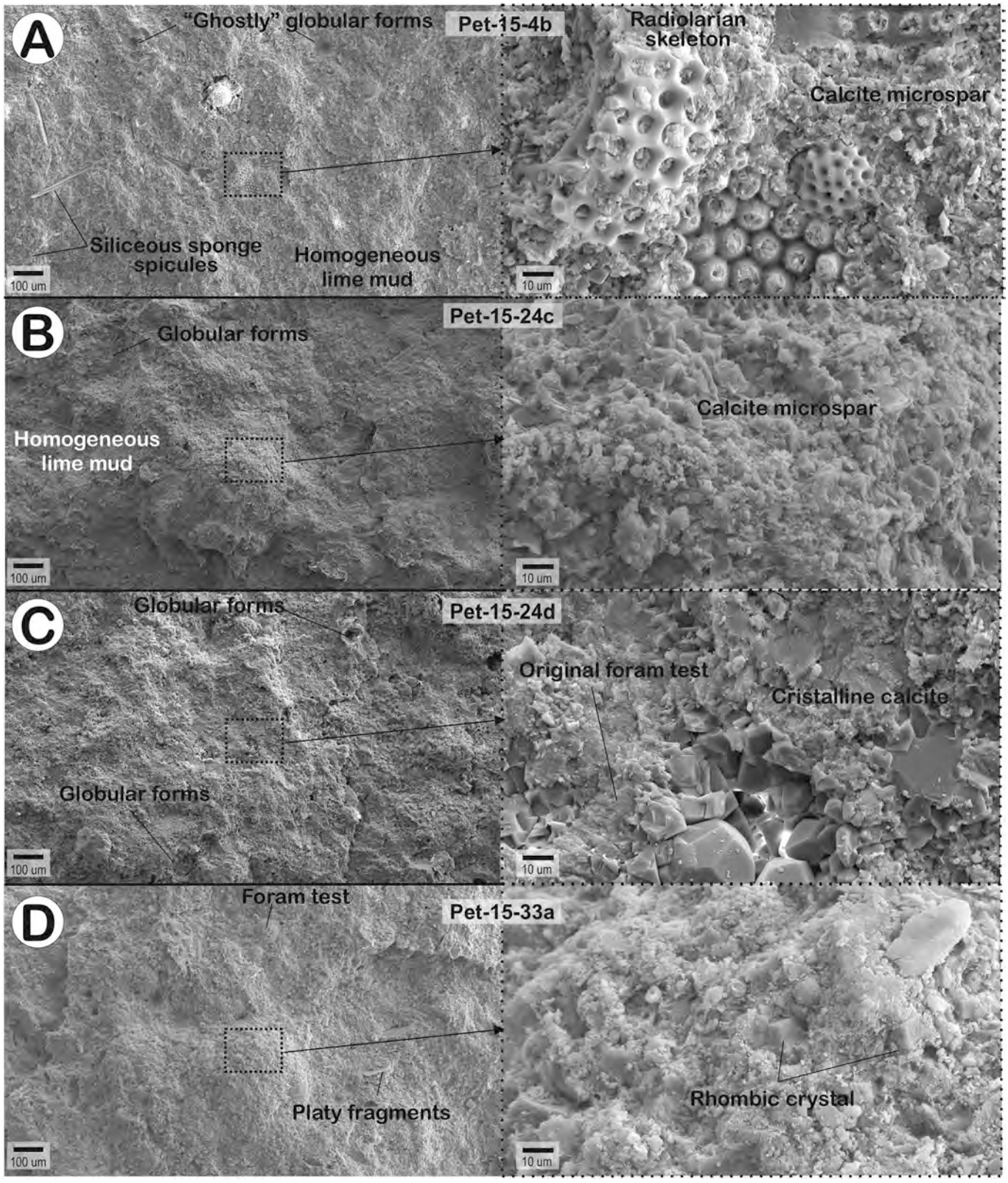

(caption on next page)

Fig. 9. SEM images for contourite deposits indicating lime mud (left) with relatively low-magnification (100 μm) and lime mud matrix (right) with higher magnification (10 μm). The lime mud is usually homogeneous due to dissolution and recrystallisation. The foraminifera clearly appear in thin sections as numerous "ghostly" globular forms. The components of the lime mud matrix consist of particles several microns apart, some of them amorphous. Others show crystal terminations representing recrystallised calcite, while yet others display some microstructure indicating that they are bioclast fragments such as coccoliths. A) Sample illustrated in thin section of F3a showing lime mud (left) with ghostly globular forms. Elongated bioclasts may represent siliceous sponge spicules. At right, radiolarian skeletons appear intergrown with calcite cement; B) Homogeneous lime mud in F3b where dissolution and recrystallisation of foram tests makes them almost undetectable, but indistinct globular forms and pods of more coarsely crystalline calcite elsewhere probably likewise indicate locations of forams. On the right, the lime mud matrix mostly consists of calcareous particles a few microns across, some of which are amorphous, although many exhibit euhedral crystal faces indicating recrystallisation. Numerous fibers present suggest small amounts of clay present throughout the matrix; C) Homogeneous lime mud in F3b with some globular forms and pods of sparry calcite that infill foram tests. Forms at right illustrate part of a pod of sparry calcite. The more finely crystalline calcite elsewhere may represent original calcareous tests that have been recrystallised; D) Bioclasts within F3b include better preserved forams as compared to many other samples examined in the contourites. This may be associated with the dolomitization recognized in package III from section C at the Petra Tou Rominou and Kalavasos localities, where clearer morphological and/or mineralogical evidence of bioclasts and the surrounding matrix is preserved. On the right, small rhombic crystals of dolomite are visible, as well as calcite, with subordinate clays and occasional quartz grains that demonstrate not all the matrix has been dolomitized. Position of the examples given in Fig. 19.

Facies F5 exhibits deformed deposits throughout the section (Figs. 12B and 13B). One of the biggest event occurs at the base of the section, between 10 and 20 m (Fig. 12B and C),. This section has more abundant diagenetic features than the Petra Tou Romiou section.

Calcilutites are characterised by facies F2a and frequent F2c (Table 1), which include light to dark brownish-grey wackestone. Facies F2a exhibits a homogenous fabric of sparsely-packed planktonic forams within the dominant lime mud matrix, similar to those described for Petra Tou Romiou units. Most of the forams are well-preserved, but many have been recrystallised to a finely crystalline calcite. The units show intense bioturbation, with burrow infill composed of mud with planktonic foraminifera. Facies F2c appears light to dark brownish-grey in colour (Fig. 13C-F) and displays faint or sharp layering of packed planktonic forams in mud dominated layers (sparse biomicrite). Deposits show parallel lamination, occasional cross-lamination or wavy bedding, and intense bioturbation (Fig. 13A, D-F, Table 2). For these two facies, planktonic foraminiferal matrix contain intraparticle micrite and sparite different from the interparticle micrite. Diagenetic evidence includes pressure solution features and stylolites, occurring pervasively throughout facies F2a. XRD analysis of some of these samples detected up to 97% calcite, <2% illite+mica clay and <1% quartz.

Calcarenites appear in facies F3a, F3b, F3d and F3e (Table 1). F3d and F3e are orange-brown in colour (Fig. 13A, E and G) and correspond to packstone-grainstone, which is supported by homogenous and well-sorted grains of planktonic foraminifera with very little interparticle lime mudmatrix. The unit displayed variable percentages of clays, possibly affected by compaction causing pressure dissolution or stylolite features (facies F3a and F3e) as well as by diagenetic alteration through cementation and neomorphism (facies F3b). Recrystallised textures include finely crystalline calcite. Facies F3a (Table 1) consists of packstone with distinct bioturbation (Table 2), faint parallel- or cross-lamination, and wavy bedding. Facies F3b consists of foraminiferal packstone – grainstones with a higher proportion of interparticle mud. Foram distributions are relatively homogenous within distinct parallel- or cross-laminations displaying subtle bioturbation features. Other sedimentary structures observed include flaser and wavy bedding (Fig. 13G). Samples with grainstone microfacies (F3d, F3e) occasionally contain benthic forams, fragments of calcareous algae, brachiopods, echinoids, bivalves, serpulids and occasional bryozoans. Larger shallow marine benthic forams include *Amphistegina*, *Operculina*, *Discocyclina*, *Lepidocyclina, Miogypsina*, and *Borelis melo*. Smaller planktonic forams include *Globigerina* and *Orbulina* (globigerinids). In samples with packstone microfacies, intact or fragmentary planktonic foraminifera ranging in diameter from 0.250 to 0.125 mm predominate within the dark, lime mud matrix. Facies F3e features packstone-grainstone beds with a sharp base, occasional sole marks and scour fills (Fig 13D), normal grading with well-preserved lamination, and an absence of bioturbation. In these facies, the lime mud matrix within planktonic foraminiferal tests has partially recrystallised to microcrystalline calcite cement, and micrite grades into microspar. Compositional analysis of the two calcarenite samples found mainly calcium carbonate along with minor concentrations of magnesium, aluminium and silicon, and traces of sodium, chlorine, potassium, phosphorus and iron. XRD analysis of some samples detected up to 98.8% calcite, <0.7% illite+mica clay and <1% quartz.

Calcirudites (Facies F4; Table 1) are orange-brown coloured bioclastic rudstone, gradually passing upwards into calcarenites (grainstone). Sedimentary structures include normal grading and fining upwards, imbrication of large clasts, parallel lamination, and lenticular lamination (Fig. 13A). These facies mark a gradual upward transition of normal grading or sharp upper surfaces indicating erosional horizons. They are composed primarily of thick-shelled bioclasts, including larger, shallow marine benthic foraminifera, brachiopods, bryozoans, coralline red algae, crinoids, echinoid fragments and serpulid bioclasts. Occasional lithoclasts represent shallow water limestones and also intraclasts, possibly rich in deep-water radiolarians. Foraminifera types among the larger shallow marine benthic foraminifera include *Amphistegina, Heterostegina, Operculina, Discocyclina*, *Lepidocyclin*a, *Miogypsina*, and *Borelis melo*. The matrix consists of micrite and smaller planktonic forams occurring in both intact and fragmented forms, together with a sparry calcite cement. Smaller planktonic foraminifera include *Globigerina* and *Orbulina* (globigerinids). An interparticle micrite or sparite matrix predominates throughout. Intraparticle micritic recrystallisation is also observed among lithoclasts. Peloids or fecal pellets comprise the remainder of the composition.

Calcarenites and calcirudites give average porosities of 0.27% to 0.11% for the calcirudite (AK- 16-02-L, AK-16-26). Calcarenite samples do not give average porosities higher than 0.01% (AK-16-05 and AK-16-14). Zones around pressure solution features have higher porosity values, between 16.6% and 20.76% (AK-16-17).

5.2.3. Age

Ten samples from the Agios Konstantinos and Zenon sections were analysed for their chronostratigraphic age (Fig. 11 and Table S1). The Zenon marls gave an age of early Rupelian (early Oligocene) and did not show reworking within either micropaleontological or nannofossil assemblages. The base of the Agios Konstantinos section appears to be late Rupelian to Chattian in age (late Oligocene). Samples within the section give early Aquitanian ages (~ 23 Ma; early Miocene). The upper part of the section gave ages ranging from Burdigalian to Langhian. The top of the section (sample AK-16-27. Figs. 11 and 13H) gave a late Burdigalian age (~ 17.5 to 15.97 Ma). Micropaleontological assemblages from this interval show moderate to high degrees of reworking of predominantly Eocene —but also locally Eocene to Oligocene, some Late Cretaceous and occasional Palaeogene— nannofossil material, especially in lower parts of the section. The upper part of the section shows occasional reworking of Eocene to Oligocene planktonic foraminifera and nannofossils.

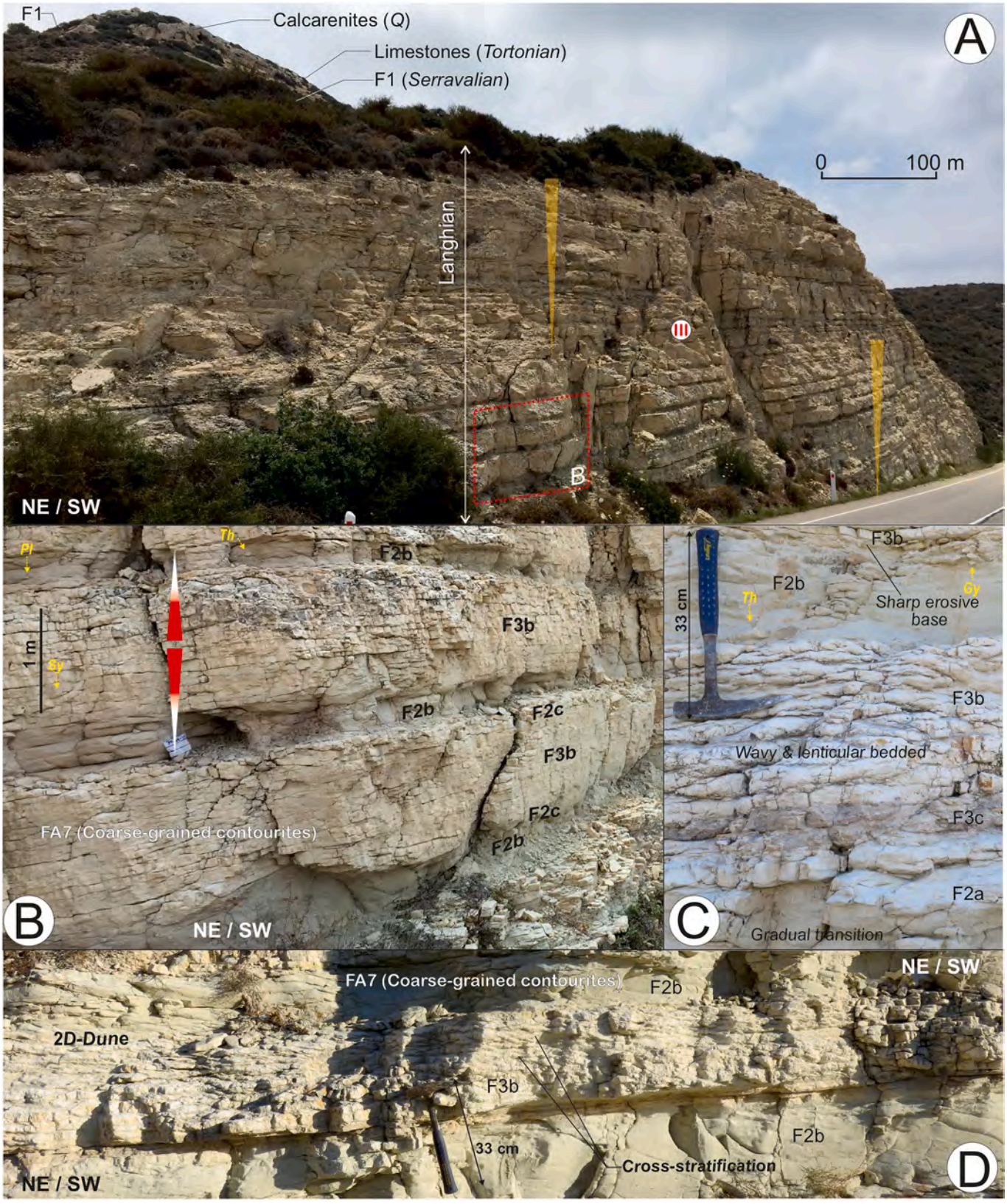

Fig. 10. Main lithologies for sections C and D (Pakhna Fm.) at Petra Tou Romiou: A) Calcilutites (F2a; F2b), calcarenites (F3a, F3b, F3c, F3e) and less frequent marls (F1). Short-term thickening upward sequences are indicated with inverted yellow triangles; B) and C) Examples of sedimentary facies interpreted as coarser-grained contourites (FA7) with typical bi-gradational sedimentary sequences from calcilutites (F2a) to calcarenites (F3a, F3b) and to calcilutites (F2a); D) Example of an asymmetric bi-gradational sedimentary sequence (FA7) from calcilutites (F2a) to calcarenites (F3b) and to calcilutites (F2a). Bedforms from the central division evolve from wavy to lenticular beds to cross-stratification interpreted as sandy ripples that evolve into small dunes.

5.3. Korfi (ko)

The section reaches a thickness of roughly 30 m, with beds striking 130°E and dipping 30°SW. Dominant lithologies are marls, calcilutites and calcarenites (Fig. 14), more closely resembling those of Agios Konstantinos than those from Petra Tou Romiou. Marls predominate in the lower part of the section (facies F1 in Table 1) as opposed to the upper part (last 15 m) where calcilutites and calcarenites predominate.

Calcilutites consist of facies F2a and F2c (Table 1), being light to dark brownish-grey in colour (Fig. 15 A and B). Facies F2a corresponds to a wackestone of planktonic foraminifera within a mud matrix. The deposit lacks sedimentary structures but shows intense bioturbation (Table 2). Facies F2c exhibits faint layering of packed planktonic foraminifers within mud- or clay-rich layers subjected to intensive bioturbation. The deposit shows parallel lamination and occasional cross-lamination or wavy bedding (Fig. 15D). Paleocurrent measurements associated with these beds indicate N70° (NE) directions, with one uncertain measurement of N240° (SW).

Calcarenite beds corresponding to facies F3d and F3e (Table 1) represent packstone-grainstones with sharp boundaries, normal grading, horizontal lamination, cross-lamination and convoluted lamination (Fig. 15C and D). These units contain varying proportions of planktonic foraminifera within a lime mud matrix, while coarser beds include bioclasts of shallow marine benthic foraminifera (up to 10-20%), brachiopods, bryozoa, coralline red algae, echinoid fragments, crinoids and serpulids. Bioclasts and lime mud matrix are found recrystallised into a

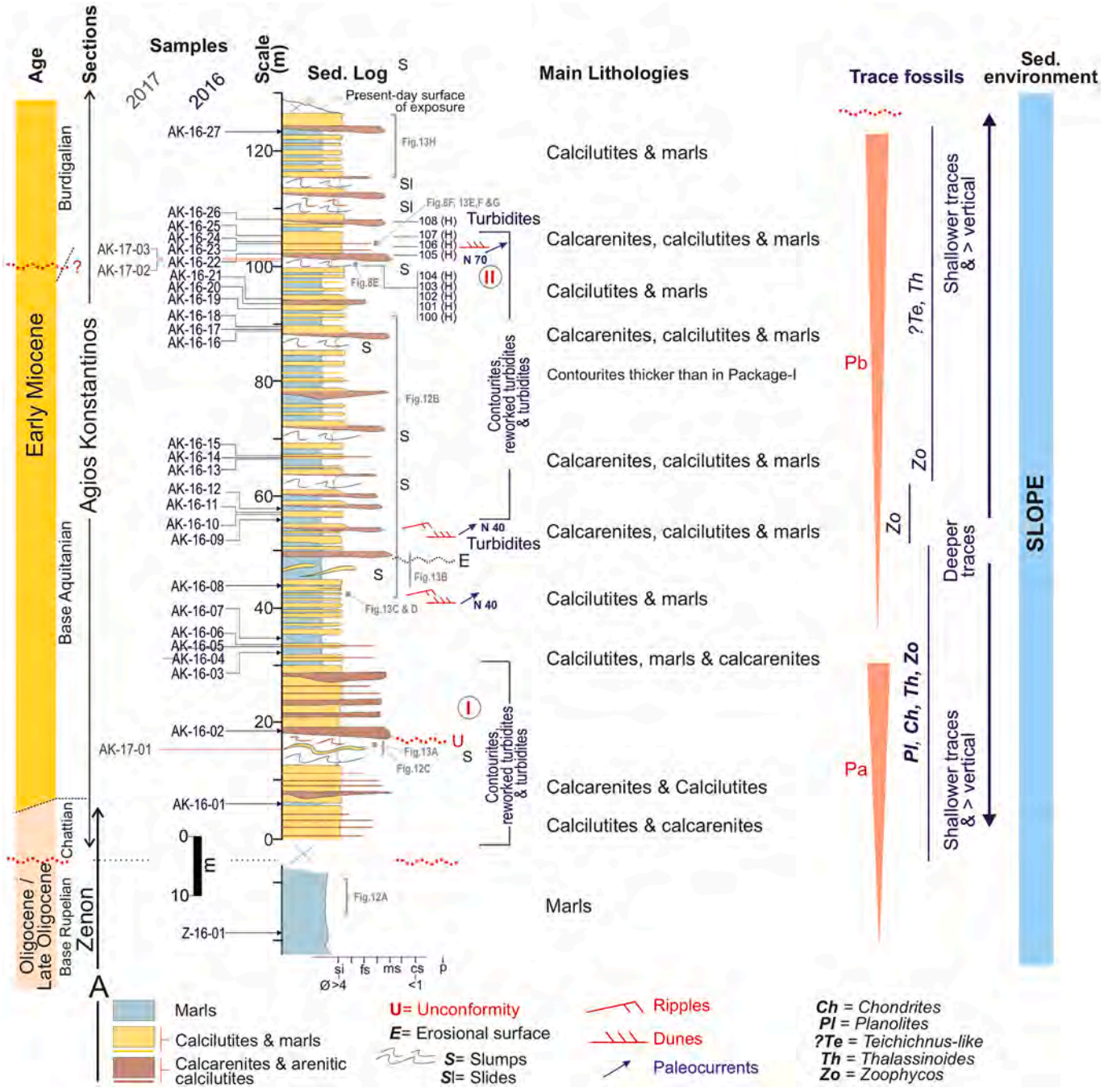

Fig. 11. Sedimentary log for the Zenon section and Agios Konstantinos showing main lithologies, samples, paleocurrents, dominant trace fossils and sedimentary environment interpretation. The stratigraphic position of sandy contourite packages I and II is highlighted, and the two packages of strata (P) within the latest Oligocene to middle Miocene deposits are indicated by inverted red triangles: Pa) late Oligocene – base of Aquitanian, and Pb) Aquitanian Burdigalian.

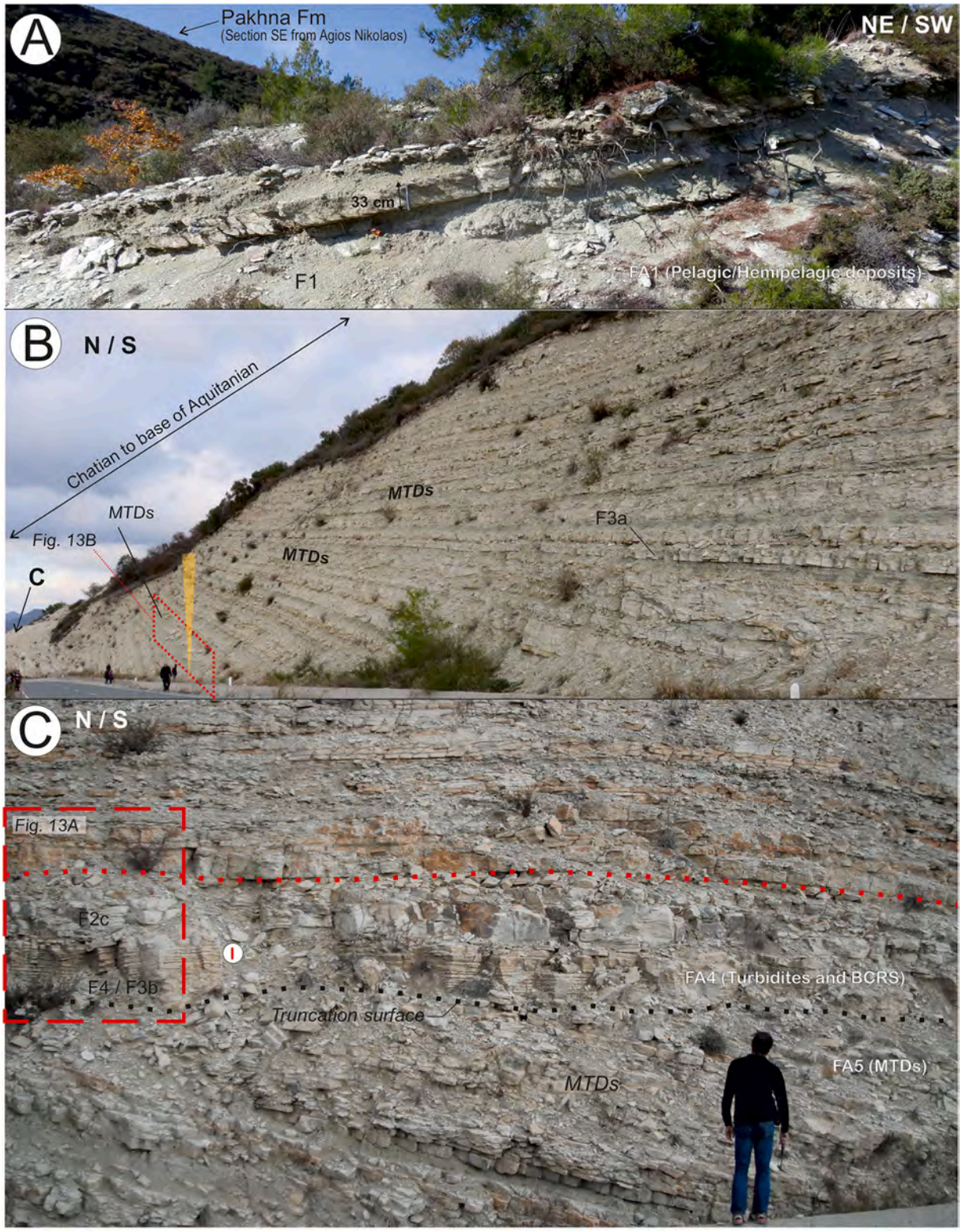

Fig. 12. A) Marls and calcilutite deposits (FA1) from the Zenon section corresponding to the upper marl unit of the Lefkara Fm.; B) Main lithologies for the Agios Konstantinos section with marls (F1), calcilutites (F2a and F2c), calcarenites (F3a, F3b and F3e), and calcirudites (F4) that characterised pelagic/hemipelagic (FA1), contourite (FA6 and FA7), turbidite (FA4 and FA3), and mass transport deposits (MTD, FA5). Identified short-term thickening upward sequences are indicated by inverted yellow triangles. The positions of Fig. 11A and B are indicated. C) Large MTDs (slumps, FA5) at the base of the Agios Konstantinos section with a prominent truncation surface at their top. The position of Fig. 13A with reworked turbidite (F4) and sandy contourite deposits (F3b) is also shown.

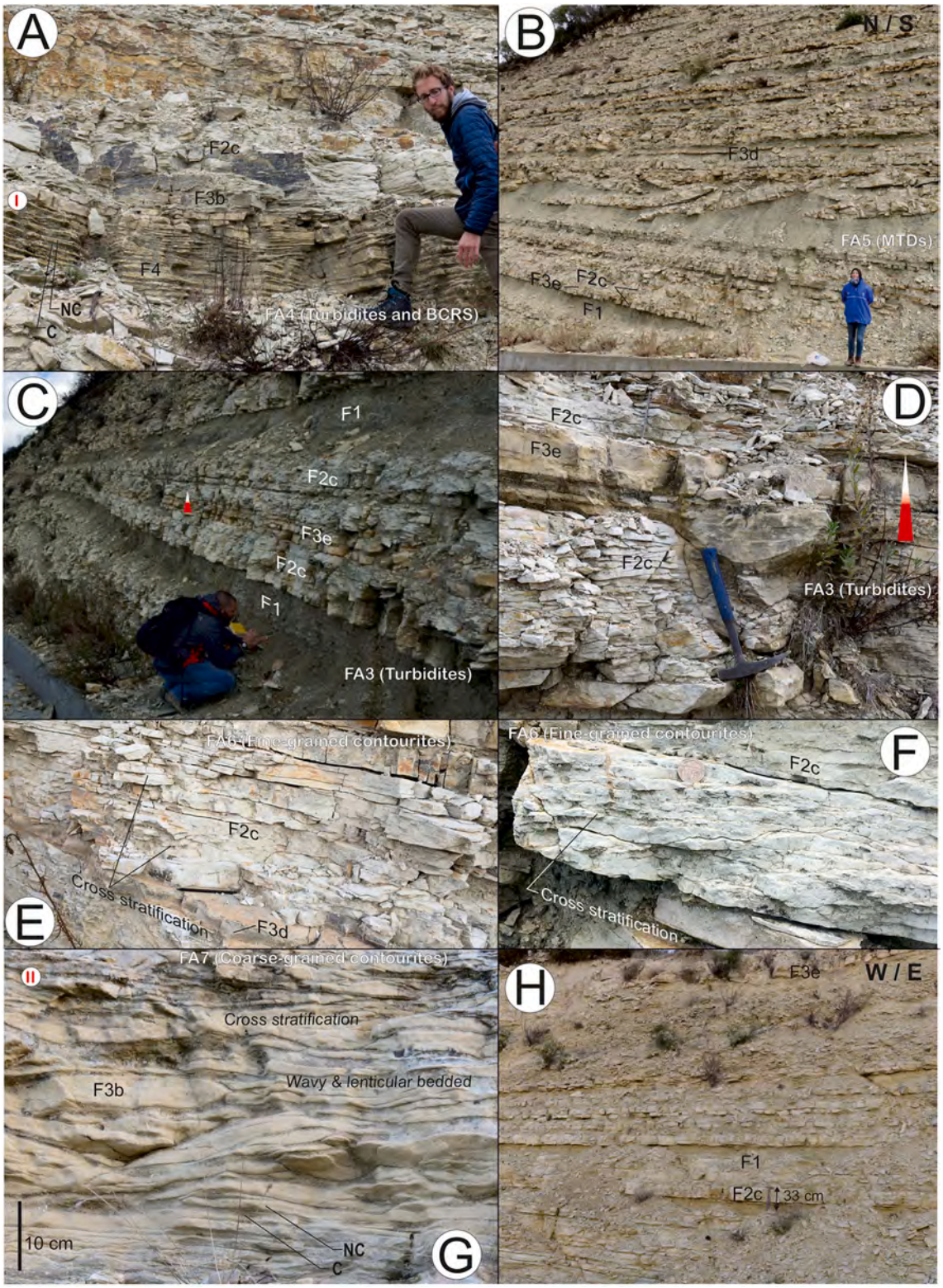

Fig. 13. A) Sedimentary facies with alternating calcilutites (F2c) and persistent calcarenite (F3b 4) beds from the Pakhna Formation, with an example of sedimentary facies interpreted as coarser-grained contourites with non-compacted (NC) and compacted interlayers (C) from bottom-current reworked turbidite (F4); B, C and D) Example of marls (F1), calcilutites (F2c), calcarenites (F3e) and MTDs (FA5). Note the darker colour of F1 as well as the orange-brown colour of calcarenites. In D the facies F3e there are packstones with a sharp base, occasional sole marks, normal grading with lamination, and an absence of bioturbation (FA3); E) and F) Calcilutite deposits (F2c) with cross-lamination associated with finer-grained contourites (FA6); G) Calcarenite (F3b) wavy and lenticular beds with cross-stratification interpreted as coarser-grained contourites with non-compacted (NC) and compacted interlayers (C); H) Upper part of the Agios Konstantinos section with dominant marls (F1), calcilutites (F2c) and calcarenites (F3e).

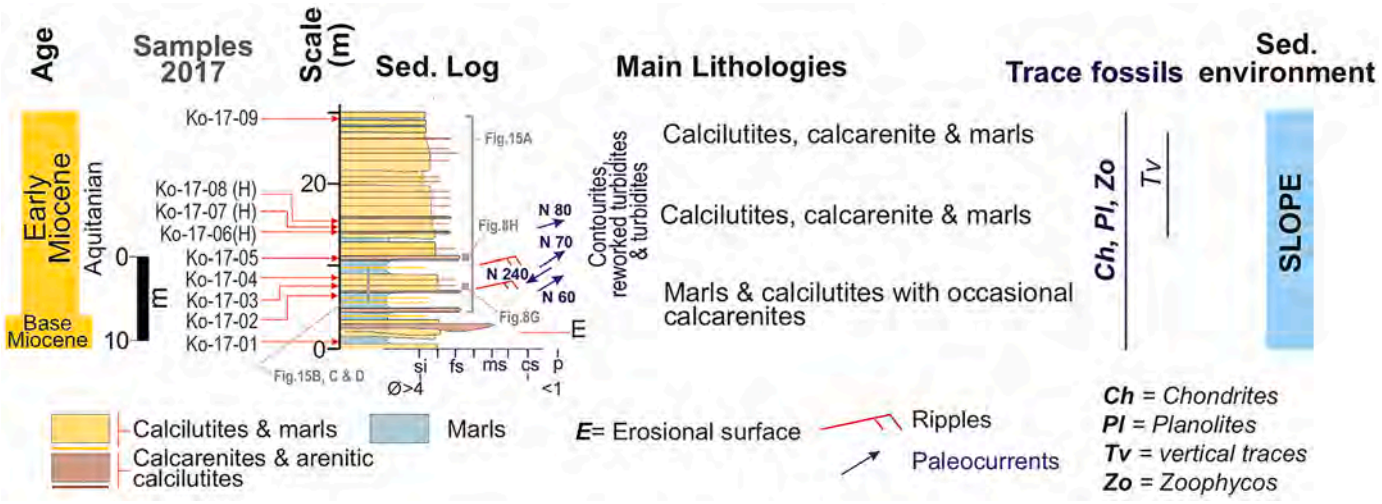

Fig. 14. Sedimentary log for the Korfi section (Pakhna Fm.) showing main lithologies, samples, paleocurrents, dominant trace fossils, and sedimentary environment interpretation.

finely crystalline calcite. Forams are replaced by sparry calcite or microspar. Recrystallisation or growth of sparry calcite can obscure depositional fabric.

Three samples from the Korfi location were analysed for chronostratigraphic ages (Table S1). They yielded abundant planktonic foraminifera with protracted age ranges. Abundant nannofossils, however, showed better preservation than that seen in samples from previous locations. Nannofossils consist mainly of the genus *Reticulofenestra* with less abundant specimens from the genera *Coccolithus* and *Sphenolithus*. Samples from the base of the section therefore appear to be Aquitanian (early Miocene) in age. Micropaleontological assemblages display pervasive reworking of predominantly Eocene and Oligocene aged planktonic foraminifera.

5.4. Kalavasos (K)

5.4.1. Section A

The lower section (Figs. 16, 17A) hosts beds striking 35°E and dipping 25°SE. It reaches around 30 m in thickness and hosts alternating white chalks and marl beds with regular occurrence of calcilutites and thin but persistent calcarenite beds of the Lefkara Fm. (Fig. 17B). Units appear whitish or light brown in colour and display occasional pressure solution features. These deposits and associated facies resemble the Beach section and section A at the Petra Tou Romiou locality.

The calcilutite beds range from 30 to 50 cm thick and correspond to facies F2a (Table 1). They alternate with fine-grained calcarenite beds (facies F3a, F3b) along sharp or gradational boundaries to form bigradational sequences (Fig. 17B). Microfacies analysis identified globigerinid wackestones (Fig. 8, Table 1) with prevalent bioclastic components consisting of ubiquitous planktonic foraminifera and subordinate radiolaria within a lime mud matrix. The carbonate matrix consists of nannofossil micrite primarily composed of coccoliths. The unit has occasional plane-parallel and rare cross-lamination. Calcarenite beds mainly correspond to facies F3a (Table 1). They appear white in colour, range from 5 to 8 cm thick, and have sharp or gradational boundaries with indistinct parallel- to cross-lamination and extensive bioturbation (Figs. 16, 17B, Table 2). Dominant microfacies include packstones to wackestones (occasionally grainstones) in which bioclasts consist of well-preserved planktonic foraminifera (mainly globigerinids) and radiolarians in a muddy and/or micrite matrix. Coarse-grained calcarenites of facies F3d (Table 1) do not appear at this locality. Paleocurrent measurement associated with facies F3a gave an average direction of N300 (NW).

5.4.2. Section B

Section B reaches about 55 m in thickness. Beds strike 40°E and dip around 25°SE. Samples show significant dolomitization and trace fossils (Fig. 16, Table 2).

As it belongs to the Lefkara Fm., the first 10 m of the package host lithologies similar to the section below. The Section B consists of alternating marls and chalks with three continuous chert beds clearly present at the top (Fig. 16). These deposits rest in a stratigraphic position similar to that of the cherts identified in the upper part of section A at the Petra Tou Romiou location. Above the chert beds, a 15-20 m interval displays similar lithologies but hosts more marly beds. The upper section shows facies F5 deformed structures (Fig. 16). Stratigraphically above these lithologies, an initial ~8 m interval of grey marls (facies F1, Table 1) with occasional calcilutites appears. Units above this marly unit vary in lithology relative to section A, which corresponds to the Pakhna Fm. Varied lithologies include calcilutites, calcarenites and marls (Figs. 16 and 18), although light grey to whitish calcilutites and marls predominate.

Calcilutites consist of facies F2a and F2c (Fig. 18 A-E, Table 1). They average about 20-30 cm in thickness, exceptionally reaching greater thicknesses (1–1.5 m; facies F2a). Facies F2a exhibits a homogenous fabric of sparsely packed planktonic foraminifera within a dominant but variable lime mud matrix that shows intensive bioturbation but no other sedimentary structures. Concentration of planktonic foraminifera can increase to become packstones similar to F3a (as in sample K17-10, Fig. 16). Facies F2a shows recrystallisation of bioclasts and matrix into microcrystalline calcite with significant dolomitization. Distinctive rhombic crystals appear within the mud matrix. The matrix includes <1% quartz in silt to very fine-grained sand grains. Facies F2c exhibits faint to pronounced layering of packed planktonic foraminifera within mud-dominated layers. Despite intensive bioturbation, units still display parallel lamination or occasional cross-lamination and wavy bedding. Reddish-brown coloration may result from iron oxides or iron-rich clays that become less common in upper parts of section B.

The dominant calcarenite beds correspond to facies F3a and F3b (Table 1) and show indistinct bed boundaries and a gradual transition to calcilutites. These facies comprises globigerinid packstones-grainstones with very low proportions of shallow-water bioclasts (F3b). At times they show well-preserved, parallel and cross-lamination, and only rarely cross-stratification (Fig. 18C). Measured paleocurrents in these layers indicate an average NNW flow direction, but with few subordinate SE measurements (Fig. 16). Section B contains no evidence of organised (facies F3d, F3e or F4) or disorganised (facies 5) intervals.

At about 75–78 m, the upper part of section B exhibits a remarkable

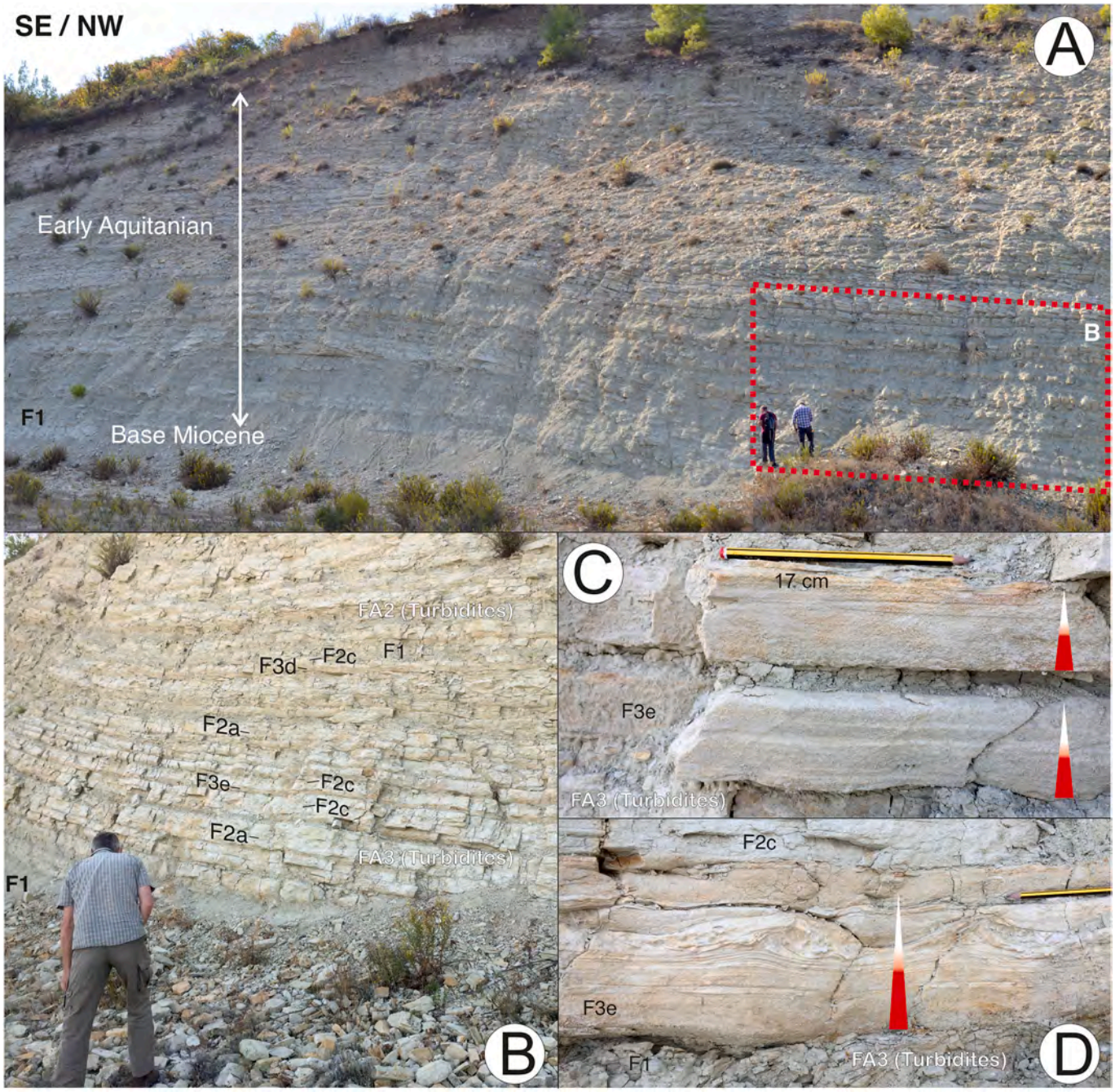

Fig. 15. A) and B) Korfi section (Pakhna Fm.) with dominant lithologies: marls (F1), calcilutites (F2a and F2c) and calcarenites (F3d and F3e); C) and D) Turbidite beds (F3e) with sharp-based boundary, normal grading, horizontal lamination, cross-lamination, convoluted lamination, and an occasional reworked top (FA3).

increase in marls among grey calcilutites and occasional calcarenites, along with clearly visible yellowish marls and reddish calcilutites (Figs. 16, 17D and 18D). Paleocurrent measurements in these facies gave an average flow direction of N310° (NW), similar to that recorded for section A.

5.4.3. Section C

This final section lies stratigraphically above section B, but their contact remains covered. Section C contains thin intervals (~5 m) of calcilutites and marls, as well as rare calcarenites (Fig. 18E), corresponding mainly to facies F1 and F2c (Table 1).

5.4.4. Age

Thirteen samples from the Kalavasos location were dated (Fig. 16 and Table S1). Section A samples gave Bartonian (middle Eocene) ages but showed a minor amount of early Eocene reworking. The lower part of the section B from the Lefkara Fm. —consisting of alternating marls, chalks and cherts (Fig. 16)— gave Bartonian to Priabonian (middle to late Eocene) ages. These samples contained early to middle Eocene reworked planktonic foraminifera and nannofossils. Samples located between chert horizons and deformed structures (Fig. 16) gave Priabonian (Eocene) and Rupelian-Chattian (late Oligocene) ages. The marly unit above the deformed deposits (Fig. 16) indicates an Aquitanian to Burdigalian (early Miocene) age. A sample from the base of the Pakhna Fm. suggests a Burdigalian to Langhian age (early to middle Miocene). This sample contained planktonic foraminifera of Eocene to Oligocene age, together with nannofossils representing reworked early Miocene taxa. Samples from the remaining section B are late Burdigalian to

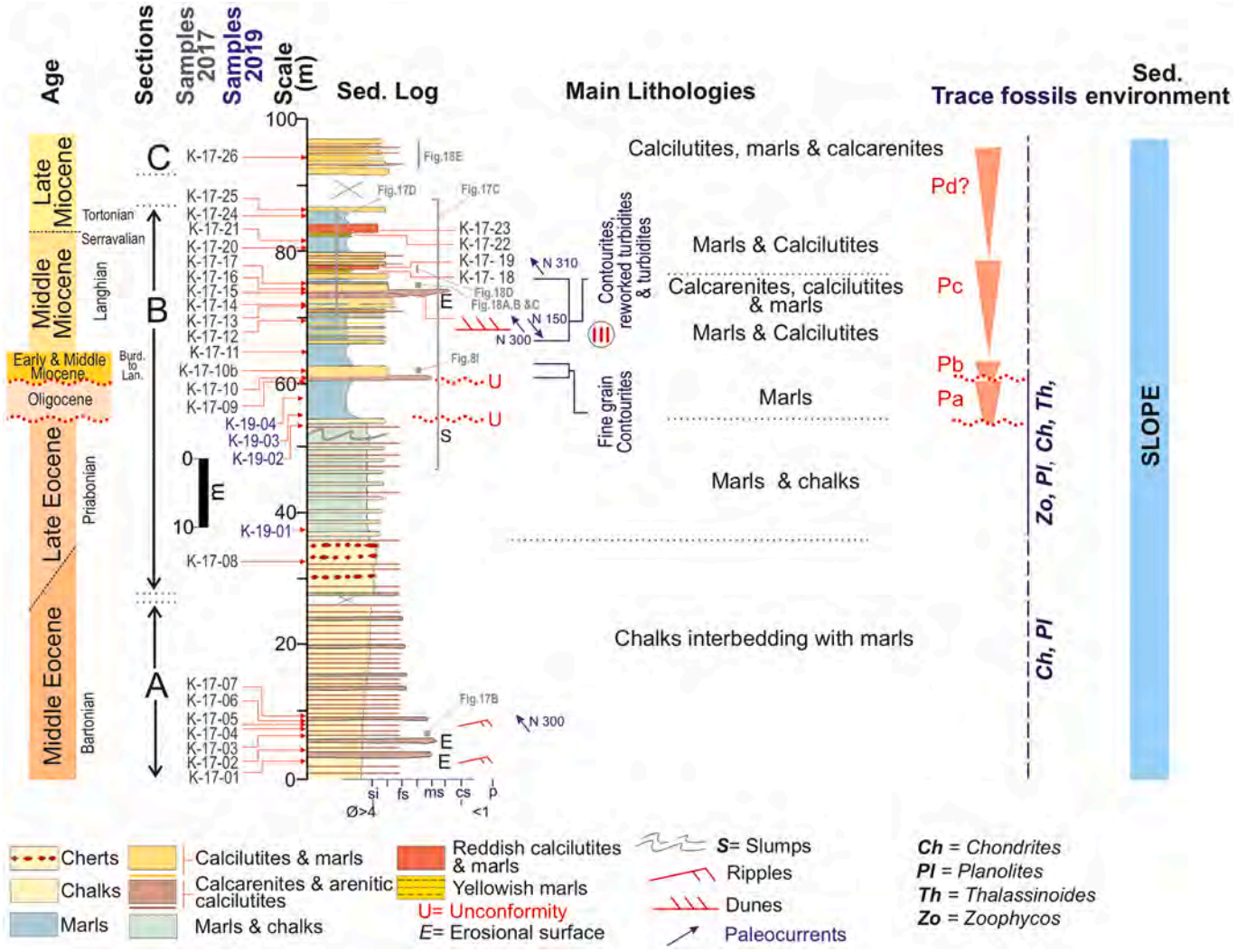

Fig. 16. Sedimentary log for the Kalavasos section including main lithologies, samples, paleocurrents, dominant trace fossils, and sedimentary environment interpretation. The stratigraphic position of the sandy contourite packages III is highlighted, and the four packages of strata (P) within the latest Oligocene to middle Miocene deposits are indicated by inverted red triangles: Pa) late Oligocene – base of Aquitanian; Pb) Aquitanian / Burdigalian; Pc) Burdigalian to Langhian; and Pd) Serravallian to Tortonian.

Langhian in age (Fig. 16). Samples showing the remarkable shift to yellowish and reddish colour (sample K-17-21; Fig. 18D) gave Serravallian (middle Miocene) ages. A sample from the top of section B (Figs. 16 and 18E) indicates a Tortonian (late Miocene) age.

Micropaleontological assemblages in Pakhna Fm. samples showed moderate degrees of reworking and contained predominantly Oligocene to early Miocene planktonic foraminifera. They also contained rare occurrences of Eocene species or even older nannofossils. The Serravalian samples contained reworked Cretaceous and Paleogene nannofossils. The Tortonian micropaleontological assemblage showed no evidence of reworking within the nannofossil assemblage, but included the shallow water benthic foraminiferid *Elphidium macellum*.

6. Interpretation

6.1. Interpretation of the sedimentary facies

6.1.1. Facies F1 (Marls)

Facies F1 consists primarily of marl deposits (Table 1). They signal a low energy depositional environment interpreted as vertical settling with slow lateral advection of very fine-grained terrigenous sediment through the water column. In the case of prevailing vertical settling processes, facies can be categorised as hemipelagic deposits (Hesse, 1975; O'Brien et al., 1980; Stow and Tabrez, 1998; Pickering and Hiscott, 2016) supplied primarily by the Troodos terrain (Eaton and Robertson, 1993).

Interstratification of these facies with F2a and/or F2c (increasing silt- and sand-sized grains) suggests fluctuations in carbonate (Hüneke and Henrich, 2011; Pickering and Hiscott, 2016) and terrigenous sediment supply by low-density and dilute turbidity currents and/or bottom nepheloid layer transport (Lowe, 1982; Stow and Wetzel, 1990; McCave and Hall, 2006). The former would reflect Bouma divisions Td and Te (Bouma, 1962).

6.1.2. Facies F2 (Calcilutites)

Facies F2 are calcilutites composed of nannofossil mud and well-preserved globigerinid tests. The absence of primary traction structures, poor sorting, and extensive bioturbation confer a wackestone texture with an indistinct mottled appearance (F2a). The texture is typical of pelagic biogenic (carbonate) oozes (Table 1) formed by deposition of pelagic sediment with low terrigenous input (Hüneke and Henrich, 2011). The trace fossil assemblage assigned to the *Zoophycos* ichnofacies (Table 2) supports the interpretation of a pelagic environment (Miguez-Salas and Rodríguez-Tovar, 2019a, 2019b). Facies F2

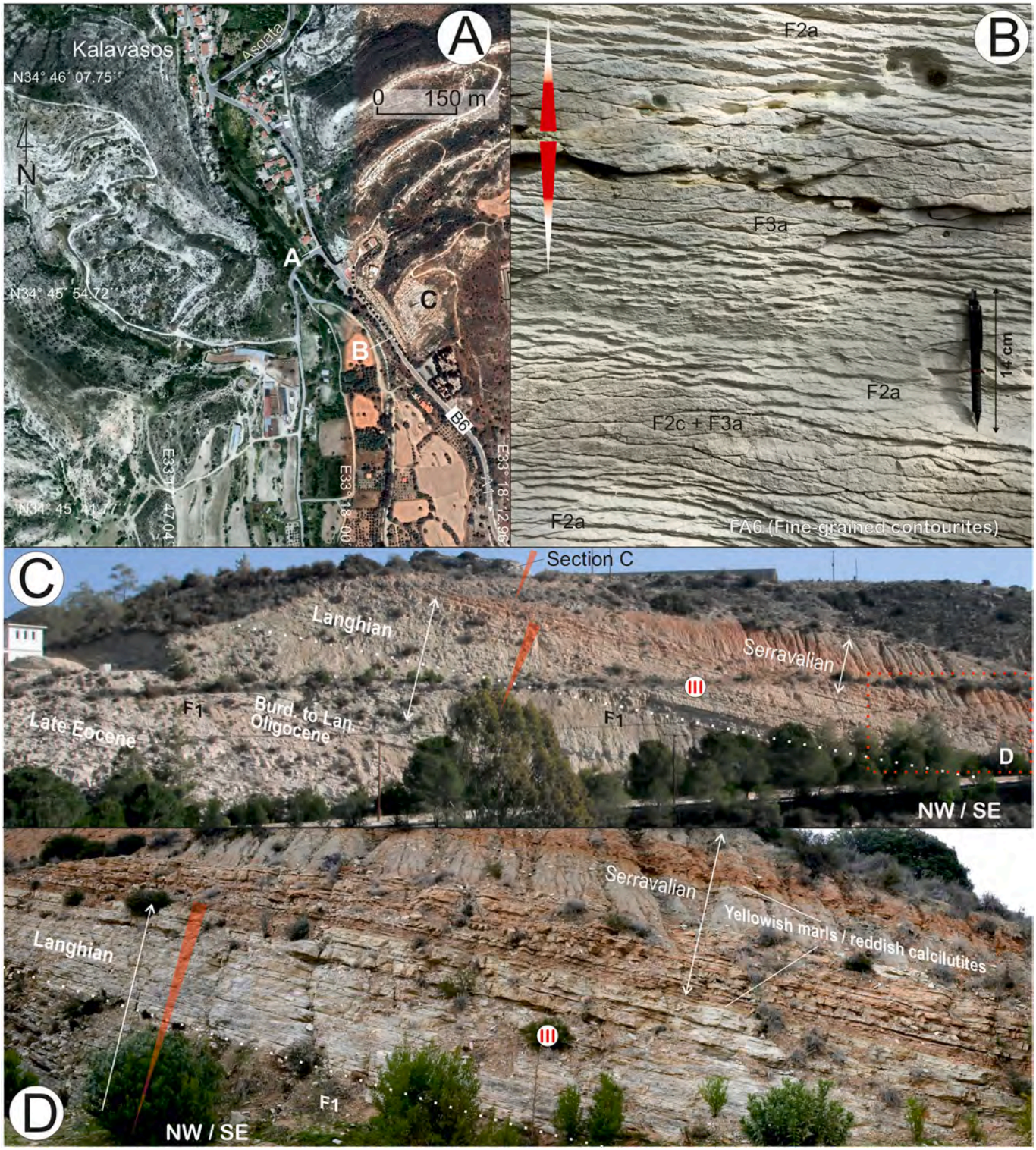

Fig. 17. A) Kalavasos section location indicating the positions of A, B and C sections; B) Example of sedimentary facies interpreted as fine grained contourites (FA6) with typical symmetric bi-gradational sedimentary sequences from calcilutites (F2a) to calcarenites (F3a) with gradual transitions; C) and D) Panorama of section B showing two packages of strata (P) within the latest Oligocene to middle Miocene deposits indicated by inverted red triangles: Pc) Burdigalian to Langhian; and Pd) Serravallian to Tortonian.

may also show evidence of hydrodynamic reworking. Some layers host bioclasts concentrated within packstone textures, centimeter-scale banding and lamination marked by subtle colour changes. These deposits may correspond to very fine-grained (muddy) contourites with facies similar to those described by previous authors (Stow and Smillie, 2020; de Castro et al., 2020, 2021a, 2021b; de Weger et al., 2021; Hüneke et al., 2021) who interpreted them as a silty contourite *sensu* Gonthier et al. (1984) or the C2 and C4 intervals of Stow and Faugères (2008). Muddy contourites are formed by very weak (<15-20 cm/s) bottom currents (McCave and Hall, 2006; Stow et al., 2009), but their centimeter-scale banding suggests intermittent bottom currents (Martín-Chivelet et al., 2008; Hüneke et al., 2021).

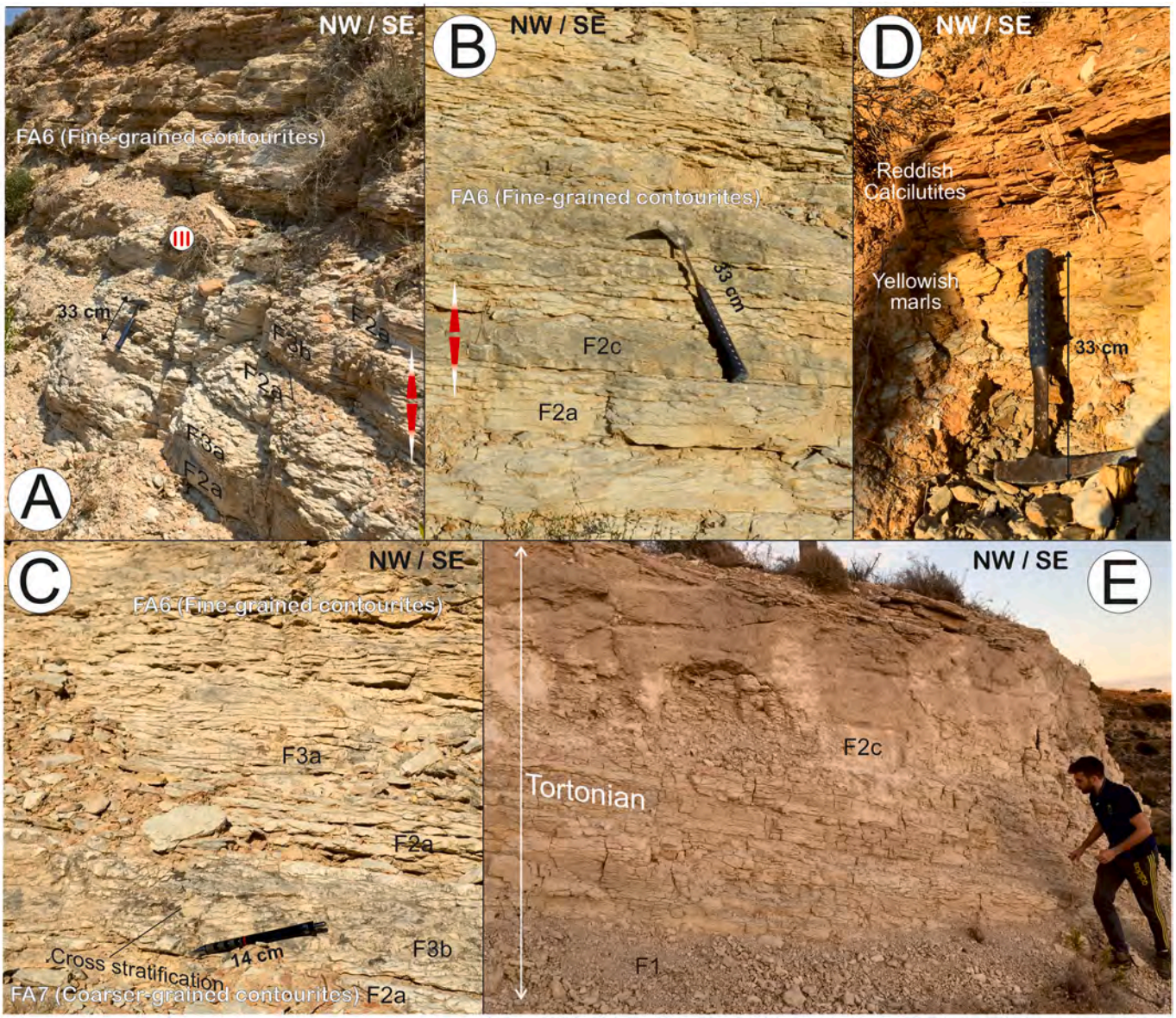

Fig. 18. A) Main sedimentary facies with alternating calcilutites (F2a) and persistent calcarenite (F3b) beds from section B of the Kalavasos (Pakhna Fm.) during the Langhian, with sedimentary facies interpreted as contourites (FA6); B) Sedimentary facies for calcilutites (F2a and F2c); C) Example of sedimentary facies interpreted as coarser-grained contourites (FA7) of the sandy contourite package III with typical symmetric bi-gradational sedimentary sequences from calcilutites (F2a) to calcarenites (F3b) and to calcilutites (F2a), with cross-stratification in the central division; D) Yellowish marls / reddish calcilutites at the top of section B; E) Marls (F1) and calcilutitic (F2c) Tortonian deposits in the upper part of section C.

Facies F2b resembles that of F2a, although the former takes on a greenish colour due to its illite (and quartz) content of up to 3%. Alteration and weathering of the mafic Troodos body (Eaton and Robertson, 1993) would be a potential source of very fine grain siliciclastic particles transported basinwards over long distances as sediment in suspension through nepheloid layers (Henrich and Hüneke, 2011). Bottom currents could then redistribute this material (e.g., Pudsey and Camerlenghi, 1998; Lucchi and Rebesco, 2007; Stow and Faugères, 2008; Rodrigues et al., 2022c).

Calcilutites from the whitish facies F2c preserve sedimentary structures (parallel lamination, cross-lamination or wavy bedding), but bioturbation can also disrupt them. This facies possesses lower clay content (<3%) and centimeter-scale banding or irregular lamination caused by variation in detrital clay content within relatively coarse-grained wackestones. The influence of weak and variable bottom currents in a slightly more energetic environment —as compared to F2a and F2b— indicates they may be contourites. Bottom currents appear to have eroded and deposited muddy contourites, thus indicating current velocities between 15 and 20 cm/s (McCave and Hall, 2006; Stow et al., 2009).

According to the above descriptions, facies F2 marks a gradational change from pure pelagic/hemipelagic (F1 and F2a and F2c) to fine grained (muddy) contourites (F2a, F2b and F2c) based on variation in the concentration and reworking of bioclasts (forams). Weak bottom currents could have converted wackestone textures into packstone. Criteria for differentiating purely pelagic/hemipelagic from fine-grained contourites are therefore quite subtle; their discernment calls for clear evidence of reworking and a concentration of bioclasts.

6.1.3. *Facies F3 (Calcarenites)*

The facies F3a, F3b and F3c represent calcarenites typical of sandy contourite deposits with internal wavy layering (Table 1). Calcarenites are a central division of the bi-gradational sequences of Gonthier et al. (1984) and would correspond to the C3 interval of Stow and Faugères

(2008). These facies present diagenetic pressure dissolution masking, in many cases masking the primary tractional structures.

Facies F3a consists of bioclast (globigerinid) wackestones-packstones distributed in typically thin (<10 cm), whitish beds with gradational boundaries, indistinct traction structures and extensive bioturbation (Fig. 5C). Particle composition exclusively of calcareous plankton shells indicates fine-grained, sandy bottom-current deposits that formed through an accumulation and reworking of pelagic sediments. Gradational contacts and traction structures signal a gradual transition in depositional conditions, under which fine-grained, sand-rich contourites form because of alternating suspension and reworking/winnowing of sediment —as opposed to episodic turbidity currents, which would show erosional basal contacts (Gonthier et al., 1984; Mutti, 1992; Shanmugam et al., 1993a, 1993b; Faugères and Stow, 2008; de Castro et al., 2020, 2021a; Hüneke et al., 2021).

Bottom currents concentrate foram tests (packstones) to generate sandy deposits (Fig. 8). Given their lower density, these medium-sand-grained bioclasts equate to coarse- or very course-grained silts, or even fine-grained quartz sands, in terms of critical flow velocities (Berger and Piper, 1972; McCave and Hall, 2006; Stow et al., 2009; McCave et al., 2017; Culp et al., 2021). Post-depositional reworking can lead to a calcarenite deposit from the reworking of forams (from initial calcilutites) given bottom current velocities of 15 to 20 cm s^{-1}. Currents with velocities of >25-30 cm s^{-1} would form sandy ripples and small dunes, however (McCave and Hall, 2006; Stow et al., 2009; Miramontes et al., 2021).

Facies F3b is characterised by whitish and greenish banding (Fig. 7). Spanning a few centimeters, the whitish bands consist of lenticular/wavy bedded calcarenites plus flaser traction structures associated with deposition of fine sand (Fig. 7B and C). Subsequent bioturbation and diagenetic alteration obscure primary sedimentary structures. Several lines of evidence suggest reworking by bottom currents. First, the packstone facies shows homogenous, well sorted bioclast distribution and grain-to-grain contact among planktonic foraminiferal tests of distinct intraparticle and interparticle matrix. Second, parallel- to cross-laminations indicate traction and bed-load transport. Finally, the units feature sharp boundaries and winnowing of the finest fraction. Greenish bands with higher proportions of terrigenous material (more clay-rich) correspond to episodic deposition of low-density, distal turbidites *sensu* Lowe (1982), which have not been winnowed. Alternatively, they could correspond to finer-grained suspension deposition from the bottom-nepheloid layer at periods of slightly reduced bottom-current velocities, where the clay (illite) is mainly transported in suspension and would not be deposited during peak flow conditions, when the whitish layers are deposited. Whitish bands reflect differential cementation during early stages of diagenesis, while compaction mainly affected the greenish bands.

The wavy layering most likely reflects relics of ripples migrating episodically over the seabed, leaving behind sets of parallel- and cross-laminated calcarenites. Facies with similar sedimentary structures described from ODP Leg 181 —sampling the Rekohu Drift in the SW Pacific— detected a light greenish and grey clay-bearing nannofossil chalk with flaser-like interbeds and laminae suggesting evidence of bottom current activity (Carter et al., 1999). Calcarenite layers document foraminiferal bedload deposition (current speeds >15 cm s^{-1}, McCave and Hall, 2006; McCave et al., 2017; Culp et al., 2021) or transport at higher current speeds (>40 cm s^{-1}) alternated with longer periods of intensified suspension settling from the nepheloid layer to eventually form the greenish bands. Beds of facies F3b can show cross-stratifications at its top, suggesting small, two dimensional, deep-marine dunes. Flow velocities for these beds never fell below threshold values for depositing and/or preserving calcilutites, hence specific velocities ranging from ~ 20 to 100 cm s^{-1} (Stow et al., 2009). Such conditions can occur along the slope, where higher energies are obtained. Ichnological data from facies F3b (Table 2) indicate interrupted sedimentation with intervals of condensation during deposition. Discrete burrows and especially *Planolites* (Fig. 7B and C) show that these interruptions signal discontinuous deposition allowing simultaneous bioturbation of *Planolites* (shallow tier structures) at, or slightly below, the seafloor (Rodríguez-Tovar et al., 2019a, 2019b). The banded facies might thus offer evidence of reworking after turbiditic deposition by intermittent and relatively vigorous bottom currents with alternating suspension and traction processes (Shanmugam, 2000; Ito, 2002; Capella et al., 2017; de Castro et al., 2021a; de Weger et al., 2021; Hüneke et al., 2021).

Facies F3c consists of greenish calcarenites with internal wavy layering forming thick (up to 60 cm) beds and bed sets of bioclastic sandy contourites (Fig. 7A). They contain globigerinid packstones-grainstones showing clear particle support and a low mud content (but higher mud proportions than F3a and F3b) as a result of sorting during bottom-current induced sediment transport and deposition.

Researchers have traditionally classified contourite deposits exclusively according to their lithology and texture (e.g., Gonthier et al., 1984; Shanmugam, 2006, 2012, 2017; Stow and Faugères, 2008; Brackenridge et al., 2018; de Castro et al., 2021a). In view of these classifications, the calcarenite facies F3a, F3b and F3c qualify as sandy bioclastic contourites and have been referred as “globigerinid sands”, “planktonic foram calcarenite”, "sandy muds", “reworked pelagic sediment” or “winnowed marl ooze” (Schiller et al., 1994). A similar contouritic deposit has been documented in onshore deposits of Indonesia (Schiller et al., 1994) and in different modern ocean environments in the Atlantic (McCave et al., 1980; Mullins et al., 1980), the Mozambique Margin (Babonneau et al., 2022) and Pacific (Lonsdale and Malfait, 1974; Lonsdale, 1981). Indonesian deposits include Pliocene East Java and Madura basins, which host calcarenite deposits of 20-50 m thickness and with decimeter-scale cemented and uncemented beds whose composition, sedimentary structures and ichnofacies (Schiller et al., 1994) are similar to those described here for the Cyprus locality.

The lime mud from aforementioned contourite deposits appears homogeneous with poor definition because of dissolution and recrystallisation. Foraminifera observed in thin sections (Fig. 8) appear only as numerous, faint, globular forms that are often partially replaced by microcrystalline calcite, and even by dolomite in a few cases (Fig. 9). The components of the lime mud matrix are distributed several microns apart; they appear as amorphous or show terminations suggesting recrystallised calcite. Others display a microstructure suggestive of coccoliths of other bioclastic fragments (Fig. 9).

Facies F3d and F3e may represent turbidites (Table 1). In general, the criteria for turbidite identification in studied outcrops includes: a) organised to massive bedding, b) normal grading of Tb to Td intervals in the Bouma sequence, c) shallow marine particle composition, and d) bioturbation only at the top of beds. The turbidites of both F3d and F3e are much better sorted than the contourite facies, and moreover particle-supported. Deposits contain allochthonous shallow marine bioclasts transported from adjacent shelves, as well as allochthonous deep-marine bioclasts (mainly globigerinid forams) from the slope that underwent reworking and transport due to erosion by turbidity currents or mass transport processes. Specifically, the F3d facies do not have a composition referable to shallow-marine environments; these turbidites must be supplied from the slope.

Facies F3d exhibits a sharp base and a gradual top boundary Calcarenite beds of < 10 cm form fining-upward sequences (normal grading) with well-preserved primary traction structures (parallel- and cross-lamination). This facies predominates during the Eocene. The upper gradational boundary may also show more abrupt changes in grain size or even local reworking. The sharp basal contact, plus the well- to very well-sorted, normal graded beds and internal structures, would indicate decelerating turbulent flow suspension fallout (e.g., Bouma, 1962). The facies is therefore interpreted as very low or low density turbidites (Lowe, 1982; Postma, 1986; Stanley, 1987, 1988, 1993; Stow and Wetzel, 1990; Sparks et al., 1993; de Castro et al., 2020, 2021a; de Weger et al., 2021; Hüneke et al., 2021) from the slope that

incorporated previous pelagic deposits and contourite deposits, thus containing very small percentages of shallow water materials. They document minor shallow marine sedimentary input compared to the deep-marine input. The normal grading upwards, resembling the Ta division of the Bouma sequence, indicates deposition by suspension, while the upper parallel-and cross-lamination is linked to Tb and Tc in the Bouma sequence (Bouma, 1962). Bioturbation occurs primarily toward the top of the unit (Miguez-Salas and Rodríguez-Tovar, 2021). Bottom currents affected some turbidites after their deposition, since the sediments are frequently missing the Tc, Td and Te intervals; they show signs of reworking at the top (Stanley, 1987, 1988, 1993; de Castro et al., 2020, 2021a) or even reworking of the entire bed. In these cases, the eroded turbidite beds are preserved only in burrow fills below the erosional surface (Rodríguez-Tovar et al., 2019a).

Facies F3e beds show normal grading with a sharp-base and a planar to gradual upper boundary, or else sharp and irregular upper surfaces with common wavy lamination (Fig. 13c and D). This facies reaches up to 20 cm in thickness and predominates during the latest Oligocene and Miocene. The well- to very well-sorted, normally graded beds and internal structures likely reflect decelerating turbulent flow suspension fallout (e.g., Bouma, 1962). These deposits are interpreted as turbidites transported from shallow marine (shelf) carbonate depositional environments with substantial additional input from upper slope settings. Normal grading and particle composition reveal fully turbulent flows enriched with bioclasts (globigerinids) and rip-up clasts due to erosion under waxing flow conditions across the slope.

6.1.4. Facies F4 (Calcirudites)

Facies F4 occurs within the late Oligocene to early Miocene deposits and consists of coarse-grained bioclastic rudstones with a sharp base and normal grading, indicating deposition by density flows. The beds contain abundant shallow marine fossils, meaning sediment was sourced from shelf environments. The facies is interpreted as deposited by higher density turbidites (Mulder and Alexander, 2001; Mulder, 2011; Hüneke et al., 2021) equivalent to the Ta Bouma sequence (Bouma, 1962). Local presence of *Helminthorhaphe* (Table 2) supports a turbiditic character (Rodríguez-Tovar et al., 2020). Accordingly, these turbiditic deposits show sharp, irregular and truncated upper boundaries that indicate erosion and/or reworking by bottom currents, as proposed by previous authors for similar deposits in other areas (Lee and Ogawa, 1998; Stanley, 1988; Ito, 2002; Gong et al., 2016; de Castro et al., 2020, 2021a; de Weger et al., 2021). The deposits initially initially consisted of shallow-marine carbonate material from the continental shelf and slope. Turbidite beds were reworked after their initial deposition by bottom currents across the slope (Fig. 7A). The current would have formed sand-rich deposits during intervals of higher current speed, and winnowed the fine-grained particles during intervals of lower current speeds (Lucchi et al., 2002; Lucchi and Rebesco, 2007).

6.1.5. Facies F5 (Deformed, amalgamated marls, calcilutites and calcarenites)

Eocene, Oligocene and especially Miocene sediments show evidence of slumps and debris flows. These consist of alternating beds of marls, calcilutites and calcarenites having different degrees of bed-internal deformation. The geometry of F5 slump deposits (Fig. 12B) shows a downslope, a S-to-SW oriented migration component. The facies is both underlain and overlain by normally bedded units composed of similar sediment types. Deformed beds in F5 indicate transitions between non-cohesive and cohesive behaviours or superimposed mass-transport processes (Shanmugam, 2006; Haughton et al., 2009). Slumps can evolve to turbidity currents owing to ambient water entrainment, or when they encounter hydraulic jumps along the margin (Wright and Anderson, 1982; Larter and Cunningham, 1993; Shanmugam, 2019). This interaction funnels flow downward, leading to seafloor erosion, sediment bypass, and distal deposition of coarse- to fine-grained deposits (Mutti, 1992; Fonnesu et al., 2020).

6.2. Interpretation of sedimentary facies associations: decoding sedimentary environments

The sedimentary facies described here form distinct facies associations (FA), which help elucidate sedimentary environments recorded by the Cyprus sections. These environments occurred in well oxygenated, normal, open marine conditions and relatively low-energy marine environments in abyssal to bathyal (deepwater) zones, except the upper part of the sedimentary record in Agios Konstantinos and Korfi sections, where episodic input of sediment from shallower depositional settings signal lower or more variable salinity (Table S1).

6.2.1. Pelagic/hemipelagic deposits (FA1)

The fine-grained sediments of facies F1 and F2 are grouped into FA1. F1 predominates and is associated with F2a/F2c. The fine-grained marine sediment of facies association FA1 shows subtle changes in composition interpreted as the interactions between pelagic/hemipelagic, low-density turbiditic and weak bottom-current induced sedimentation. Pelagic settling was also an important background process during this time. Fluctuations in bottom current activity caused fluctuations in contouritic and hemipelagic sedimentation. Similar facies associations have been described along continental margins in modern and ancient sedimentary records (Pickering and Hiscott, 2016; Stow and Smillie, 2020; de Castro et al., 2021a; de Weger et al., 2021).

6.2.2. Turbidites (FA2, FA3 and FA4)

Turbidites typically result from short-lived, rapid depositional events that temporarily interrupt the normal activity of bottom-dwelling organisms (Bouma, 1962; Stow and Shanmugam, 1980; Lowe, 1982; Mulder, 2011; Mulder and Hüneke, 2014). Turbidity currents usually carry coarse-grained particles at the base and head of a flow, whereas fine-grained particles are transported within a turbulent suspension cloud (Bouma, 1962; Mutti, 1992, 2011). A single turbidity current can deposit a sequence having up to five internal divisions, Ta to Te, according to the Bouma sequence model (Bouma, 1962). From base to top, the five divisions of the Bouma model comprise a massive, normally graded gravelly-to-sandy unit with an erosional base (Ta) overlain by a sandy unit with parallel laminae (Tb) and a sandy-to-silty unit with current ripples (Tc), followed by a silty unit with upper parallel laminae (Td), and terminating in structureless or laminated mud (Te) (Bouma, 1962; Mutti, 2011). Each division is deposited either by suspension (Ta, Td, Te) or traction (Tb,Tc) sedimentation. The five divisions represent a waning flow and result from flow instability, yet might be caused by flow non-uniformity. Three facies associations were recognized in the studied sections:

- Facies F3d is associated with F2, and more specifically F2a and F2c. Together they represent the facies association FA2. The erosional bases and wavy or parallel laminations —which would include Td to Te divisions— represent very low density turbiditic flows in distal settings (Stow and Shanmugam, 1980; Stow and Wetzel, 1990).
- Facies F3e associates with F2 and specifically F2c. Together they form facies association FA3. FA3 includes Tc or Td to Te divisions for fine-grained turbidites, but thicker deposits having distinctive normal grading and commonly well developed scour marks their base occur as well. Altogether, FA3 reflects low density turbiditic flows (Bouma, 1962; Walker, 1965; Mutti, 2011) in a more proximal setting and/or thicker turbiditic flows relative to FA2.
- Facies F4 commonly relates to facies F3b or F2a to form facies association FA4 for medium-grained and thicker turbidites. FA4 includes the divisions Ta to Tb caused by loss of energy in turbulent flows, and representing higher density turbiditic flows and/or more proximal settings (Bouma, 1962; Walker, 1965; Lowe, 1982; Mutti, 2011) in comparison to FA2 and FA3. In those cases where F4 evolves into F3b, evidence of a reworked top of the turbidites by bottom currents could explain the lack of fine-grained fractions, generating

bottom current reworked sands (BCRS) as the result of bottom current reworking processes (Stanley, 1988; Shanmugam et al., 1993a, 1993b; Viana et al., 1998; Ito, 2002; Mutti et al., 2014; de Castro et al., 2020, 2021a; Fonnesu et al., 2020). Partial reworking of a turbidite division (usually the top) with only minor sediment transport would qualify as BCRS. BCRS may or may not include a component of lateral displacement and they usually appear in contourite drifts (de Castro et al., 2020, 2021a; de Weger et al., 2021) or mixed systems (Shanmugam et al., 1993a, 1993b; Fonnesu et al., 2020; Fuhrmann et al., 2020; Rodrigues et al., 2022a). Mutti et al. (2014) also defined a facies association similar to BCRS in which genetically distinct processes (turbidity currents and bottom currents) produce vertically and laterally associated facies. Most of these reworked sands show only minor bioturbation, but *Planolites* is commonly present in cases of low-sedimentation rate or discontinuous sedimentation (Rodríguez-Tovar et al., 2019a, 2019b).

The FA for turbidites include incomplete sequences, as they show only the lower or upper divisions of the theoretical Bouma sequence model (Bouma, 1962). Indeed, complete sequences of turbidites are rare. The incomplete turbiditic sequences described here are typical especially in terms of calcilutite turbidites in which silt-laminated divisions appear less distinct when compared to the equivalent siliciclastic turbidite deposits (Piper and Stow, 1991; Stow and Piper, 1984). The Eocene to Miocene deposits from Cyprus lack calcareous silt divisions (Hüneke et al., 2021) and the main components of turbidites (and contourites) are sand- to coarse-silt-sized bioclastic fragments (essentially globigerinids) and nano-sized coccoliths. Coarser turbidites occasionally include shallow marine components yet still host predominantly intra-basin bioclastic components. The lack of calcareous silt particles mainly reflects carbonate sources, indicating that organisms producing silt-sized material were not abundant (Hüneke et al., 2021).

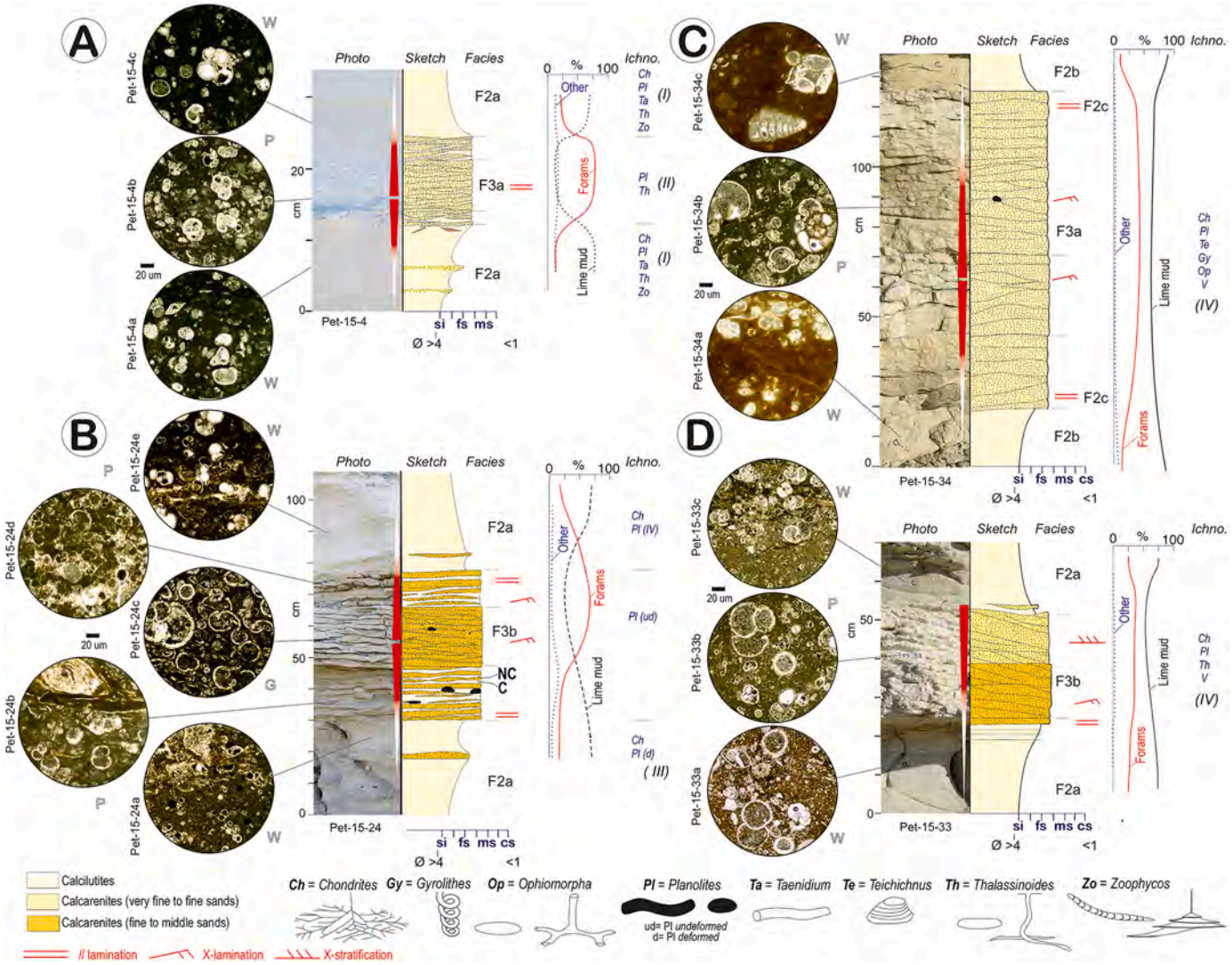

Fig. 19. Key examples of different bi-gradational sequences for the Lefkara (A) and Pakhna (B, C and D) formations. A) Bi-gradational sequences for fine-grained contourites with typical bi-gradational sedimentary sequences from calcilutites (F2a) to calcarenites (F3a) and to calcilutites (F2a) with gradual transitions; B) Bi-gradational sequences for coarser-grained contourites (package I, Chattian, late Oligocene and package II, Aquitanian/Burdigalian, early Miocene) with typical symmetric bi-gradational sedimentary sequences from calcilutites (F2a) to calcarenites (F3b) and to calcilutites (F2a). The central division (F3b) contains non-compacted (NC) and compacted layers (C) with planar and wavy to lenticular beds; C) Bi-gradational sequences for coarser-grained contourites (package III, Langhian, middle Miocene) with typical bi-gradational sedimentary sequences from calcilutites (F2a) to calcarenites (F3a) and to calcilutites (F2a); D) Asymmetric bi-gradational sequences for packages II and III where the central calcarenite (F3b) division bedforms evolve from parallel planar or wavy to lenticular beds, to cross-stratification indicating sandy ripples that evolved into small dunes on the top.

6.2.3. Mass transport deposits (FA5)

FA5 represents turbidite facies associations between pelagic/hemipelagic and contourite features that include mass transport deposits, MTDs (FA5). The stratigraphic position of large MTDs depends primarily on unconformities. Although they have been described in the literature (e.g., Farrell and Eaton, 1987; Lee and Stow, 2007; Lord et al., 2009), MTDs identified at the present study locality were smaller than those reported by Lord et al. (2009). The paleocurrents from turbidites and MTDs mainly indicate transport from the north, as reported by Eaton and Robertson (1993).

6.2.4. Bottom current (contourite) deposits (FA6 and FA7): symmetric and asymmetric bi-gradational sequences

The sections analysed show evidence of Eocene to middle Miocene bottom current deposits with two main facies associations that determine several types of bi-gradational sequences.

Facies F3a and F2a are associated in bi-gradational sequences and thus comprise FA6 with gradational boundaries between facies. On occasion these sequences incorporate F2c instead of F2a. The facies association FA6 documents a bi-gradational sedimentary sequence for finer grained contourites in the Lefkara Fm. (Fig. 19A) during the Eocene to middle Miocene. These sequences have a gradual transition from calcilutites (F2a) to calcarenites (F3a) to calcilutites (F2a) and are identified based on the absence of compacted and non-compacted layers in the central division (Fig. 19A), where amalgamated and sometimes lenticular beds may appear (Fig. 19A), respectively exhibiting parallel and occasional cross-lamination.

Facies F3b are associated with F2b, representing a facies association FA7 for coarser grained (sandier) contourites in the Pakhna Fm. These deposits are tabular, with dominant paleocurrents trending SE; the Lefkara Fm. paleocurrents trend in an opposite direction. The sandier contourites appear in three packages (I, II and III). Package I is Chattian (late Oligocene), package II is Aquitanian / Burdigalian (early Miocene), and package III is Langhian (middle Miocene) in age. In Petra Tou Romiou sections, the contourite beds found in early Miocene package II appear thinner than those of package III (middle Miocene). The occurrence of package II was previously suggested by Eaton and Robertson (1993) and moreover described as well sorted globigerinid grainstones/packstones with minor silt-sized quartz. This package was likewise identified by Kähler (1994), Kähler and Stow (1998) and Stow et al. (2002b), but erroneously included as part of the upper Lefkara Fm.

Three types of bi-gradational sequences can be determined in the Pakhna Fm., marking complete symmetric bi-gradational sequences (Fig. 19B and C) or incomplete asymmetric bi-gradational sequences (Figs. 5C, 7B and E, 10D and 19). Occasionally, these sequences incorporate F3c instead of F3b, or F2a or F2c instead of F2b.

- Coarser-grained contourites (packages I and II, Fig. 19B) typically appear as symmetric bi-gradational sedimentary sequences from calcilutites (F2a) to calcarenites (F3b) and to calcilutites (F2a). The central division (F3b) of these sequences contains non-compacted and compacted interlayers with planar and wavy to lenticular beds. The beds at the base of the central division appear as planar surfaces with horizontal laminations that transition to wavy and lenticular beds then back to horizontal laminations as at the top (Fig. 19B). The base and top of these sequences show thick compacted beds relative to those of the central division, which are much thinner. Non-compacted beds may be amalgamated. Both the distribution of bed forms and reduction in compacted bed thickness indicate an increase and subsequent decrease in bottom currents during the time of formation of the central division.
- Bi-gradational sequences for coarser-grained contourites (package III) appear as typical sequences from calcilutites (F2a) to calcarenites (F3a but ocassionally F3b) and to calcilutites (F2a). They show a thicker, homogenous, central calcarenite interval (Fig. 19C) in comparison with those of package II, but without the non-compacted or compacted layers. Wavy to lenticular beds amalgamate to show parallel and cross-laminations.
- Asymmetric bi-gradational sequences for packages II and III (Fig. 19D) appear as top-cut sequences for which the calcarenite (F3b) division transitions: from parallel, planar and wavy to lenticular beds into cross-stratification indicative of sandy ripples and sandy dunes at the top of the central division. The main difference between the bi-gradational sequences in packages II and III is the absence of non-compacted or compacted layers in III. The distribution of bedforms suggests an increase in bottom currents during deposition of the central division.

Standard symmetric bi-gradational sequences include calcilutite-calcarenite-calcilutite cycles in FA6 and FA7. Coarsening-upward (from globigerinid wackestones to globigerinid packstones) and fining-upward sequences (from globigerinid packstones to globigerinid wackestones) are comparable with the standard sequence defined by Faugères et al. (1984) and Gonthier et al. (1984). Contourites that first coarse upwards and then fine upward mark an increase and subsequent decrease in bottom-current velocities along with temporal variation in local sediment supply (Faugères et al., 1984; Gonthier et al., 1984; Martín-Chivelet et al., 2008; McCave, 2008; Stow and Faugères, 2008; Rebesco et al., 2014). Faugères and Stow (2008) defined five intervals (C1 to C5) in the contourite sequence proposed by Gonthier et al. (1984), wherein C3 represents the central calcarenites facies (F3a, F3b or F3c), and calcilutites (F2a, F2b and F2c) correspond to intervals C1 and C5. Intervals C2 and C4 consist primarily of silt-sized particles, but these calcilutite deposits do not appear among Cyprus contourites, given the lack of organisms producing silt-sized sediment and the low grade of shell fragmentation (Hüneke et al., 2021).

In bi-gradational sequences, the sandier central interval (C3) documents enhanced bottom currents. The observed banding with the cemented (non-compacted) and compacted layers described in F3b and F3c signals alternation between increasing siliciclastic material in the green bands (more suspension fallout) and pure carbonate in the white bands, with lenticular, flaser and parallel layering (sandy contourites). The occurrence of non-compacted and compacted layers depends on the abundance of clay and muddy lime and of carbonates bioclasts, and is controlled by sorting. Higher percentages of clay and muddy lime in basal areas may decline by the central and upper part of the central division (Fig. 19). The percentage of forams is low at the base of the central division, then increases slightly toward the middle and upper parts (Fig. 19). This suggests grain size sorting processes. Bioclastic particles other than forams (including shallow marine bioclasts) become more abundant in the lower part of the central division of the F3b of bi-gradational sequence B (Fig. 19B). This indicates intensified reworking of previous turbiditic deposits. These non-compacted and compacted layers could be interpreted as a heterolitic fabric resulting from repeated shifts between suspension fallout and bedload deposition. Alternations suggest short-term fluctuations in bottom current speed, and gravity sediment supply, in agreement with ichnological analysis. They may indicate interruptions in sedimentation, low sedimentation rates, omission surfaces, or sedimentary condensation (Föllmi, 2016; Rodríguez-Tovar et al., 2019a). When bottom currents become weak, turbidity and suspension settling determine deposition. Alternatively, coexisting turbidite-contourite deposition occurs with transport of suspended, fine-grained sediments or the reworking of turbidites by stronger bottom currents that can transport sediments along slope, and then deposit them further as contourite drifts (Creaser et al., 2017; de Castro et al., 2020, 2021a; Rodrigues et al., 2022c).

The standard bi-gradational sequence is widely used as a diagnostic framework for modern and ancient bottom current and contourite mounded drift deposits (Duan et al., 1993; Balaky and Tamar-Agha, 2017; Capella et al., 2017; Brackenridge et al., 2018; Rodríguez-Tovar et al., 2019a, 2019b; Li et al., 2020; Zhang et al., 2020; de Castro et al., 2021a; de Weger et al., 2021; Hüneke et al., 2021). Consequently, FA6

and FA7 stand as partial depositional features of a contourite system. As described above, some sequences in FA7 represent incomplete, asymmetric bi-gradational sequences (Figs. 10 and 19). In these cases, the central interval consists of either horizontal lamination or cross-lamination within lenticular beds (ripples) in the lower part. Cross-stratification at the top of the unit suggests small two-dimensional (2D) dunes, with a more net contact to F2 calcilutites facies above. Such asymmetric bi-gradational sequences may thus be interpreted as a "top-cut contourite sequence". They appear at the top of packages II and II, and may be seen as diagnostic features of distal zone contourite terraces with higher bottom current energy conditions (>25 cm s^{-1}) than the ones commonly observed for contourite drifts and sedimentary dunes (Viana and Faugères, 1998; Thieblemont et al., 2019; Miramontes et al., 2020; Miramontes et al., 2021; de Castro et al., 2021b).

7. Discussion

7.1. Stratigraphic, sedimentological and age considerations

7.1.1. Marly unit at the top of the Lefkara Fm. and the boundary between the Pakhna and Lefkara Fms

The marly unit at the top of the Lefkara Fm., and stratigraphically below the Pakhna Fm. (Figs. 6E and 12A), shows variable sedimentary thickness. This unit provides valuable regional stratigraphic constraint and likely corresponds to the upper marly unit at the top of the Lefkara Fm. as defined by Robertson and Hudson (1974) and Robertson (1976). Samples from this unit in Agios Konstantinos gave early Rupelian (early Oligocene) ages. Samples from Petra-Tou Romiou gave late Rupelian and Chattian (late Oligocene) ages, while samples from Kalavasos gave Aquitanian (early Miocene) ages, thus demonstrating the degree of regional diachroneity of the marly unit as noted by Kähler (1994). Similar Oligocene marl deposits commonly appear around the Mediterranean (e.g., Rögl, 1998, 1999; Hawie et al., 2013).

The contact between the Pakhna and Lefkara Fms. SE of Agios Nikolaos is Chattian (late Oligocene, ~ 28 to 23 Ma) in age. This contact in the Petra Tou Romiou section is latest Aquitanian – early Burdigalian (early Miocene, between ~ 21 to 19.5 Ma). The contact in the Kalavasos section is Burdigalian to Langhian in age (early to middle Miocene, ~ 18 to 15 Ma). These results indicate that the base of the Pakhna Fm. is regionally diachronous, as suggested by Eaton and Robertson (1993), but in disagreement with Kähler (1994), who assigned a Burdigalian age to this regional boundary. The results reported here indicate that this boundary is older (latest Oligocene) among landward positions closer to the Troodos Massif (inner margin position), whereas it is younger (Burdigalian-Langhian) in basinward positions (distal margin position). At the Petra Tou Romiou locality, the boundary between the Pakhna and Lefkara Fms. appears as an unconformity between the Oligocene marls and sandy (calcarenite) contourites (Fig. 7G).

7.1.2. Lefkara Fm

The studied sections correspond primarily to the middle and upper Lefkara Fm. defined by Robertson and Hudson (1974), Robertson (1976) and Eaton and Robertson (1993). In the sections described here, chert beds below the marly unit and at the top of the Lefkara Fm. lie at the same stratigraphic position and can serve as a regional stratigraphic marker horizon (Figs. 4 and 16). The dominant sedimentary facies association for this Eocene to Oligocene formation includes hemipelagic/pelagic, fine grained turbidites from dilute turbiditic flows, and fine grained contourites formed by weak paleocurrents trending NW. These facies eventually become locally disorganised and mixed within mass transport deposits (MTDs). Facies associations based on microfacies, microfossil data and ichnological features indicate deep-marine environments dominated by carbonate pelagic (chalk) sediments as previously proposed (Eaton and Robertson, 1993; Lord et al., 2009). A distal, bathyal (lower slope) sedimentary environment reflecting normal open marine conditions comports with the interpretation of Kähler (1994), who proposed that deposition took place around the Calcite Compensation Depth (CCD) at 2 to 3 km water depth.

Sedimentological and tectonic characteristics of the Lefkara Fm. suggest that the paleomargin was a wide sedimentary basin of uniform thickness that inclined gently seaward. The sloping basin covered previous Cretaceous deposits and shows local displacement by extensional faults. Following Dickinson's simple classification scheme for slope (forearc) basin morphology within active margins (Dickinson, 1995), its characteristics represent the incipient phase of slope basin development as suggested by further authors (Shimamura, 1995; Takano et al., 2013). Dominant pelagic and hemipelagic sediment includes intercalations of thin-bedded turbidites and muddy contourite deposits. They suggest intermittent, but frequent, low-density turbiditic and along-slope bottom currents transporting fine-grained material.

7.1.3. Pakhna Fm

The Pakhna Fm. hosts facies associations similar to those defined by Eaton and Robertson (1993). In addition to an increase in average grain size, thicker and more common high-density turbidites, debrites and slump deposits coexist with coarser (sandy) contourites and hemipelagic/pelagic deposits. Data did not show evidence of submarine canyons within the study intervals, although Eaton and Robertson (1993) reported late Miocene canyons at the Tokhni locality (East of the Kalavasos section. Fig. 2). The older basal age (latest Oligocene) closer to the Troodos Massif ophiolites (inner margin position), the younger (Burdigalian-Langhian) basinward surface (distal margin position), and increased sedimentation rate (Lord et al., 2009) suggest a prograding continental margin during Pakhna Fm's deposition. The Pakhna Fm. does not offer distinctive marker horizons like the Lefkara Fm.; it does, however, evidence development of marly deposits between sandier contourite packages I and II, and II and III (Figs. 4, 11, 16), which can help constrain stratigraphic orientation.

During the Pakhna Fm. deposition, the regional paleo-slope dipped toward the south/southwest but was divided into a number of minor slope basins due to active northward subduction along the margin (Eaton and Robertson, 1993). The observed structure and depositional features support the interpretation of a compressional setting and unstable continental slope, wherein the common occurrence of redeposited bioclastic sediments —as well as the frequent occurrence of turbidites and MTDs— record synsedimentary tectonic activity. Facies and facies associations indicate deep-marine sedimentary environments within normal, oxic, open marine conditions. The vertical facies and ichnological features, along with the increase of benthic foraminifera in this formation, would however indicate a more proximal and shallower (middle to upper slope) setting as compared to the Lefkara Fm. These associations show long-term variation from deepwater, pelagic carbonates that transition into shallow water bioclastic and terrigenous sediment, as noted by previous authors (Robertson, 1977; Eaton and Robertson, 1993; Kinnaird, 2008). Miocene fossils suggest episodic input of redeposited sediments from shallower depositional settings with lower salinity levels within the surface water.

The confinement of thicker sedimentary units to segmented basins on synclinal areas indicates that the Pakhna Fm. was deposited during an apparent compressional stress event entailing uplift of the trench slope as proposed by Takano et al. (2013) for forearc Basins offshore Japan. Consequently, trench slope break uplift and landward suppression could produce these features in slope or forearc settings. Compressional tectonics cause a shallowing of slope basins with simultaneous seaward migration of the trench, leading to uplift of the internal zone and shallowing upward sedimentary sequences in the slope basin. Slope basins can be categorized as "overfilled deep-marine terraced" types (Dickinson, 1995) given that the estimated trench slope break becomes mostly submerged and exhibits deep-marine sedimentation. Basin segmentation into 50 to 100 km long sub-basins during the late Oligocene to Miocene reflects enhanced oblique subduction processes and strike-slip movement (Takano et al., 2013).

7.1.4. The marly unit in the upper Pakhna Fm

Above the sandy contourite package III within the Pakhna Fm. (Figs. 3B, 4 and 10A), a middle to late Miocene marl formed regionally during the Serravallian to early Tortonian stages (late Miocene, ~ 12.77 to 10 Ma). This unit serves as another stratigraphic guide for the end of contourite deposition in onshore sections at the Cyprus locality. The Serravallian to Tortonian white marls appear until the restriction (~ 8 Ma) and final closure of the Atlantic connection, when late Miocene blue marls appear (de Weger et al., 2021).

7.2. Contouritic depositional systems: sedimentary model and the stratigraphic position of the sandier contourites deposits

Facies associations FA6 and FA7 represent the partial record of contourite depositional features (drifts) visible in outcrops at the sedimentary facies scale. Robertson (1977) initially described evidence of contourite deposits and their occurrence onshore Cyprus as the accumulation of a thick sequence of Paleocene and Eocene calciturbidites, and possible contourites along the southern margin of the Troodos Massif. Later, other authors studied the contourite deposits (Kähler, 1994; Kähler and Stow, 1998; Stow et al., 2002b) and proposed a sedimentary model for the uppermost chalk and marl units of the Lefkara Fm.

The contourites identified in this work were deposited within the upper plate of an active continental margin (Fig. 20). Previously and coevally deposited and modified pelagic and turbidite deposits served as the sedimentary source. From Eocene to middle Miocene times, weak bottom currents were vigorous enough to influence vertical settling and low-density turbiditic processes (coeval winnowing), and/or to remobilise previous pelagic and turbidite deposits (post-depositional winnowing and reworking). Shallow marine carbonate particles identified within contourites have the same composition as those of the turbidite beds. The Troodos ophiolite complex, which had already experienced uplift and alteration during the Oligocene-Miocene, would be the probable source area for fine-grained siliciclastic materials (Eaton and Robertson, 1993). Gravity flows carried the shallow marine bioclasts to the slope setting, after which bottom currents redistributed the sediment. Occurrence of clastic particles (illite and silt-sized quartz) within the greenish calcarenites with internal wavy layering points to bottom-current controlled sediment entrainment from siliciclastic sources (Hüneke et al., 2021).

Coeval contourite features have also been determined in offshore areas around Cyprus along the slope and in deeper basins (Fig. S1 and S2 in supplementary material), thereby evidencing an active intermediate and deep water circulation regionally throughout the eastern Mediterranean Sea. The records of contourite deposits from active margins remain scarce in comparison to records from passive margins. Furthermore, active margin contourite deposits reported from modern marine settings appear more limited than those developed along modern passive margins (Reed et al., 1987; Bailey et al., 2021) or in the ancient sedimentary record (Schiller et al., 1994; Stow et al., 2002c). Bottom current features have been identified along trenches and adjacent abyssal plains, accretionary prisms and within slope basins, including forearc basins (Underwood and Moore, 1995; Bailey et al., 2021). In the upper slope, drift associations are common. Plastered drifts and sedimentary waves, for example, conform extensive intra-basinal structures that serve as corridors for enhanced bottom currents (Saffer et al., 2018; Bailey et al., 2021).

Facies associations FA6 and FA7 represent depositional elements of ancient contourite depositional systems (CDS), even though major erosional features (channels, moats, furrows) did not appear in the sections analysed here. The associations could represent two CDSs (Figs. 20 and 21). Eocene bottom currents flowing predominantly NW formed finer-grained contourites (FA6) along the lower slope. They were later buried by Oligocene marls (Fig. 20). Late Oligocene to middle Miocene circulation to the SE then formed coarser-grained contourites (FA7) in shallower (middle to upper slope) environments. They, in turn, became buried by Serravallian marls (Fig. 20). During that time, bottom

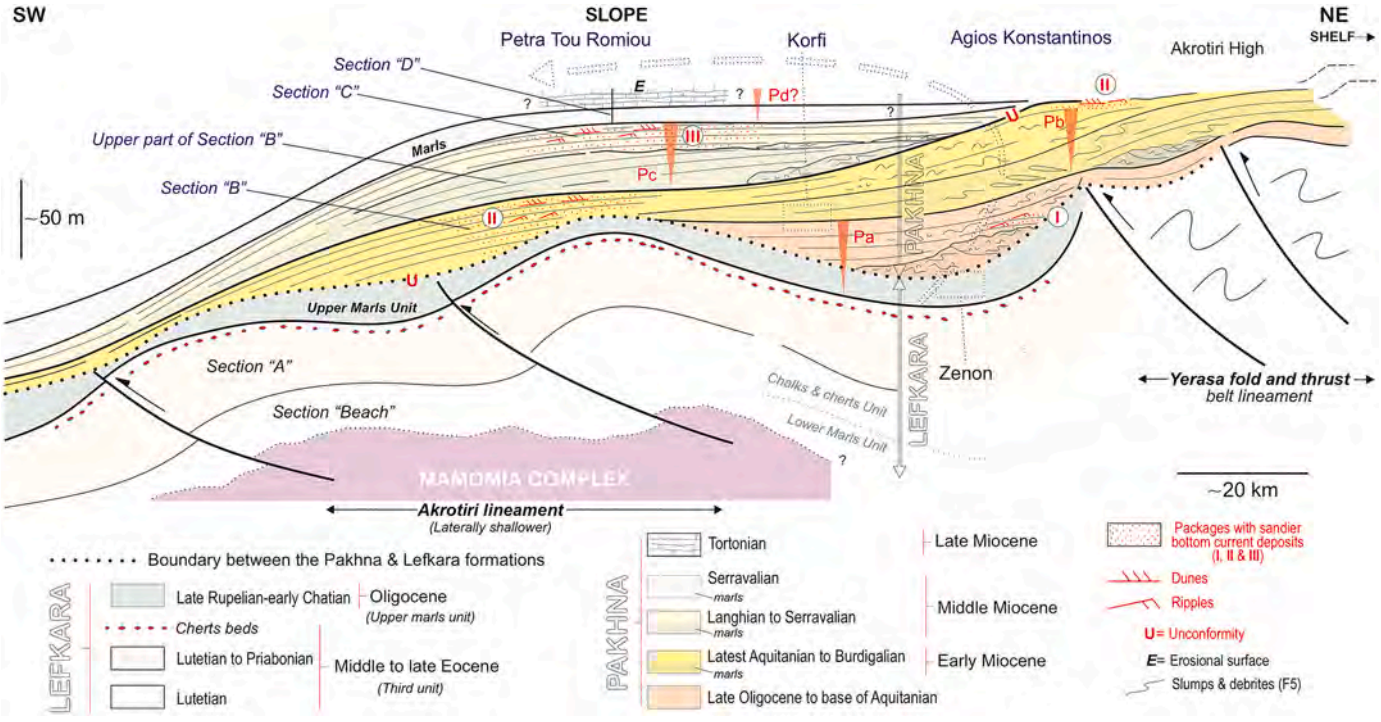

Fig. 20. Theoretical sedimentary model explaining formation of contourites along a basin slope of the upper plate in Cyprus. The model highlights stratigraphic position of sandy contourite packages I, II and III and the four packages of strata (P) within the latest Oligocene to middle Miocene deposits (inverted red triangles): Pa) late Oligocene – base of Aquitanian; Pb) Aquitanian / Burdigalian; Pc) Burdigalian to Langhian and Pd) Serravallian to Tortonian. Horizontal and vertical scale are relative. Syn-sedimentary tectonic features were also active during the latest Oligocene to middle Miocene.

current flow directions and velocities varied locally owing to the complex local sub-basin morphology —for example, in the Korfi and Kalavasos locations. The Petra Tou Romiou section deposits host contourites that are coarser and sandier than the predominantly muddy contourites of the Agios Konstantinos and Korfi sections, located landward and to the east (Fig. 20), which show a greater influence of the supply from turbidity currents or MTDs from slope failure (Fig. 20). The part of the basin hosting the Petra Tou Romiou section thus underwent more effective winnowing and reworking processes. Facies association FA7 includes asymmetric bi-gradational sequences and sandy dunes on flatter (terrace) domains along slope (e.g., Viana and Faugères, 1998; Thieblemont et al., 2019; Miramontes et al., 2019; Miramontes et al., 2021; Miramontes et al., 2020; de Castro et al., 2021b). Terraced slopes also frequently appear along active margins (Dickinson, 1995) and can be identified in offshore areas around Cyprus associated to plastered drifts along the slope (Tartus Basin) (Fig. S1 and S2 in supplementary material). Water masses and their secondary oceanographic processes are known to influence flatter domains by extensive development of sandier bottom current deposits, including ripples and small dunes, as documented in both modern and ancient marine records (Mutti et al., 2014; Shanmugam, 2014; Hernández-Molina et al., 2017a; Miramontes et al., 2019, 2020, 2021; de Castro et al., 2021b) and even Mesozoic outcrops (Bádenas et al., 2012; Val et al., 2018).

Based on our observations and as described above, a regional shift in water mass circulation occurred coeval to the transition from the Lefkara to the Pakhna Fms., and two possible explanations could be considered: a) a current reversal among water masses, or b) the influence of different water masses over time. Accordingly, the lower slope was influenced by deeper water masses during Lefkara Fm. deposition, or else the upper and middle slope were influenced by intermediate water masses flowing in an opposite direction during Pakhna Fm. deposition. The long-term shallowing trend of the margin lends support to the second explanation, but a flow reversal might be traced to a combination of the two. Such a shift in water mass circulation agrees with the proposed flow reversal between the Oligocene and Miocene through the Panama Seaway (Fig. 21) or Cental American Seaway (Omta and Dijkstra, 2003; von der Heydt and Dijkstra, 2005, 2006). This flow reversal is attributed to the narrowing of the Tethys Seaway in the early Miocene (Figs. 21 and 22) and the widening of the Southern Ocean passages (von der Heydt and Dijkstra, 2006).

Long-term sedimentary variations are detected from the Eocene to the middle Miocene. The Eocene CDS (Lefkara Fm.) terminates by the en of the Eocene (~33.9 Ma) and becomes buried by marl deposits from late Rupelian to Chattian times (~29.5 to 23 Ma). Deposits occurring stratigraphically below are chalks with extensive chert (early to middle Eocene, ~56-41 Ma) and the lower marls (end of the Paleocene / beginning of the Eocene) (Robertson, 1976, 1977; Kähler, 1994; Kähler and Stow, 1998; Stow et al., 2002b). The latest Oligocene to middle Miocene CDS (Pakhna Fm.) spans from late Oligocene to Langhian (~ 13 Ma) / early Serravallian (~ 13 Ma) being stratigraphically above the Oligocene marls and buried by Serravallian marls (~ 13 to 11.54 Ma). Therefore, the architecture from latest Cretaceous to early Miocene consists of two long-term sedimentary variations (Figs. 20, 21 and 23) having a duration of a few tens of millions of years (~ 20-25 My), where each CDS would develop in the upper part of each variation with about ten millions of year (Figs. 21 and 23). At smaller scales, the latest Oligocene-mid Miocene CDS contains the following packages of strata (P) (inverted red triangles in Figs. 4, 11, 16, 20, 21 and 23): Pa) late Oligocene – Base of Aquitanian, Pb) Aquitanian to Burdigalian, Pc) Burdigalian to Langhian, and Pd) Serravallian to Tortonian. Each package of strata represents a cycle of beds showing a progradational pattern, with dominant marl deposits in the lower part evolving into dominant calcarenite deposits in the upper part (Fig. 23). These end with the sandier contourite packages I (Pa), II (Pb) and II (Pc), respectively of Chattian (late Oligocene), latest Aquitanian-Burdigalian (early Miocene) and Langhian (middle Miocene) ages. Shallowing-upward cycles document the creation of limited accommodation space soon filled by sediments, sharing common characteristics with parasequences (Catuneanu, 2022). Although biostratigraphy provides reasonable regional age control for the studied outcrops, the dating does not provide a high-resolution age model for these packages of strata. In spite of this limitation, their duration appears to span a few (4-5) million years. The base, and over the top, of the calcarenite upper parts frequently hosts MTDs and/or turbidites representing key periods of sedimentary instability spanning about 2-2.5 My in duration (Fig. 23). Shorter-term, thickening upward sequences (Figs. 21 and 23) also appear within these sequences (yellow inverted triangles in Figs. 5A, 7G, 10A and 12B).

7.3. Bi-gradational sequences: permanent or intermittent bottom currents?

Cyprus represents an ancient sedimentary example of bi-gradational sequences (Fig. 19) with bedforms recording higher velocity bottom currents in the middle or upper part of packages I, II and III (Fig. 20). The bi-gradational contourite model defined from the middle slope of the Gulf of Cadiz by Faugères et al. (1984) and Gonthier et al. (1984) lacks, however, sedimentary structures due to intense bioturbation (Rodríguez-Tovar and Hernández-Molina, 2018). In Cyprus, contourites clearly record sedimentary structures (horizontal laminations, ripples, small dunes, etc.) in the middle or upper divisions of sequences despite bioturbation and diagenetic alteration. Early diagenesis may have led to rapid lithification that preserved original sedimentary structures for units having high percentages (>90%) of carbonate bioclasts. Polar margins are another setting where primary sedimentary structures are well preserved, but in this case because environmental conditions do not favour benthic activity (Rodrigues et al., 2022a).

The occurrence of bi-gradational contourite sequences in association with other pelagic or turbidite deposits indicates intermittent bottom currents affecting sections at meter scales. A thick sandy calcarenite bed signals a vigorous bottom current whose flow strength fluctuated irregularly. In modern contourite drifts with mixed siliciclastic-bioclastic composition, full bi-gradational sequences point to cyclic variation in the forcing variables, with periodicities ranging from 3,000 to 10,000 years (Brackenridge et al., 2018). These include millennial scale precessional (orbital) and climatic variables (Sierro et al., 2020; de Castro et al., 2021a; de Weger et al., 2021). Banding patterns in contourite deposits within bi-gradational sequences represent relatively shorter-term fluctuations in flow strength of bottom currents, inducing regular changes in depositional processes during the accumulation of calcarenite beds. Phases of flow acceleration caused the recurrence of bed-load traction, with ripples and dune formation; and phases of flow deceleration caused deposition of suspended sediment, which effectively suppressed traction and induced draped lamination and grading. Controlling mechanisms for short-term fluctuations in flow strength remain unknown, although centennial fluctuations (Martorelli et al., 2021) and deep tides (Shanmugam, 2006, 2014; Rebesco et al., 2014; de Weger et al., 2021) have been suggested. In summary, the Cyprus contourites record bottom currents that were neither permanent nor semi-permanent. Bottom current circulation and associated paleo-environmental conditions were instead intermittent at different scales, and they could interact in a synchronised or unsynchronised manner with other sedimentary processes, e.g., pelagic sedimentation or turbidite flows.

7.4. Evolutionary stages

The closure of the Tethys Ocean due to convergence and northward-dipping subduction of the African beneath the Eurasian plate affected the study area (Fig. 22). This event induced the formation and subsequent obduction of the Troodos ophiolites during the Late Cretaceous, its collision with the Mamonia Complex in the late Maastrichtian, and the later establishment of a deep-marine setting with active deposition

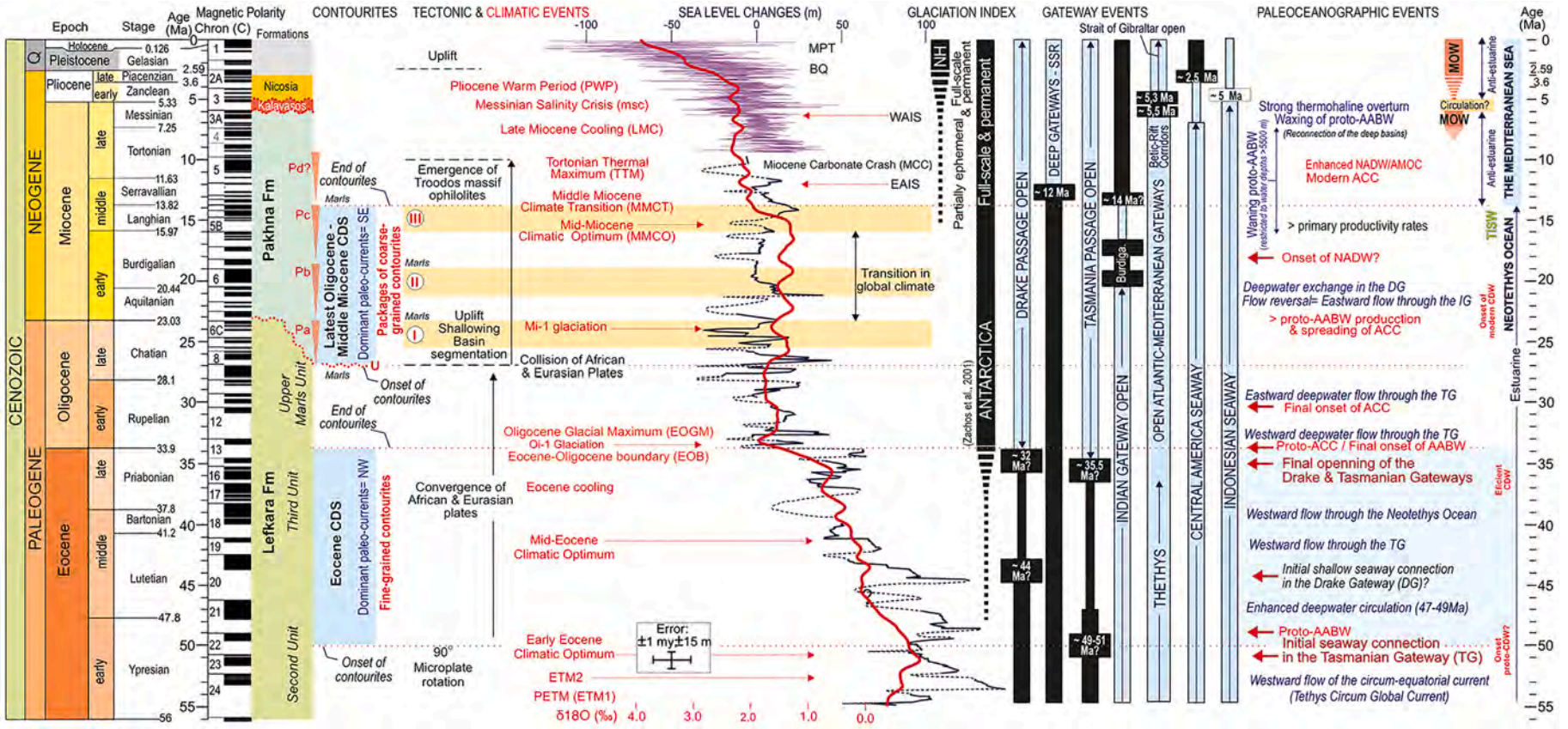

Fig. 21. Sketch of major Paleogene to Quaternary global changes, including climatic, sea level, palaeoceanographic and tectonic events. These events are correlated with regional stratigraphy around Cyprus, the evolutionary stages for the studied deposits, the highlighted position of sandy contourite packages I, II and III, and the four packages of strata (P) within the latest Oligocene to middle Miocene deposits (inverted red triangles). Global sea level records: 1) global sea level (in pink) from 0 to 7 Ma (Miller et al., 2020); 2) global sea level (dark blue dot line) from 7 to 56 Ma (Miller et al., 2020); 3) global sea level (dark blue continuous line) from 7 to 65 Ma (Kominz et al., 2008), based on deep sea oxygen isotope records; 4) oxygen isotopic (in red) synthesis (Zachos et al., 2008; Cramer et al., 2011). The long-term major climatic changes and cooling trend were punctuated by several global-scale climatic events and transitions including the Miocene Climatic Optimum (MCO), Middle Miocene Climate Transition (MMCT), Tortonian Thermal Maximum (TTM), Late Miocene Cooling (LMC), and Pliocene Warm Period (PWP) (Eocene to late Miocene major climatic and palaeoceanographic changes and events synthesized from (by alphabetic order: Allen and Armstrong, 2008; Allen and Armstrong, 2008; Bahr et al., 2022; Barker et al., 2002, 2007; Barron and Keller, 1982; Berra and Angiolini, 2014; Bianchi et al., 2012; Bijl et al., 2018; Billups and Schrag, 2002; Billups, 2002; Boyle et al., 2017; Bryden and Kinder, 1991; Cande and Stock, 2004; Capella et al., 2017, 2019; CIESM, 2008; Cramer et al., 2011; Cramwinckel et al., 2018; de la Vara and Meijer, 2016; de Weger et al., 2020, 2021; Douglas et al., 2014; Eagles and Jokat, 2014; Evangelinos et al., 2020; Exon et al., 2001, 2004; Flecker et al., 2015; Flower and Kennett, 1993; Galeotti et al., 2016; Hamon et al., 2013; Harzhauser et al., 2007; Hay, 2009; Herbert et al., 2016; Hernández-Molina et al., 2010, 2014, Hernández-Molina et al., 2017b; Herold et al., 2008, 2012; Hodel et al., 2021; Hodell and Venz-Curtis, 2006; Holbourn et al., 2015; Houben et al., 2019; Hsü et al., 1973; Hüsing et al., 2009; Ivanovic et al., 2013; Karami et al., 2011; Kennett and Barker, 1990; Krijgsman et al., 1999; Lagabrielle et al., 2009; Lawver and Gahagan, 2003; Lear et al., 2015; Leutert et al., 2020; Levy et al., 2022, Liebrand et al., 2017; Magyar et al., 1999; Maldonado et al., 2003, 2006, 2014; Martos et al., 2013; McKay et al., 2022; Meulenkamp and Sissingh, 2003; Modestou et al., 2020; Naish et al., 2001; Newkirk and Martin, 2009; Ng et al., 2021, 2022; Nisancioglu et al., 2003; Pekar and DeConto, 2006; Pérez et al., 2019, 2021; Pérez-Díaz and Eagles, 2017; Pfuhl and McCave, 2005; Popov et al., 2004; Reid, 1979; Renema et al., 2008; Reuter et al., 2009; Rodrigues et al., 2021, 2022c; Rogerson et al., 2012; Rögl, 1998, 1999; Rosenbaum et al., 2002; Roveri et al., 2014; Salabarnada et al., 2018; Sangiorgi et al., 2018; Scher and Martin, 2006; Scher et al., 2015; Scotese and Wright, 2018; Shevenell et al., 2004, Shevenell et al., 2008; Sijp et al., 2011; Stampli and Borel, 2002; Steininger and Wessely, 2000; Stickley et al., 2004; Straume et al., 2020; Super et al., 2018, 2020; Sykes et al., 1998; Thieblemont et al., 2019, Thiéblemont et al., 2020; Torfstein and Steinberg, 2020; Uenzelmann-Neben et al., 2017; Utescher et al., 2011; van de Lagemaat et al., 2021; Westerhold et al., 2020; You, 2010; Zachos et al., 2001, 2008; and Zhang et al., 2013). Abbreviations in alphabetic order: ACC= Antarctic Circumpolar Current; AABW= Antarctic Bottom Water; BGMS= Base of the Glacial Margin Sequences; BQ= Base of the Quaternary (2.6 Ma); CDW= Circumpolar Deep Water; EAIS= Eastern Antarctic Ice Sheet; LCDW= Lower Circumpolar Deep Water; MTDs= mass transport deposits; NADW= North Atlantic Deep Water; NH= Northern Hemisphere; UCDW= Upper Circumpolar Deep Water; UU= Uplift Unconformity.

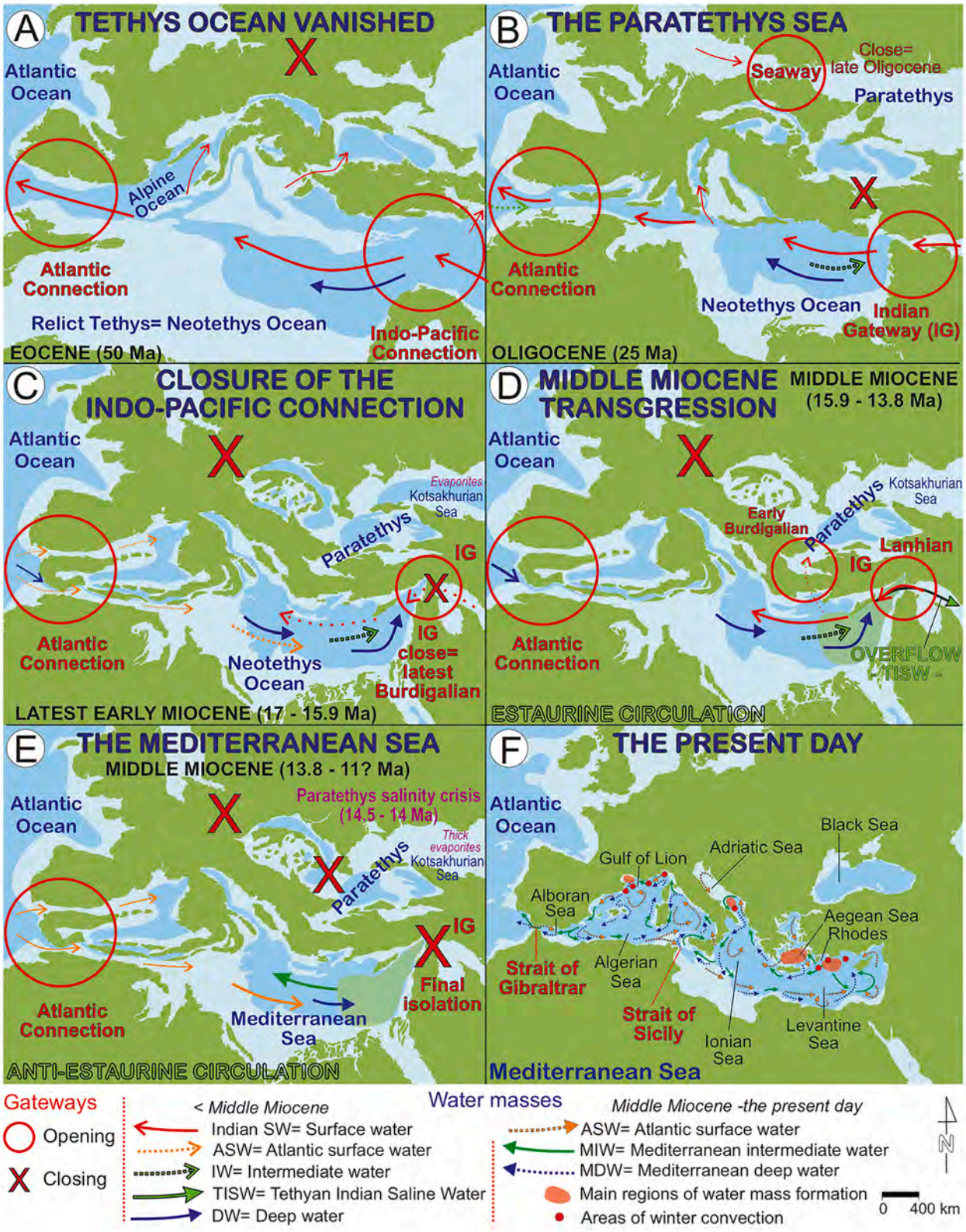

Fig. 22. Paleo-reconstructions of Eocene (A), Oligocene (B), latest early Miocene (C), middle Miocene (D and E) and present day (F) for the Neotethys Ocean and Mediterranean Sea, including regional distribution of surface, intermediate and deepwater masses, and the key opening and closure of gateways, especially for the Indian and Atlantic Gateways (compilation based on Kähler and Stow, 1998; Rögl, 1998, 1999; Magyar et al., 1999; Millot, 1999, 2009; Steininger and Wessely, 2000; Stow et al., 2002b; Popov et al., 2004, 2006; Hüsing et al., 2009; Karami et al., 2009; Herold et al., 2012; Hamon et al., 2013; de la Vara and Meijer, 2016). Eocene finer-grained contourites developed in A, but the coarser (sandy) contourites packages were developed in B (package I, Chattian, late Oligocene); C (package II, Aquitanian/Burdigalian, early Miocene); and D (Package III, Langhian, middle Miocene). Base maps after paleogeographic maps of Europe by Balaky and Tamar-Agha, 2017 (Deep Time Maps™, https://deeptimemaps.com).

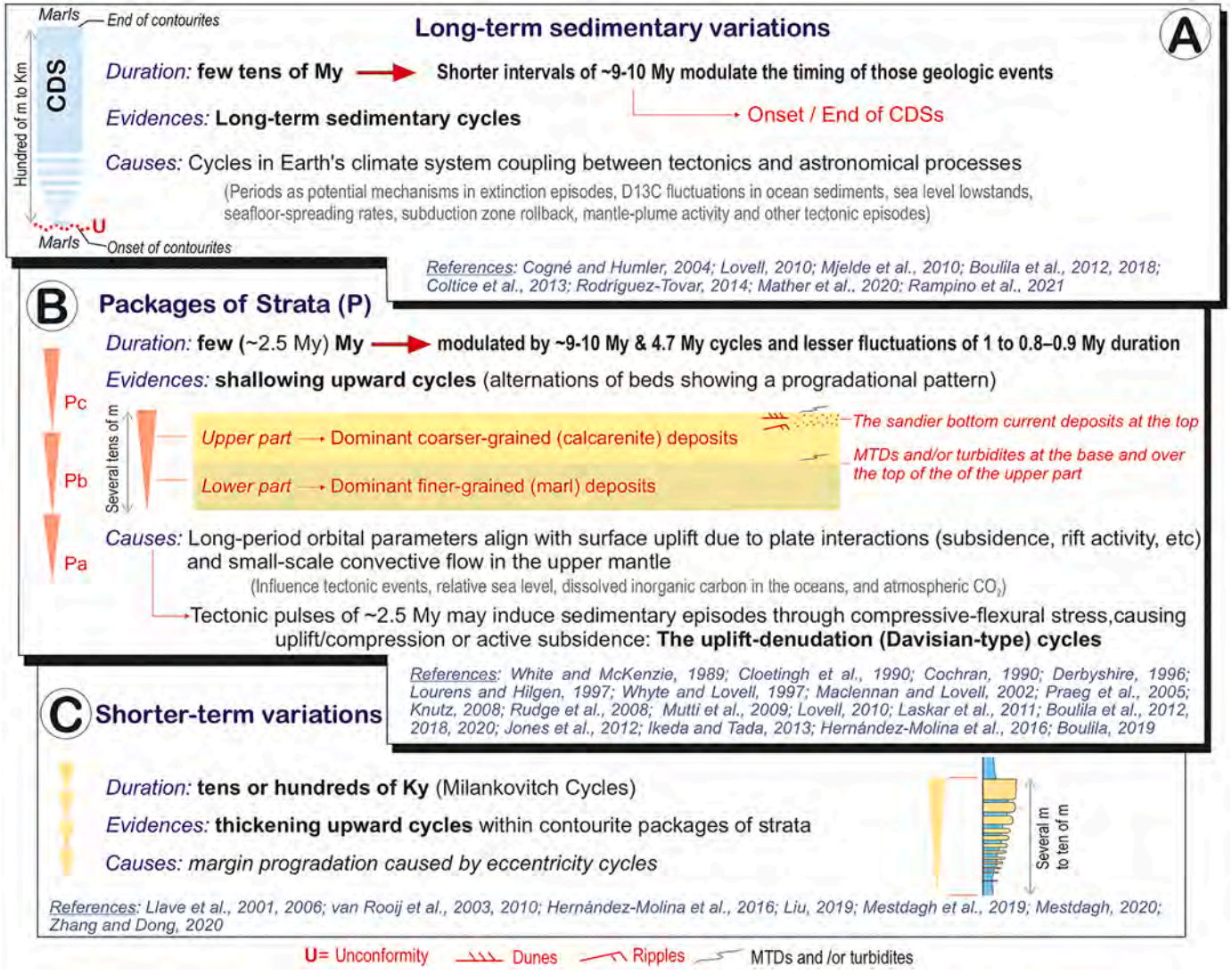

Fig. 23. Long-term sedimentary variations, the packages of strata (P) with shallowing-upward trend and the shorter-term thickening upward sequences identified in the studied sedimentary record at Cyprus, which determine a clear repetition in the sedimentary stacking pattern at different scales, where the onset and buried of Contourites Depositional Systems (CDS) and the stratigraphic position of the sandier contourites deposits is not random (*key references are included for further details about the causes and implications on these variations are included for each case*). The two long-term sedimentary variations, could be related to second-order of 26- to 36-My cycles in Earth's climate system coupling tectonic processes and episodic astronomical periods, which are typically modulated by shorter intervals of ~9-10 My duration. Shorter cycles of about ~2.4/2.5 My correspond to long-period orbital parameters align with surface uplift due to plate interactions (subsidence, rift activity, etc.) and small-scale convective flow in the upper mantle, modulated by ~9 to 10 My and 4.7 My astronomical cycles and lesser fluctuations of 1 to 0.8–0.9 My duration. Tectonic pulses of ~2.5 My induce sedimentary episodes through compressive-flexural stress, causing uplift/compression or active subsidence, and may also be tied to uplift-denudation (Davisian-type) cycles of tectonic origin (*sensu* Mutti et al., 2009). These variations would generate shallowing-upward cycles in which calcarenite deposits in upper strata coincide with compression, margin progradation and relative sea level fall caused by tectonic events, and enhanced bottom currents that deposited sandier contourite packages. Deposition of sandy contourites may reflect compression and inversion caused by subduction, as proposed by Schiller et al. (1994). Shorter-term thickening-upward sequences within contourite packages have been described previously in other deepwater setings, and they may reflect margin progradation caused by eccentricity cycles, as proposed for other continental slopes dominated by contourite deposition. (Boulila et al., 2012; Boulila et al., 2018; Boulila et al., 2020; Cloetingh et al., 1990; Cochran, 1990; Cogné and Humler, 2004; Coltice et al., 2013; Derbyshire, 1996; Hernández-Molina et al., 2016; Ikeda and Tada, 2013; Jones et al., 2012; Laskar et al., 2011; Liu, 2019; Llave et al., 2001; Lourens and Hilgen, 1997; Lovell, 2010; Maclennan and Lovell, 2002; Mather et al., 2020; Mestdagh, 2020; Mestdagh et al., 2019; Mjelde et al., 2010; Montadert et al., 2010; Praeg et al., 2005; Rampino et al., 2021; Rodríguez-Tovar, 2014; Rudge et al., 2008; Van Rooij et al., 2003; Van Rooij et al., 2010; White and McKenzie, 1989; Whyte and Lovell, 1997; Zhang and Dong, 2020)

(Robertson and Xenophontos, 1993; Stampfli and Borel, 2002; Lapierre et al., 2007; Kinnaird, 2008; Robertson et al., 2012). The Eocene to late Miocene sedimentary succession in Cyprus appears to record four main evolutionary stages (a-d) related to the (plate tectonic) evolution of the Indian Gateway (IG) and the exchange between the Indian and the Neotethys oceans (Figs. 21 and 22), the latter of which preceded the Mediterranean Sea. The Indian Gateway influenced paleo-circulation and water mass stratification in the adjacent marine basins (de la Vara and Meijer, 2016) and triggered a series of global environmental changes (Zachos et al., 2001; Hamon et al., 2013) (Figs. 21 and 22).

7.4.1. Eocene to late Oligocene stage: Upper Lefkara Fm. and closure of the Tethys Ocean

Results from the Cyprus sections indicate that, from the Lutetian (~45 Ma, Eocene) to end of the Eocene (~33.9 Ma), the southern continental margin of the Troodos massif (Cyprus) experienced pelagic sedimentation simultaneously with fine grained contourite and turbidite deposition. The upper Lefkara Fm. records these processes. During that

time, basin deposition consisted of distal and relatively deepwater (lower slope) deposition by water masses flowing northwest (Fig. 22A). Along-slope circulation would have generated an initial contourite depositional system (CDS) with possible sheeted drifts made up mainly of muddy contourites formed by a reworking of pelagic and fine grained turbiditic deposits. Thus, homogenous material was deposited over previous seafloor irregularities and older Cretaceous deposits (Robertson, 1976; Peybernes et al., 2005). Robertson (1977) proposed gradual relative shallowing of the basin in a laterally continuous and northeastward direction during the late Eocene. Shallower marine domains became established, with sediment transport through low-density NE to SW turbidite flows (Robertson, 1976). During the Oligocene, a change in depositional style occurred with a rise in sea level. Widespread deposition of marls buried and preserved the Eocene CDS. Similar marl deposits appear regionally on continental slopes around the Mediterranean (e.g., Rögl, 1998, 1999; Hawie et al., 2013). By the beginning of the Oligocene, new climate conditions induced a shift from more siliceous to calcareous organisms, entailing extinction of the former (radiolaria) and preservation of the latter by a deeper CCD (Molina et al., 1993).

During the Eocene, the tectonic setting became regionally compressional, but remained relatively quiescent due to low velocity subduction (Eaton and Robertson, 1993; Calon et al., 2005; Robertson et al., 2012). Slope basin formation during subduction processes explains local normal faults as well as evidence of occasional synsedimentary instability in the form of MTDs, including slumps and debrites (Fig. 21). Symeou et al. (2018) described coeval normal faults offshore Cyprus. The relative quiescent tectonic setting occurred after a complex period during which the Troodos plate was rotated and strongly deformed in late Cretaceous and into early Eocene time (Clube and Robertson, 1986). By the late Eocene, maximum stress fields changed from NW-SE to N-S coeval with the separation of the African and Arabian plates, the Dead Sea Transform Fault began its displacement, and collision between the Kyrenia Range and Troodos ophiolites began (Robertson and Woodcock, 1986; Papadimitrioua et al., 2018).

At this stage, the Neotethys Ocean was connected to and exchanged water with both the Atlantic and Indian oceans (Rögl, 1998; Rögl, 1999; Meulenkamp and Sissingh, 2003; Reuter et al., 2009). Water mass exchange was dominated by westward and northwestward flow of the circum-equatorial current (Fig. 22A) or the so-called Tethys Circum Global Current (Butzin et al., 2011; Krapp and Jungclaus, 2011; Herold et al., 2012). This flow prevailed until the late Oligocene (Rögl, 1999; Hay, 2009). Within this paleoceanographic framework, the middle to late Eocene onset of contourites in the Eocene represents bottom currents enhanced by a new and persistent deepwater current circulation accompanied by a shallowing-upward trend. These long-term changes occurred coevally with a decline in the global mean temperature from 29°C to 19°C from the early to the late Eocene (Cramwinckel et al., 2018). Similar changes in Eocene paleo-circulation have been reported from other marine basins such as the North Atlantic, where the onset of enhanced deepwater circulation from ~49 to 47 Ma formed contourite drifts below ~4000 m water depths (Boyle et al., 2017; Bahr et al., 2022). Some researchers interpret this shift in paleoceanographic circulation as having occurred due to the separation of Antarctica from Australia (~50 Ma ago) and the formation of the Antarctic water masses (e.g., the proto-Antarctic Bottom Water) (Boyle et al., 2017; Pérez-Díaz and Eagles, 2017; Rodrigues et al., 2022c). The important change in the depositional style with the burial of the Eocene CDS by the end of the Eocene (Fig. 21) is coeval with an important shift in global climatic conditions from an ice-free greenhouse state to a state of persistent ice coverage (Galeotti et al., 2016; Westerhold et al., 2020). The very weak circulation of the Tethys Circum Global Current (and the equatorial seaway) during the Oligocene is coincident with the development of the circum-Antarctic circulation system (the proto-Antarctic Circumpolar Current, proto-ACC) and the final onset of the AABW (Fig. 21) after the opening of the Drake Passage / Scotia Sea and the Tasmanian Gateway (Kennett, 1982; Scher and Martin, 2006; Sijp et al., 2011; Douglas et al., 2014; Galeotti et al., 2016; Houben et al., 2019; Straume et al., 2020; Bahr et al., 2022).

7.4.2. Late Oligocene to early Miocene: Pakhna Fm. and Indian Gateway restrictions

A second stage began in the latest Oligocene / Aquitanian and lasted into the late Burdigalian (early Miocene 17 – 15.9 Ma). Results described here indicate a shift in sedimentary style and tectonic setting. The changes led to the development of turbidites, MTDs, and coarser-grained contourites in a background of pelagic/hemipelagic sedimentation. These diachronous events are recorded in the lower Pakhna Fm.

The erosive, latest Oligocene to early Miocene basal boundary and periodic occurrence of MTDs indicate successive compressional pulses and general sedimentary instability in the wake of the latest Oligocene / early Miocene. A similar hiatus has been identified offshore in the eastern Mediterranean, coeval with a shift in the maximum regional tectonic stress field from NW-SE to N-S (Hawie et al., 2013; Papadimitrioua et al., 2018). This shift reflects: a) the onset of the collision between the African and Eurasian plates in the late Oligocene, b) the separation of the African and Arabian plates, plus the initiation of the Dead Sea Transform Zone, c) northward-dipping active subduction along the Cyprus Arc System, and d) regional uplift and deformation of the Troodos Massif (Dercourt et al., 1986; Robertson and Woodcock, 1986; Rögl, 1998; Rögl, 1999; Robertson, 1990; Eaton and Robertson, 1993; Brew et al., 2001; Edwards et al., 2010; Nader, 2011; Papadimitrioua et al., 2018; Symeou et al., 2018).

Local expressions of these tectonic events along the southern continental margin of the Troodos Massif are referred to as the Politiko tectonic events. They restructured southerly areas of the massif and previous margin and induced erosion of both the WNW-ESE Yerasa fold and thrust belt lineament (Morel, 1960) and the Akrotiri high (Robertson, 1976). Restructuring of the margin caused segmentation of the slope into a number of local highs and sub-basins (Fig. 21). In turn, they determined locations for Miocene sedimentary depocenters within the new compressional regime. The Yerasa lineament thereafter separated the Maroni sub-basin in the east from the Khalassa sub-basin in the west. The Petra Tou Romiou, Agios Konstantinos, and Korfi sections were confined to the Maroni sub-basin, while the Kalavasos section became part of the adjacent eastward Khalassa sub-basin (Eaton and Robertson, 1993). The E-W trending Akrotiri high bounded the new sub-basins to the south (McCaltum, 1989). At local scales, isolated highs, shelves, and coral reefs (Terra Member) formed due to these events (Follows, 1992).

At this time, the southern continental margin of the Troodos Massif had begun prograding basinward, developing an increasing slope gradient (Robertson et al., 1991). This coincided with a general shallowing upward of sedimentary trends and a global sea level fall. Sandy contourite packages I and II (Fig. 21) formed during this time owing to bottom currents —occasionally enhanced— flowing SE, and higher sediment supply.

At the beginning of this stage, the Neotethys Ocean remained connected (Fig. 22B and C) to both the Atlantic and Indian oceans (Rögl, 1998, 1999; Meulenkamp and Sissingh, 2003; Reuter et al., 2009). By the latest Oligocene, a new circulation regime became established (Fig. 22B) through the Indian Gateway (Allen and Armstrong, 2008; Herold et al., 2008, 2012; Hamon et al., 2013; Bahr et al., 2022). It included: a) a superficial (0-500 m wd) water mass flowing north to westward from the Indian Ocean into the Neotethys, b) an intermediate (500-2500 m wd) water mass referred to as the Tethyan Indian Saline water (TISW) circulating southeastward as warm and salty water flowing from the Neotethys toward the Indian Ocean, and c) a deepwater mass (>2500 m wd). In contrast to present dynamics (Figs. 22 and Fig. S3), surface water from the Neotethys flowed toward the Atlantic, whereas deeper water flowed eastward from the Atlantic towards the Neotethys (Rögl, 1998, 1999; Hamon et al., 2013; de la Vara and Meijer, 2016). The early Miocene is marked by a major transition in global climate, from the relatively warm conditions of the late Oligocene to

generally cooler climates (Fig. 21) that persisted through most of the Neogene (Zachos et al., 2001; Cramer et al., 2011; Zhang et al., 2013; Super et al., 2018; Miller et al., 2020; Super et al., 2020; Naish et al., 2001). During the early Miocene, the Indian Gateway became shallower due to the collision of the Arabian and Eurasian plates. This triggered intensification of water mass exchange and gave rise to severe changes in the water mass properties of the Neotethys (de la Vara and Meijer, 2016). An open connection through the Indian Gateway became very shallow and even closed (Fig. 22C and Fig. S3) during a short period in the late Burdigalian, reopening later during the Langhian (middle Miocene, Fig. 22D) (Rögl, 1998).

7.4.3. The middle Miocene: transgression, reconnection and deepening

After the previous stage, the marly/muddy interval described within the Pakhna Fm. between contouritic packages II and III formed during the early Langhian (middle Miocene, 15.9 – 13.8 Ma). Another pulse of margin progradation, sedimentation and development of turbidites, MTDs and coarser-grained contourites (package III) occurred against a background of pelagic/hemipelagic sedimentation (Fig. 20).This new period of sedimentary instability coincides with gradual shallowing and emergence of the Troodos Massif (Robertson, 1977). The deposition of package III represents another period of enhanced bottom currents flowing predominantly towards the SE, with water column stratification and in a water mass circulation configuration similar to those prevailing in the early Miocene.

This evolutionary stage followed the relatively cool climate of the earliest Miocene (Fig. 21). The global climate then entered one of the warmest intervals (Miocene Climatic Optimum, 17 to 14.8 Ma) of the past 35 million years (Flower and Kennett, 1993; Utescher et al., 2011) coeval with a global transgression trend (Zachos et al., 2001; You, 2010). It ended at ~14.8 Ma with the onset of cooling and glacial expansion through the middle Miocene (Super et al., 2018; Leutert et al., 2020). Ocean circulation also changed during this time (Shevenell et al., 2008) because of: a) constriction of the Tethys ocean (Hamon et al., 2013); b) final modern ACC formation (~ 11 Ma), and c) vigorous, widespread deepwater currents associated with Southern Component Water (Maldonado et al., 2003; Bijl et al., 2018; Salabarnada et al., 2018; Sangiorgi et al., 2018; Pérez et al., 2019, 2021; Evangelinos et al., 2020). Contourite formation occurred during this stage as a consequence of the re-establishment of circulation in the wake of the reconnection of the Neotethys with the Indian Ocean through the Indian Gateway (Fig. 22D) from the Langhian to the beginning of the Serravallian (Rögl, 1998, 1999; Magyar et al., 1999; Steininger and Wessely, 2000; Meulenkamp and Sissingh, 2003; Popov et al., 2004; Reuter et al., 2009). The relative movement among Eurasian, African and Arabic plates made oceanic reconnection possible (Rosenbaum et al., 2002; Stampli and Borel, 2002; Hay, 2009; Berra and Angiolini, 2014). The identified intervals containing calcareous dinoflagellates from shallower, less salinity depositional settings suggest a transition to a new surface circulation model, wherein surface water from the Atlantic flowed toward the Neotethys coeval with Indian Gateway closure.

7.4.4. Middle to late Miocene: Indian Gateway closure and the inception of the Mediterranean Sea

This stage occurred during the early Serravallian and earlier Tortonian (middle Miocene, around 13.8-11 Ma). Results reveal a remarkable shift in sedimentary style during the Serravallian, with additional marl deposition that buried the late Oligocene to middle Miocene CDS observed in the onshore Cyprus section (Fig. 21). A visible shift in lithologies and colour to yellowish marls / reddish calcilutites, with light grey calcilutites and occasional calcarenites, marks the beginning of this stage. Eaton and Robertson (1993) described similar lithological changes in other localities around Cyprus. Deposition occurred during a marine transgression and significant subsidence; it ended with progressive shallowing in the late Tortonian to Messinian. Local coral reef (Koronia Member) development took place around highs and tectonic blocks influenced by local structures (Follows, 1992; Eaton and Robertson, 1993).

A change in sedimentary style accompanied widespread emergence of the Troodos Massif during the middle Miocene (Robertson, 1977, 1990; Eaton and Robertson, 1993) along with a relative N-S to NW-SE shift in plate motion between Africa and Eurasia (Jolivet et al., 2006). This culminated in late Tortonian deformation in the upper Pakhna Fm. (Symeou et al., 2018). The Episkopi tectonic event is the name given to local expression of these tectonic events along the southern continental margin of the Troodos Massif. It involved a new regional compressional regime, which triggered massive MTDs south of the Troodos during collision and emplacement of the Kyrenia Range (Robertson, 1977; Eaton and Robertson, 1993; Lord et al., 2009; Papadimitrioua et al., 2018; Chen et al., 2019) and the collision of the Eratosthenes Seamount with the Cyprus Arc System (Papadimitrioua et al., 2018).

Final closure of the Indian Gateway (Fig. 22E) indicates the end of the Neotethys Ocean and inception of the Mediterranean Sea (Fig. 22E and F) between the Serravallian and early Tortonian, i.e., from ~ 13.8 to 11 Ma (Rögl, 1998, 1999; Popov et al., 2004; Harzhauser et al., 2007; Hüsing et al., 2009; Hamon et al., 2013; de la Vara and Meijer, 2016). Final closure conditioned: a) global scale changes in oceanic circulation due to termination of equatorial westward circulation (Reid, 1979; Bryden and Kinder, 1991; Torfstein and Steinberg, 2020), b) a wide gateway connection between the Mediterranean Sea and the Atlantic (Capella et al., 2017, 2019), c) a greater role for the Atlantic Ocean in Mediterranean oceanographic processes, with full establishment of an anti-estuarine circulation (Figs. 22E and Fig. S3) similar to the present (Hamon et al., 2013; de la Vara and Meijer, 2016), d) cooling and a salinity increase in the Mediterranean Sea (Karami et al., 2011), e) sourcing of Mediterranean water for warm and saline intermediate waters strengthening both the NADW and AMOC in the Atlantic Ocean (Ivanovic et al., 2013), f) spreading of cooler, fresh Indian water to depths of 3000 m within the Indian Ocean and south towards the Southern Ocean, coeval with ice sheet expansion in the Antarctic (Hamon et al., 2013), g) ecosystem and marine life redistribution (Renema et al., 2008; Bianchi et al., 2012), and h) increased carbon and silica burial in the region (Allen and Armstrong, 2008). These changes in ocean circulation coincided with the onset of global cooling (Fig. 21) from the middle Miocene 'warm house' to more recent 'icehouse' climates (Westerhold et al., 2020).

Middle and late Miocene convergence between Africa and Eurasia caused westward displacement of the Alboran (micro) plate to form the Gibraltar Arc (Vergés and Fernàndez, 2012). Disruption of the connection between the Mediterranean Sea and the Atlantic led the Mediterranean to become a marginal sea (Flecker et al., 2015). Between ~ 11.6 and 7.2 Ma, following the convergent phase, two main corridors formed south of Spain (Betic) and north of Morocco (Rifean) to allow MOW overflow into the Atlantic (Capella et al., 2017, 2019; Krijgsman et al., 1999; de Weger et al., 2020, 2021; Ng et al., 2021, 2022). During the late Messinian, shallowing/closure of these corridors produced the Messinian Salinity Crisis (MSC) between 5.97 and 5.33 Ma, and associated late Miocene cooling (Hsü et al., 1973; CIESM, 2008; Roveri et al., 2014; Flecker et al., 2015; Herbert et al., 2016; Krijgsman et al., 1999). By the end of the Miocene, the connection between the Mediterranean Sea and the Atlantic Ocean was re-established through the Strait of Gibraltar (Rogerson et al., 2012; Krijgsman et al., 1999), which allowed for relatively rapid warming of ~ 3°C to 4°C around middle latitudes in the early Pliocene (Herbert et al., 2016).

7.5. Conceptual implications

7.5.1. Sedimentological implications: diagnostic criteria for contourites, reworked turbidites, turbidites and pelagites

Detailed sedimentologic analysis has provided some criteria for discriminating facies-scale bottom current deposits from turbidites or other deepwater pelagic deposits. Specific contourite sedimentary facies

have been described by a number of studies (e.g., Stow and Lovell, 1979; Stow, 1982; Stow and Holbrook, 1984; Stow and Piper, 1984; Pickering et al., 1989; Faugères and Stow, 1993; Gao et al., 1998; Faugères et al., 1999; Stow et al., 2002a, 2013a, 2013b; Rebesco, 2005; Llave et al., 2006; Øvrebø et al., 2006; Shanmugam, 2006, 2012; Shanmugam, 2014; Stow and Faugères, 2008; Stow et al., 2013a, 2013b; Rebesco et al., 2014; de Castro et al., 2020, 2021a, 2021b; Stow and Smillie, 2020; de Weger et al., 2021; Hüneke et al., 2021; Rodrigues et al., 2022a). Recent research proposes new diagnostic criteria for contouritic sedimentary facies (Alonso et al., 2016; Brackenridge et al., 2018; Rodríguez-Tovar and Hernández-Molina, 2018; de Castro et al., 2020, 2021a, 2021b; Stow and Smillie, 2020; Yu et al., 2020; de Weger et al., 2021; Hüneke et al., 2021; Rodríguez-Tovar, 2022) based on statistical analyses (as Principal Component Analysis, PCA) of texture, microfacies, ichnological features and geochemical data (X-ray fluorescence, XRF).

The main diagnostic criteria for discriminating ancient contourite deposits applied in this work can be summarized in terms of evidence of: sedimentary condensation (*sensu* Föllmi, 2016), reworking, reactivation surfaces, smaller grain-size variations, small-scale hiatuses, sedimentary condensation/omission, variations in sedimentary processes (bed load *versus* suspension load), current velocity, sedimentation rates, and paleo-environmental conditions. Such criteria have been proposed and evaluated by numerous reports (McCave, 2008; Stow et al., 2008; Rebesco et al., 2014; Rodríguez-Tovar et al., 2019a, 2019b; de Castro et al., 2020, 2021a, 2021b; de Weger et al., 2021; Hüneke et al., 2021; Rodrigues et al., 2022a). More specific diagnostic criteria include: a) particles representing bioclasts from skeletons of planktonic biota recycled from deep-marine pelagic muds, b) bands of coarser grainstone with higher concentration and/or reworking of foraminifera (and other bioclast types) within calcarenite beds, c) muddy contourites varying from mud-supported (wackestones) to grain-supported (packstones) and back again, d) intensely, pervasively bioturbated contourite beds with indistinct boundaries, e) mud-rich (packstone) and heterogeneous middle parts of particle-supported contourite beds relative to particle-supported lower parts of turbidite beds (globigerinid grainstones), and f) wavy layering in sandy contourites with local faint lamination or parallel- and cross-lamination (traction sedimentary structures) characterised by layer-specific proportions of bioclasts.

Two primary conceptual frameworks have emerged in the characterisation and identification of contourites. The first focuses on the presence and abundance of bioturbation (Gonthier et al., 1984), and the second focuses on primary sedimentary structures as a basic criterion for contourite recognition (Shanmugam et al., 1993a, 1993b; Shanmugam, 2000; Martín-Chivelet et al., 2003, 2008). The two different approaches (Stow *versus* Shanmugam) arose because researchers were addressing fine-grained contourite deposits within drifts as well as sandier parts of contourite and mixed depositional systems. A pragmatic approach would apply each of these frameworks to different systems, depending on research objectives. Cases like the present study suggest that primary sedimentary processes should receive priority over secondary processes such as biological activity. Ichnological features (Wetzel et al., 2008; Rodríguez-Tovar and Hernández-Molina, 2018; Miguez-Salas and Rodríguez-Tovar, 2019a, 2019b, 2021; Rodríguez-Tovar et al., 2019a, 2019b) and key microfacies (de Castro et al., 2020; de Castro et al., 2021a, 2021b; Yu et al., 2020; Hüneke et al., 2021; de Weger et al., 2021) can also confirm contouritic processes.

The main evidence used to discriminate bottom-current reworked turbidites (BCRS) in this work are: a) their presence in upper parts of the turbidite intervals, b) lamination and repeated inverse-to-normal grading within layers, and c) poorer sorting and declining proportions of shallow-water bioclasts layer by layer. Stanley (1987, 1988) defined turbidites reworked by bottom currents. Shanmugam et al. (1993a, 1993b) proposed criteria based on a turbidite-dominated, mixed system in the Gulf of Mexico, where contouritic reworking of sediment mainly took place between turbidite channels within the slope. The sandy contourites described in these studies consist of discretely rippled and well-sorted, very fine to fine-grained sand layers. They are referred to as bottom-current reworked sands (BCRS). Shanmugam et al. (1993a, 1993b) asserted that the term BCRS is preferable to that of sandy contourite (Stow and Lovell, 1979; Gonthier et al., 1984) because it distinguishes the former phenomena from more conventional sandy contourites. Bioturbation is not considered a diagnostic criterion for BCRS. Recent studies further define BCRS as formed by partial, near-source reworking of a non-contouritic deposit by a bottom current (de Castro et al., 2020, 2021a, 2021b). Partial reworking of a turbidite division (usually the top) with only minor sediment transport would qualify as BCRS. They may or may not include a component of lateral displacement, and usually appear in a contourite drift environment, for example in the channel-drift transition (de Castro et al., 2020, 2021a; de Weger et al., 2021), or in mixed levee-drift systems (Shanmugam et al., 1993a, 1993b; Fonnesu et al., 2020; Fuhrmann et al., 2020; Rodrigues et al., 2022a, 2022b). Mutti et al. (2014) defined a facies association similar to BCRS in which genetically distinct processes (turbidity currents and bottom currents) produce vertically and laterally associated facies. Most of these reworked sands show only minor bioturbation, but *Planolites* is usually present. The bioturbation is concentrated along upper surfaces. Signs of reworking at the top indicate bottom currents affecting some turbidites after deposition (Stanley, 1987, 1988, 1993; de Castro et al., 2020, 2021a; Miguez-Salas and Rodríguez-Tovar, 2021). Complete reworking of the whole bed —or cases where eroded turbidite beds only appear in burrow fills below the erosional surface— confirm this (Rodríguez-Tovar et al., 2019a).

Many authors have described the general sedimentological characteristics of turbidites (e.g., Bouma, 1962; Stow and Shanmugam, 1980; Lowe, 1982; Mutti, 1992, 2011; Mulder, 2011) and low density turbidites (Lowe, 1982; Postma, 1986; Stanley, 1987, 1988, 1993; de Castro et al., 2020, 2021a; de Weger et al., 2021; Hüneke et al., 2021). The main diagnostic criteria for their identification in this work are: a) generally sharp-based beds, b) general normal grading visible in outcrops or based on microfacies as a clear trend from particle-supported textures (grainstones) to mud-supported textures (wackestones), c) massive lower part or intervals from the Bouma sequence, d) preservation of well-defined lamination (parallel- and cross-lamination), e) intensively bioturbated tops (with increasing homogenization towards the top), f) particles sourced from shallow marine environments (as indicated by benthic bioclasts), and g) embedded planktonic bioclasts (partially) incorporated by seabed erosion due to the erosive capacity of the density flow.

Previous research has established sedimentological characteristics for pelagic or hemipelagic deposits (Hesse, 1975; O'Brien et al., 1980; Stow and Tabrez, 1998; Hüneke and Henrich, 2011; Pickering and Hiscott, 2016). In modern and ancient sedimentary records, where these deposits interstratify with low-density turbiditic and finer-grained bottom current deposits (Stow and Smillie, 2020; de Castro et al., 2021a; de Weger et al., 2021). The diagnostic criteria for discriminating pelagic/hemipelagic deposits from muddy contourites include: a) consistent concentration of bioclasts (forams) in particular lamina, b) extensive bioturbation, and c) shells empty or filled with mud that matches the overall matrix. If sediment infill differs from the surrounding matrix, these allochthonous bioclasts then indicate reworking and re-deposition by the influence of weak bottom currents as previously reported by Hüneke et al. (2021).

7.5.2. Implications for energy geosciences

Deepwater deposits have received increasing interest due to their petroleum and carbon storage potential. Sandy contourites and reworked turbidites can serve as deepwater reservoirs and contribute to potential plays (Viana et al., 2007; Viana, 2008; Mutti and Carminatti, 2012; Shanmugam, 2012; Shanmugam, 2006; Shanmugam, 2017; Mutti et al., 2014; Fonnesu et al., 2020) since they often exhibit the petrophysical characteristics of high porosity, high permeability (Yu et al., 2020) and good lateral and vertical transmissibility of fluids (Viana,

2008; Shanmugam, 2012). In fact, new deepwater gas discovery in 2022 in the Guajira margin offshore Colombia (Uchuva-1, Tayrona Block) are in a very similar basin slope setting in the upper plate of an active margin (Leslie and Mann, 2020; Vence and Mann, 2020) and deep water deposits compared with studied outcrops onshore Cyprus.

The deposits described here are a good analogue for sandy contourites that attain 30-40 m thicknesses and offer a porous and permeable medium in deep-marine deposits. Units are composed almost entirely of planktonic forams and give primary porosities of 10 - 14%, permeability of 190 md, and net-to-gross (NTG) of 26/130 m at Petra Tou Romiou. These values exceed the ones measured from average post-diagenetic carbonates (Choquette and Pray, 1970). Diagenetic processes of compaction and cementation reduce primary porosity, but fracturing, dissolution, recrystallisation and fluid migration create secondary porosity and permeability, which give augmented porosity of up to 21% at Agios Konstantinos (NTG of 28/70 m). Such values would allow the units to serve as reservoirs with good fluid mobility. Similar sandy contourite deposits in Indonesia have intervals with a porosity of 30-45% and 100-1000 md permeability (Schiller et al., 1994). Reworked turbidites containing more homogenous sands could give higher porosity than classical turbidites, owing to the redistribution of finer particles as a result of bottom current action. Moreover, in the studied sections, applications of techniques such as X-ray micro-computed tomography (Micro-CT), mercury intrusion porosimetry, and analysis of impregnated thin sections have served to reveal the impact of ichnological feaures on rock properties (e.g., porosity and permeability), particularly in contourites (Dorador et al., 2021; Miguez-Salas et al., 2021, 2022; Rodríguez-Tovar et al., 2021).

8. Conclusions

Outcrops from Cyprus offer a unique example of ancient carbonate contourites. Formed from the late Eocene to the middle Miocene, these finer- and coarser-grained deposits interstratify with pelagic/hemipelagic, turbidite and mass-transports deposits (MTDs). Deepwater deposits developed along a basin slope located in the upper plate of an active margin as it transitioned from an initial wide basin to a series of shallower, segmented sub-basins in a complex compressional setting. The basin underwent tectonic pulses over different time scales related to regional compressive-flexural stress fields and external environmental processes (sea level, climate and oceanic circulation) over time. These factors influenced long-term sedimentary variations, packages of strata (P) with shallowing-upward trend and shorter-term thickening upward sequences, which determine a clear repetition in the sedimentary stacking pattern, where the onset and buried of Contourites Depositional Systems and the stratigraphic position of the sandier contourites deposits is not random.

Two long-term contourite depositional systems developed. An Eocene system consists primarily of finer-grained contourites, while a late Oligocene to middle Miocene system was dominated by coarser-grained contourites. Both systems are buried by extensive marl deposits that record variation in deep (circulating NW) and intermediate (circulating SE) water masses, respectively, because of plate tectonics that conditioned the enhancement of subduction processes south of Cyprus and the evolving exchange between the Neotethys Ocean and the Indian and Atlantic oceans until the final closure of the Indian Gateway in the middle Miocene. This closure coincided with the emergence of the Troodos Massif, the collision and emplacement of the Kyrenia Range by the Troodos Massif, and the collision of the Eratosthenes Seamount with the Cyprus Arc System. Following these events, contourite deposition ceased. A new circulation regime was established with the final inception of the Mediterranean Sea.

Contourites represent bi-gradational sequences that normally appear in association with contourite drifts, the asymmetric top-cut sequences being characteristic of plastered drift and contourite terraces. The presence of plastered drift in the offshore basins north of the subduction zone might support a similar depositional environment during the Eocene to early Miocene during to regional uplift, while continuation of more local uplift by Troodos diverge their evolution during later parts of the Miocene. The coarser (sandy) contourites formed during the latest Oligocene to middle Miocene are divided into three packages: package I is Chattian (late Oligocene), package II is Aquitanian/Burdigalian (early Miocene), and package III is Langhian (middle Miocene). Contourites evidencing enhanced bottom current episodes towards the top of the packages are buried by later extensive marl deposits. Sandy contourites thus appear to have formed during compressive phases with subsequent finer-grained sedimentation during the flexural phases. Coevally to these pulses, turbidites and MTDs developed during compressional phases. In conjunction with pelagic/hemipelagic processes, they provide the sediment supply for the contourite deposits after winnowing and reworking.

The diagnostic criteria for discriminating ancient bottom current deposits from other deepwater deposits in the ancient record includes sedimentary condensation, reworking, reactivation surfaces, smaller grain-size variations, small-scale hiatuses, and omission surfaces. All of these vary depending on current velocity, sedimentation rate, and paleoenvironmental conditions. The results described here highlight the importance of primary sedimentary structures, microfacies and ichnological features as the best diagnostic criteria for discriminating contourites and reworked turbidites at the sedimentary facies scale. Deepwater sandy contourites (with ripples and occasional sandy dunes) are a result of the reworking of pelagic/hemipelagic deposits or turbidites. Such deposits reach 30-40 m in thickness and can have petrophysical properties making them relevant as reservoirs in the context of energy geosciences.

This work documents the role of plate tectonics and the evolution of oceanic gateways in driving paleo-oceanic circulation, which in turn influenced sedimentary processes, shaping oceanic basins and continental margins. Our research can facilitate interpretations of other present day or ancient deepwater continental margins. Future high-resolution analysis may fine-tune the description and interpretation of deepwater systems and the role of contourites during their evolution. As such, contourites can record and help determine local, regional and global environmental processes, including —but not limited to— oceanic circulation.

Supplementary data to this article can be found online at https://doi.org/10.1016/j.gloplacha.2022.103983.

Declaration of Competing Interest

Heriot Watt University, D.Stow@hw.ac.uk
The University of Texas, shanshanmugam@aol.com
Colorado School of Mines,Golden, Colorado, lwood@mines.edu

Data availability

Data will be made available on request.

Acknowledgements

This work was funded through the Joint Industry Project (JIP) supported by BP (United Kingdom), ENI (Italy), TOTAL (France), ExxonMobil (United States), Wintershall Dea (Germany) and TGS (United Kingdom) within the framework of “The Drifters” Research Group at Royal Holloway University of London (RHUL), and it is related to the projects CTM 2012-39599-C03, CGL2016-80445-R and CTM2016-75129-C3-1-R. Financial support of the Deutsche Forschungsgemeinschaft (DFG) is gratefully acknowledged (HU 804/11-1). We thank the Cyprus Geological Survey for scientific collaboration and support, in particular *Costas Constantinou* and *Efthymios Tsiolakis*. We thank A. Creaser, L. Hyslop (RHUL), D.A.W. Stow (Heriot-Watt University) and A. Viana (PETROBRAS) for valuable help and discussions

during field campaigns. We are also grateful to S. Suklap and B. Docherty for their analysis on microfacies during their MSc. in 2016. Thanks to Dr. G. Blackbourn (Blackbourn Geoconsulting) for his petrographic analysis; F. Sierro (Univ. Salamanca, Spain), RPS Energy Ltd and PalaeoVision Ltd for their biostratigraphic analysis of the samples and A. Maestro (IGME, Spain) for the basemap in Fig. 1. A. de la Vara's contribution is based on work done during her PhD at Utrecht University, supervised by Paul Meijer. We thank the editor, *Gabriel Tagliaro* and one anonymous reviewer for their positive comments which helped us to improve considerably our manuscript.

References

Allen, M.B., Armstrong, H.A., 2008. Arabia–Eurasia collision and the forcing of mid Cenozoic global cooling. Palaeogeogr. Palaeoclimatol. Palaeoecol. 265 (1), 52–58. https://doi.org/10.1016/j.palaeo.2008.04.021.

Alonso, B., Ercilla, G., Casas, D., Stow, D.A.V., Rodríguez-Tovar, F.J., Dorador, J., Hernández-Molina, F.J., 2016. Contourite vs gravity-flow deposits of the Pleistocene Faro Drift (Gulf of Cadiz): sedimentological and mineralogical approaches. Mar. Geol. 377, 77–94. https://doi.org/10.1016/j.margeo.2015.12.016.

Anastas, A.S., Dalrymple, R.W., James, N.P., Nelson, C.S., 1997. Cross-bedded calcarenites from New Zealand: subaqueous dunes in a cool-water Oligo-Miocene seaway. Sedimentology 44, 869–891.

Anovitz, L.M., Cole, D.R., 2015. Characterization and analysis of porosity and pore structures. Rev. Mineral. Geochem. 80 (1), 61–164. https://doi.org/10.2138/rmg.2015.80.04.

Babonneau, N., Raisson, F., Genêt, A., Lopes, U., Fierens, R., Miramontes, E., Révillon, S., Rabineau, M., Droz, L., Belleney, D., Moulin, M., M. and Aslanian, D., 2022. Contourite on the Limpopo Corridor, Mozambique margin: Long-term evolution, facies distribution and Plio-Quaternary processes. Sedimentology. https://doi.org/10.1111/sed.13045. Accepted Author Manuscript.

Bádenas, B., Pomar, L., Aurell, M., Morsilli, M., 2012. A facies model for internalites (internal wave deposits) on a gently sloping carbonate ramp (Upper Jurassic, Ricla, NE Spain). Sediment. Geol. 271–272, 44–57. https://doi.org/10.1016/j.sedgeo.2012.05.020.

Bahr, A., Kaboth-Bahr, S., Karas, C., 2022. The opening and closure of oceanic seaways during the Cenozoic: pacemaker of global climate change? Geol. Soc. Lond., Spec. Publ. 523 https://doi.org/10.1144/SP523-2021-54.

Bailey, W.S., McArthur, A.D., McCaffrey, W.D., 2021. Distribution of contourite drifts on convergent margins: examples from the Hikurangi subduction margin of New Zealand. Sedimentology 68, 294–323. https://doi.org/10.1111/sed.12779.

Balaky, S.M., Tamar-Agha, M.Y., 2017. Sedimentology and stratigraphy of Geli Khana Formation (Anisian–Ladinian), a contourite depositional system in the northeastern passive margin of Arabian plate, northern Iraq-Kurdistan region. Arab. J. Geosci. 10 (5), 118.

Barker, P.F., Camerlenghi, A., Acton, G.D., Ramsay, A.T.S., et al., 2002. Proceedings of the Ocean Drilling Program, Scientific Results 178 (CD-ROM). Available from Ocean Drilling Program. Texas A &M University, College Station, TX, U.S.A.

Barker, P.F., Filippelli, G.M., Florindo, F., Martin, E.E., Scher, H.D., 2007. Onset and role of the antarctic circumpolar current. Deep-Sea Res. II Top. Stud. Oceanogr. 54 (21), 2388–2398.

Barron, J.A., Keller, G., 1982. Widespread Miocene deep-sea hiatuses: coincidence with periodsof global cooling. Geology 10 (11), 577581.

Berger, W.H., Piper, D.J.W., 1972. Planktonic foraminifera: differential settling, dissolution and redeposition. Limnol. Oceanogr. 17, 275–287. https://doi.org/10.4319/lo.1972.17.2.0275.

Berggren, W.A., 1982. Role of Ocean Gateways in Climate Change. In: Climate in Earth History. Studies in Geophysics. National Academy Press, Washington D.C., pp. 118–125

Berra, F., Angiolini, L., 2014. The evolution of the Tethys region throughout the Phanerozoic: a brief tectonic reconstruction. In: Marlow, L., Kendall, C., Yose, L. (Eds.), Petroleum Systems of the Tethyan Región, AAPG Memoir, 106, pp. 1–27.

Bianchi, C.N., Morri, C., Chiantore, M., et al., 2012. Mediterranean sea biodiversity between the legacy from the past and a future of change. In: En: Life in the Mediterranean Sea: A Look at Habitat Changes (Noga Stambler, Ed.), pp. 1–55.

Bijl, P.K., Houben, A.J.P., Hartman, J.D., Pross, J., Salabarnada, A., Escutia, C., et al., 2018. Paleoceanography and ice sheet variability offshore Wilkes Land, Antarctica - Part 2: insights from OligoceneMiocene dinoflagellate cyst assemblages. Clim. Past 14, 1015–1033. Available from: https://doi.org/10.5194/cp-14-1015-2018.

Billups, K., 2002. Late Miocene through early Pliocene deep water circulation and climate change viewed from the sub-Antartic South Atlantic. Palaeogeogr. Palaeoclimatol. Palaeoecol. 185, 287–307.

Billups, K., Schrag, D.P., 2002. Paleotemperatures and ice volume of the past 27 Myr revisited with paired Mg/Ca and 18O/16O measurements on benthic foraminifera. Paleoceanography 17 (1), 1003.

Boulila, S., Galbrun, B., Laskar, J., Palike, H., 2012. ~9 My cycle in Cenozoic d13C record and long-term orbital eccentricity modulation: Is there a link? Earth Planet. Sci. Lett. 317–318, 273–281.

Boulila, S., Laskar, J., Haq, B.U., Galbrun, B., Hara, N., 2018. Long-term cyclicities in Phanerozoic sea-level sedimentary record and their potential drivers. Glob. Planet. Chang. 165, 128–136.

Boulila, S., Brange, C., Cruz, A.M., Laskar, J., Gorini, C., Dos Reis, T., Silva, C.G., 2020. Astronomical pacing of Late Cretaceous third- and second-order sea-level sequences in the Foz do Amazonas Basin. Mar. Pet. Geol. 117, 104382 https://doi.org/10.1016/j.marpetgeo.2020.104382.

Bouma, A.H., 1962. Sedimentology of some flysch deposits. A graphic approach to facies interpretation. Elsevier Publishing Company, Amsterdam, New York, p. 168.

Boyle, P.R., Romans, B.W., Tucholke, B.E., Norris, R.H., Swift, S.A., Sexton, P.F., 2017. Cenozoic North Atlantic deep circulation history recorded in contourite drifts, offshore Newfoundland, Canada. Mar. Geol. 385, 185–203. https://doi.org/10.1016/j.margeo.2016.12.014.

Brackenridge, R.E., Stow, D.A.V., Hernández-Molina, F.J., Jones, C., Mena, A., Alejo, I., Ducassou, E., Llave, E., Ercilla, G., Nombela, M.A., Pérez-Arlucea, M., Frances, G., 2018. Textural characteristics and facies of sand-rich contourite depositional systems. Sedimentology 65, 2223–2252.

Brew, G., Barazangi, M., Al-Maleh, A.K., Sawaf, T., 2001. Tectonic and geologic evolution of Syria. GeoArabia 6 (4), 573–616. https://doi.org/10.1190/1.1438571.

Bryden, H.L., Kinder, T.H., 1991. Steady two-layer exchange through the Strait of Gibraltar. Deep Sea Res. Part A Ocea. Res. Papers 38, S445–S463.

Burky, D., 1974. Coccoliths as paleosalinity indicators — evidence from Black Sea. Black Sea Geol., Chem. Biol. Mem. 20, 353–363.

Butzin, M., Lohmann, G., Bickert, T., 2011. Miocene ocean circulation inferred from marine carbon cycle modeling combined with benthic isotope records. Paleoceanography 26, PA1203. https://doi.org/10.1029/2009PA001901.

Calon, T.J., Aksu, A.E., Hall, J., 2005. The Oligocene-Recent evolution of the Mesaoria Basin (Cyprus) and its western marine extension, Eastern Mediterranean. Mar. Geol. 221, 95–120.

Cande, S.C., Stock, J.M., 2004. Cenozoic reconstructions of the Australia–New Zealand–South Pacific sector of Antarctica. The Cenozoic Southern Ocean: tectonics, sedimentation and climate change between Australia and Antarctica. Geophys. Monograph Ser. 151, 5–18.

Capella, W., Hernández-Molina, F.J., Flecker, R., Hilgen, F.J., Hssain, M., Kouwenhoven, van Oorschot, M., Sierro, F.J., Stow, D.A.V., Trabucho-Alexandre, J., Tulbure, M.A., Yousfi, M.Z., Krijgsman, W., 2017. Sandy contourite drift in the late Miocene Rifian Corridor (Morocco): reconstruction of depositional environments in a foreland-basin seaway. Dev. Sedimentol. 355, 31–57.

Capella, W., Flecker, R., Hernández-Molina, F.J., Simon, D., Meijer, P.T., Rogerson, M., Sierro, F.J., Krijgsman, W., 2019. Mediterranean isolation preconditioning the Earth System for late Miocene climate cooling. Sci. Rep. 9 (1), 3795. https://doi.org/10.1038/s41598-019-40208-2.

Carter, R.M., McCave, I.N., Richter, C., Carter, L., et al., 1999. Proceedings of the Ocean Drilling Program, Initial Reports, Vol. 181.

Catuneanu, O., 2022. Principles of Sequence Stratigraphy, Second Edition). Elsevier, p. 454. https://doi.org/10.1016/C2009-0-19362-5.

Catuneanu, O., Abreu, V., Bhattacharya, J.P., Blum, M.D., Dalrymple, R.W., Eriksson, P. G., Fielding, C.R., Fisher, W.L., Galloway, W.E., Gibling, M.R., Giles, K.A., 2009. Towards the standardization of sequence stratigraphy. Earth Sci. Rev. 92 (1–2), 1–33.

Chen, G., Robertson, A.H.F., Ustaömer, T., 2019. U–Pb detrital zircon ages used to infer provenance and tectonic setting of Late Triassic–Miocene sandstones related to the Tethyan development of Cyprus. J. Geol. Soc. Lond. 176 (5) https://doi.org/10.1144/jgs2018-207 jgs2018-207.

Choquette, P.W., Pray, L.C., 1970. Geologic nomenclature and classification of porosity in sedimentary carbonates. Am. Assoc. Petrol. Geol. Bull. 54 (2), 207–250.

CIESM, 2008. The Messinian Salinity Crisis from mega-deposits to microbiology – A consensus report. In: CIESM workshop Monographs (F.Biand, Ed.) Monaco, 33, p. 168.

Cloetingh, S., Gradstein, F.M., Kooi, H., Grant, A.C., Kaminski, M., 1990. Plate reorganization: a cause of rapid late neogene subsidence and sedimentation around the North Atlantic? J. Geol. Soc. Lond. 147, 495–506.

Clube, T.M.M., Robertson, A.H.F., 1986. The palaeorotation of the Troodos microplate, Cyprus in the Late Mesozoic-Early Cenozonic plate tectonic framework of the Eastern Mediterranean. Surv. Geophys. 8, 361–375.

Cochran, J.R., 1990. Himalayan uplift, sea level, and the record of Bengal Fan sedimentation at the ODP Leg 116 sites. In: Cochran, J.R., Stow, D.A.V., et al. (Eds.), Proc. ODP, Sci. Results, 116. Ocean Drilling Program, College Station, TX, pp. 397–414.

Cogné, J.-P., Humler, E., 2004. Temporal variation of oceanic spreading and crustal production rates during the last 180 my. Earth Planet. Sci. Lett. 227 (3-4), 427–439.

Coltice, N., Seton, M., Rolf, T., Müller, R.D., Tackley, P.J., 2013. Convergence of tectonic reconstructions and mantle convection models for significant fluctuations in seafloor spreading. Earth Planet. Sci. Lett. 383, 92–100.

Cramer, B.S., Miller, K.G., Barrett, P.J., Wright, J.D., 2011. Late CretaceousNeogene trends in deep ocean temperature and continental ice volume: reconciling records of benthic foraminiferal geochemistry (δ18O and Mg/Ca) with sea level history. J. Geophys. Res. Oceans 116 (C12), C12023.

Cramwinckel, M.J., Huber, M., et al., 2018. Synchronous tropical and polar temperature evolution in the Eocene. Nature 559, 382–386. https://doi.org/10.1038/s41586-018-0272-2.

Creaser, A., Hernández-Molina, F.J., Badalini, G., Thompson, P., Walker, R., Soto, M., Conti, B., 2017. A late cretaceous mixed (turbidite-contourite) system along the Uruguayan margin: sedimentary and palaeoceanographic implications. Mar. Geol. 390, 234–253. https://doi.org/10.1016/j.margeo.2017.07.004.

Culp, J., Parent, A.M., Abolfazli, E., Strom, K., Romans, B.W., 2021. Advective sorting of silt by currents: a laboratory study. Sedimentology. https://doi.org/10.1111/sed.12889.

Cyprus Geological Survey, 2005. Tectonic Evolution. Geology of Cyprus.

Cyprus Geological Survey, 2017. AAPG January 2017 - Field Trips in Cyprus.
de Castro, S., Hernández-Molina, F.J., Rodríguez-Tovar, F.J., Llave, E., Ng, Z.L., Nishida, N., Mena, A., 2020. Contourites and bottom current reworked sands: Bed facies model and implications. Mar. Geol. 428, 106267 https://doi.org/10.1016/j.margeo.2020.106267.
de Castro, S., Hernández-Molina, F.J., de Weger, W., Jimenez-Espejo, F.J., Rodríguez-Tovar, F.J., Mena, A., Llave, E., Sierro, F.J., 2021a. Contourite characterization and its discrimination from other deep-water deposits in the Gulf of Cadiz contourite depositional system. Sedimentology 68 (3), 987–1027. https://doi.org/10.1111/sed.12813.
de Castro, S., Miramontes, E., Dorador, J., Jouet, G., Cattaneo, A., Rodríguez-Tovar, F.J., Hernandez-Molina, F.J., 2021b. Siliciclastic and bioclastic contouritic sands: textural and geochemical characterisation. Mar. Pet. Geol. 128, 105002 https://doi.org/10.1016/j.marpetgeo.2021.105002.
de la Vara, A., Meijer, P., 2016. Response of Mediterranean circulation to Miocene shoaling and closure of the Indian Gateway: a model study. Palaeogeogr. Palaeoclimatol. Palaeoecol. 442, 96–109. Elsevier. https://doi.org/10.1016/j.palaeo.2015.11.002.
de Weger, W., Hernández-Molina, F.J., Flecker, R., Sierro, F.J., Chiarella, D., Krijgsman, W., Manar, M.A., 2020. Late Miocene contourite channel system reveals intermittent overflow behavior. Geology 48 (12), 1194–1199.
de Weger, W., Hernández-Molina, F.J., Miguez-Salas, O., de Castro, S., Bruno, M., Chiarella, D., Sierro, F.J., Blackbourn, G., Manar, M.A., 2021. Contourite depositional system after the exit of a strait: case study from the late Miocene South Rifian Corridor. Morocco. Sedimentol. 68 (7), 2996–3032. https://doi.org/10.1111/sed.12882.
de Weger, W., Hernández-Molina, F.J., Miguez-Salas, O., de Castro, S., Bruno, M., Chiarella, D., Sierro, F.J., Blackbourn, G., Manar, M.A., 2021. Contourite depositional system after the exit of a strait: Case study from the late Miocene South Rifian Corridor, Morocco. Sedimentology. https://doi.org/10.1111/sed.12882.
Derbyshire, E., 1996. Quaternary glacial sediments, glaciation style, climate and uplift in the Karakoram and nortwest Himalaya: review and speculations. Palaeogeogr. Palaeoclimatol. Palaeoecol. 120, 147–157.
Dercourt, J., Zonenshain, L.P., Ricou, L.E., Kazmin, V.G., Le Pichon, X., Knipper, A.L., Grandjacquet, C., Sbortshikov, I.M., Geyssant, J., Lepvrier, C., Pechersky, D.H., Boulin, J., Sibuet, J.C., Savostin, L.A., Sorokhtin, O., Westphal, M., Bazhenov, M.L., Lauer, J.P., Biju-Duval, B., 1986. Geological evolution of the Tethys belt from the Atlantic to the Pamirs since the Lias. Tectonophysics 123, 241–315.
Dickinson, W.R., 1995. Forearc basins. In: Busby, C., Ingersoll, R.V. (Eds.), Tectonics of Sedimentary Basins. Blackwell, Oxford, pp. 221–261.
Dorador, J., Rodríguez-Tovar, F.J., Miguez-Salas, O., 2021. The complex case of Macaronichnus trace fossil affecting rock porosity. Sci. Rep. 11 (1), 1–7. https://doi.org/10.1038/s41598-021-81687-6.
Douglas, P.M., Affek, H.P., Ivany, L.C., Houben, A.J., Sijp, W.P., Sluijs, A., et al., 2014. Pronounced zonal heterogeneity in Eocene southern high-latitude sea surface temperatures. Proc. Natl. Acad. Sci. 111, 6582–6587. https://doi.org/10.1073/pnas.1321441111.
Duan, T., Gao, Z., Zeng, Y., Stow, D.A.V., 1993. A fossil carbonate contourite drift on the Lower Ordovician palaeocontinental margin of the middle Yangtze Terrane, Jiuxi, northern Hunan, southern China. Sediment. Geol. 82, 271–284.
Dunham, R.J., 1962. Classification of carbonate rocks according to depositional texture. In: Classification of Carbonate Rocks (Ed. Ham, W.E.), 1. AAPG Mem, pp. 108–121.
Eagles, G., Jokat, W., 2014. Tectonic reconstructions for paleobathymetry in Drake Passage. Tectonophysics 611, 28–50.
Eaton, S., Robertson, A.H.F., 1993. The Miocene Pakhna formation, southern Cyprus and its relationship to the Neogene tectonic evolution of the Eastern Mediterranean. Sediment. Geol. 86, 273–296.
Edwards, S., Hudson-Edwards, K., Cann, J., Malpas, J., Xenophontos, C., 2010. Cyprus. In: Classic Geology in Europe 7. Terra Publishing, Dunedin Academic Press Ltd., p. 271
Evangelinos, D., Escutia, C., Etourneau, J., Hoem, F., Bijl, P., Boterblom, W., et al., 2020. Late Oligocene-Miocene proto-Antarctic circumpolar current dynamics off the Wilkes Land margin, East Antarctica. Glob. Planet. Chang. 191, 103221. Available from: https://doi.org/10.1016/j.gloplacha.2020.103221.
Exon, N.F., Kennett, J.P., Malone, M.J., Brinkhuis, H., Chaproniere, G.C.H., Ennyu, A., et al., 2001. Proceedings of the Ocean Drilling Program, initial reports, the Tasmanian Gateway, Cenozoic climatic and oceanographic development; covering Leg 189 of the cruises of the drilling vessel JOIDES Resolution; Hobart, Tasmania, to Sydney, Australia; sites 1168-1172, 11 March, 6 May 2000. Proceedings of the Ocean Drilling Program, Part A: Initial Reports, p. 189.
Exon, N.F., Kennett, J.P., Malone, M.J., 2004. Leg 189 synthesis: cretaceous-holocene history of the Tasmanian Gateway. In: Exon, N.F., Kennett, J.P., Malone, M.J. (Eds.), Proceedings of the Ocean Drilling Program. https://doi.org/10.2973/odp.proc.sr.189.2004.
Farrell, S.G., Eaton, S., 1987. Slump strain in the Tertiary of Cyprus and the Spanish Pyrenees. Definition of palaeoslopes and models of soft-sediment deformation. In: Jones, M.E., Preston, R.M.F. (Eds.), Deformation of Sediments and Sedimentary Rocks, 29. Geol. Soc. Lond. Special Publ, pp. 181–196.
Faugères, J.-C., Stow, D.A.V., 1993. Bottom-current-controlled sedimentation: a synthesis of the contourite problem. Sediment. Geol. 82, 287–297.
Faugères, J.C., Stow, D.A.V., 2008. Contourite drifts: nature, evolution and controls. Dev. Sedimentol. 60, 257–288.
Faugères, J.C., Gonthier, E., Stow, D.A.V., 1984. Contourite drift molded by deep Mediterranean outflow. Geology 12, 296–300.
Faugères, J.-C., Stow, D.A.V., Imbert, P., Viana, A.R., 1999. Seismic features diagnostic of contourite drifts. Mar. Geol. 162, 1–38. https://doi.org/10.1016/S0025-3227(99)00068-7.
Flecker, R., Krijgsman, W., Capella, W., de Castro Martíns, C., Dmitrieva, E., Mayser, J.P., Marzocchi, A., Modestou, S., Ochoa, D., Simon, D., Tulbure, M., van den Berg, B., van der Schee, M., de Lange, G., Ellam, R., Govers, R., Gutjahr, M., Hilgen, F., Kouwenhoven, T., Lofi, J., Meijer, P., Sierro, F.J., Bachiri, N., Barhoun, N., Alami, A. C., Chacon, B., Flores, J.A., Gregory, J., Howard, J., Lunt, D., Ochoa, M., Pancost, R., Vincent, S., Yousfi, M.Z., 2015. Evolution of the Late Miocene Mediterranean–Atlantic gateways and their impact on regional and global environmental change. Earth Sci. Rev. 150, 365–392.
Flower, B.P., Kennett, J.P., 1993. Middle Miocene ocean-climate transition: high-resolution oxygen and carbon isotopic records from Deep Sea drilling project site 588A, southwest Pacific. Paleoceanography 8 (6), 811–843.
Flügel, E., 2010. Microfacies of Carbonate Rocks. Analysis, Interpretation and Application. Springer, Berlin, p. 976.
Föllmi, K.B., 2016. Sedimentary condensation. Earth Sci. Rev. 152, 143–180. https://doi.org/10.1016/j.earscirev.2015.11.016.
Follows, E.J., 1992. Patterns of reef sedimentation and diagenesis in the Miocene of Cyprus. In: Sellwood, B.W. (Ed.), Ramps and Reefs. Sediment. Geol., 79, pp. 225–253.
Fonnesu, M., Palermo, D., Galbiati, M., Marchesini, M., Bonamini, E., Bendias, D., 2020. A new world-class deep-water play-type, deposited by the syndepositional interaction of turbidity flows and bottom currents: the giant Eocene Coral Field in northern Mozambique. Mar. Pet. Geol. 111, 179–201. https://doi.org/10.1016/j.marpetgeo.2019.07.047.
Fuhrmann, A., Kane, I.A., Ferguson, R.A., Schomacker, E., Bonamini, E., Contreras, F.A., 2020. Hybrid turbidite-drift channel complexes: an integrated multiscale model. Geology 48. https://doi.org/10.1130/G47179.1.
Galeotti, S., DeConto, R., Naish, T., Stocchi, P., Florindo, F., Pagani, M., Barrett, P., Bohaty, S.M., Lanci, L., Pollard, D., Sandroni, S., Talarico, F.M., Zachos, J.C., 2016. Antarctic ice sheet variability across the Eocene-Oligocene boundary climate transition. Science 352 (6281), 76–80. https://doi.org/10.1126/science.aab0669.
Gao, Z.Z., Eriksson, K.A., He, Y.B., Luo, S.S., Guo, J.H., 1998. Deep-water Traction Current Deposits. A Study of Internal Tides, Internal Waves, Contour Currents and Their Deposits. Science Press, Beijing.
Gass, I.G., 1960. The geology and mineral resources of the Dhali Area. Mem. Geol. Surv. Cyprus 4, 116.
Gong, C., Wang, Y., Zheng, R., Hernández-Molina, F.J., Li, Y., Stow, D.A.V., Xu, Q., Brackenridge, R.E., 2016. Middle Miocene reworked turbidites in the Baiyun Sag of the Pearl River Mouth Basin, northern South China Sea margin: Processes, genesis, and implications. J. Asian Earth Sci. 128, 116–129. https://doi.org/10.1016/j.jseaes.2016.06.025.
Gonthier, E., Faugères, J.-C., Stow, D.A.V., 1984. Contourite facies of the Faro Drift, Gulf of Cadiz. In: Stow, D.A.V., Piper, D.J.W. (Eds.), Fine Grained Sediments, Deepwater Processes and Facies, 15. Geological Society, London, Special Publication, pp. 275–291.
Gradstein, F.M., Ogg, J.G., Schmitz, M.D., Ogg, G.M., 2012. The Geological Time Scale 2012, 1 & 2. Elsevier B.V., p. 1144
Hall, J.K., 1994. Bathymetric chart of the Eastern Mediterranean Sea. In: Scale 1:625,000 Geological Survey of Israel. Marine Geology, Mapping and Tectonics Division.
Hamad, N., Millot, C., Taupier-Letage, I., 2005. A new hypothesis about the surface circulation in the eastern basin of the Mediterranean Sea. Prog. Oceanogr. 66 (2–4), 287–298.
Hamon, N., Sepulchre, P., Lefebvre, V., Ramstein, G., 2013. The role of eastern Tethys seaway closure in the Middle Miocene Climatic Transition (ca. 14 Ma). Clim. Past 9, 2687–2702. https://doi.org/10.5194/cp-9-2687-2013.
Harzhauser, M., Kroh, A., Mandic, O., Piller, W.E., Göhlich, U., Reuter, M., Berning, B., 2007. Biogeographic responses to geodynamics: a key study all around the Oligo–Miocene Tethyan Seaway. Zool. Anz. 246, 241–256. https://doi.org/10.1016/j.jcz.2007.05.001.
Haughton, P., Davis, C., McCaffrey, W., Barker, S., 2009. Hybrid sediment gravity flow deposits – classification, origin and significance. Mar. Pet. Geol. 26, 1900–1918. https://doi.org/10.1016/j.marpetgeo.2009.02.012.
Hawie, N., Gorini, C., Deschamps, R., Nader, F.H., Montadert, L., Granjeon, D., Baudin, F., 2013. Tectono-stratigraphic evolution of the northern Levant Basin (offshore Lebanon). Mar. Pet. Geol. 48, 392–410. https://doi.org/10.1016/j.marpetgeo.2013.08.004.
Hay, W.W., 2009. Cretaceous Oceans and Ocean Modeling. SEPM Spec. Publ. 91, 243–271.
Heezen, B.C., Hollister, C.D., Ruddiman, W.F., 1966. Shaping of the continental rise by deep geostrophic contour currents. Science 152, 502–508.
Henrich, R., Hüneke, H., 2011. Hemipelagic advection and periplatform sedimentation. In: Deep-Sea Sediments (Eds Hüneke, H. and Mulder, T.), 63. Dev. Sedimentol., pp. 353–396
Herbert, T.D., Lawrence, K.T., Tzanova, A., Peterson, L.C., Caballero-Gill, R., Kelly, C.S., 2016. Late Miocene global cooling and the rise of modern ecosystems. Nat. Geosci. 9 (11), 843–847. https://doi.org/10.1038/ngeo2813.
Hernández-Molina, F.J., Paterlini, M., Somoza, L., Violante, R., Arecco, M.A., de Isasi, M., Rebesco, M., Uenzelmann-Neben, G., Neben, S., Marshall, P., 2010. Giant mounded drifts in the Argentine Continental Margin: origins, and global implications for the history of thermohaline circulation. Mar. Pet. Geol. 27 (7), 1508–1530. https://doi.org/10.1016/j.marpetgeo.2010.04.003.
Hernández-Molina, F.J., Stow, D.A.V., Alvarez-Zarikian, C.A., Acton, G., Bahr, A., Balestra, B., Ducassou, E., Flood, R., Flores, J.A., Furota, S., Grunert, P., Hodell, D., Jimenez-Espejo, F., Kim, J.K., Krissek, L., Kuroda, J., Li, B., Llave, E., Lofi, J.,

Lourens, L., Miller, M., Nanayama, F., Nishida, N., Richter, C., Roque, C., Pereira, H., Sanchez Goñi, M.F., Sierro, F.J., Singh, A.D., Sloss, C., Takashimizu, Y., Tzanova, A., Voelker, A.H.L., Williams, T., Xuan, C., 2014. Onset of Mediterranean outflow into the North Atlantic. Science 344, 1244–1250.

Hernández-Molina, F.J., Sierro, F.J., Llave, E., Roque, C., Stow, D.A.V., Williams, T., Lofi, J., Van der Schee, M., Arnáiz, A., Ledesma, S., Rosales, C., 2016. Evolution of the gulf of Cadiz margin and Southwest Portugal contourite depositional system: tectonic, sedimentary and paleoceanographic implications from IODP expedition 339. Mar. Geol. 377, 7–39.

Hernández-Molina, F.J., Campbell, S., Badalini, G., Thompson, P., Walker, R., Soto, M., Conti, B., Preu, B., Thiéblemont, A., Hyslop, L., Miramontes, E., Morales, E., 2017a. Large bedforms on contourite terraces: Sedimentary and conceptual implications. Geology 46 (1), 27–30. https://doi.org/10.1130/G39655.1.

Hernández-Molina, F.J., Larter, R., Maldonado, A., 2017b. Neogene to Quaternary stratigraphic evolution of the Antarctic Peninsula, Pacific Margin offshore of Adelaide Island: transitions from a non-glacial, through glacially-influenced to a fully glacial stage. Glob. Planet. Chang. 156, 80–111. https://doi.org/10.1016/j.gloplacha.2017.07.002.

Hernández-Molina, F.J., de Castro, S., de Weger, W., Duarte, D., Fonnesu, M., Glazkova, T., Kirby, A., Llave, E., Ng, Z.L., Mantilla Muñoz, O., Rodrigues, S., Rodríguez-Tovar, F.J., Thieblemont, A., Viana, A.R., Yin, S., 2022. Chapter 9 - Contourites and mixed depositional systems: A paradigm for deepwater sedimentary environments. In: Rotzien, Jon R., Yeilding, Cindy A., Sears, Richard A., Hernández-Molina, F. Javier, Catuneanu, Octavian (Eds.), Deepwater Sedimentary Systems. Elsevier, pp. 301–360. https://doi.org/10.1016/B978-0-323-91918-0.00004-9.

Herold, N., Seton, M., Müller, R., You, Y., Huber, M., 2008. Middle Miocene tectonic boundary conditions for use in climate models. Geochem. Geophys. Geosyst. 9, Q10009. https://doi.org/10.1029/2008GC002046.

Herold, N., Huber, M., Müller, R.D., Seton, M., 2012. Modeling the Miocene climatic optimum: ocean circulation. Paleoceanography 27 (1), PA1209. https://doi.org/10.1029/2010PA002041.

Hesse, R., 1975. Turbiditic and non-turbiditic mudstone of Cretaceous flysch sections of the East Alps and other basins. Sedimentology 22, 387–416. https://doi.org/10.1111/j.1365-3091.1975.tb01638.x.

Hodel, F., Grespan, R., de Rafélis, M., Dera, G., Lezin, C., Nardin, E., Rouby, D., Aretz, M., Steinnman, M., Buatier, M., Lacan, F., Jeandel, C., Chavagnac, V., 2021. Drake Passage gateway opening and Antarctic Circumpolar Current onset 31 Ma ago: the message of foraminifera and reconsideration of the Neodymium isotope record. Chem. Geol. Elsevier 570, 120171. https://doi.org/10.1016/j.chemgeo.2021.120171.

Hodell, D.A., Venz-Curtis, K.A., 2006. Late Neogene history of deepwater ventilation in the Southern Ocean. Geochem. Geophys. Geosyst. 7 (9).

Holbourn, A., Kuhnt, W., Kochhann, K.G.D., Andersen, N., Sebastian Meier, K.J., 2015. Global perturbation of the carbon cycle at the onset of the Miocene Climatic Optimum. Geology 43 (2), 123–126.

Houben, A.J.P., Bijl, P.K., Sluijs, A., Schouten, S., Brinkhuis, H., 2019. Late Eocene Southern Ocean cooling and invigoration of circulation preconditioned Antarctica for Full-Scale Glaciation. Geochem. Geophys. Geosyst. 20, 2214–2234.

Hsü, K.J., Ryan, W.B., Cita, M.B., 1973. Late Miocene desiccation of the Mediterranean. Nature 242 (5395), 240–244.

Hüneke, H., Henrich, R., 2011. Chapter 4 - Pelagic Sedimentation in modern and Ancient Oceans. In: Heiko, H., Thierry, M. (Eds.), Deep-Sea Sediments, Developments in Sedimentology, 63. Elsevier, pp. 215–351.

Hüneke, H., Stow, D.A.V., 2008. Identification of ancient contourites: problems and palaeoceanographic significance. In: Rebesco, M., Camerlenghi, A. (Eds.), Contourites. Developments in Sedimentology, 60. Elsevier, Amsterdam, pp. 323–344.

Hüneke, H., Hernández-Molina, F., Rodríguez-Tovar, F., Llave, E., Chiarella, D., Mena, A., Stow, D., 2021. Diagnostic criteria using microfacies for calcareous contourites, turbidites and pelagites in the Eocene-Miocene slope succession, southern Cyprus. Sedimentology. 68 (2), 557–592. https://doi.org/10.1111/sed.12792.

Hüsing, S.K., Zachariasse, W.-J., van Hinsbergen, D.J., Krijgsman, W., Inceöz, M., Harzhauser, M., Mandic, O., Kroh, A., 2009. Oligocene-Miocene basin evolution in SE Anatolia, Turkey: constraints on the closure of the eastern Tethys gateway. Geol. Soc. Lond., Spec. Publ. 311, 107–132. https://doi.org/10.1144/SP311.4.

Ikeda, M., Tada, R., 2013. Long period astronomical cycles from the Triassic to Jurassic bedded chert sequence (Inuyama, Japan), Geologic evidences for the chaotic behavior of solar planets. Earth Planets Space 65, 1–10.

Ito, M., 2002. Kuroshio current-influenced sandy contourites from the Plio-Pleistocene Kazusa forearc basin, Boso Peninsula. Japan. Geol. Soc. London Mem. 22 (1), 421–432. https://doi.org/10.1144/GSL.MEM.2002.022.01.29.

Ivanovic, R.F., Valdes, P.J., Gregoire, L., Flecker, R., Gutjahr, M., 2013. Sensitivity of modern climate to the presence, strength and salinity of Mediterranean-Atlantic exchange in a global general circulation model. Clim. Dyn. 1–19, 2013. https://doi.org/10.1007/s00382-013-1680-5.

Jackson, J., McKenzie, D., 1984. Active tectonics of the Alpine-Himalayan belt between western Turkey and Pakistan. Geophys. J.R Astron. Soc. 77, 185–264.

Jolivet, L., Auguier, R., Robin, C., Suc, J.P., Rouchy, J.M., 2006. Lithospheric-scale geodynamic context of the Messnian salinity crisis. Sediment. Geol. 188-189, 9–33. https://doi.org/10.1016/j.sedgeo.2006.02.004.

Jones, S.M., Lovell, B., Crosby, A.G., 2012. Comparison of modern and geological observations of dynamic support from mantle convection. J. Geol. Soc. 169, 745–758.

Kähler, G., 1994. Stratigraphy and sedimentology of the Lefkara Formation, Cyprus (Paleogene to Early Neogene). University of Southampton. PhD Thesis.

Kähler, G., Stow, D.A.V., 1998. Turbidites and contourites of the Paleogene Lefkara Formation, southern Cyprus. Sediment. Geol. 115, 215–231. Elsevier.

Kamel, M.S., Maiyza, I.A., 2000. On the formation of intermediate & deep water masses in the eastern Mediterranean. Qatar Univ. Sci. J. 20, 197–204.

Karami, M.P., Meijer, P.Th., Dijkstra, H.A., Wortel, M.J.R., 2009. An oceanic box model of the Miocene Mediterranean Sea with emphasis on the effects of closure of the eastern gateway. Paleoceanography 24 (4), PA4023. https://doi.org/10.1029/2008PA001679.

Karami, M.P., De Leeuw, A., Krijgsman, W., et al., 2011. The role of gateways in the evolution of temperature and salinity of semi-enclosed basins: an oceanic box model for the Miocene Mediterranean Sea and Paratethys. Glob. Plan. Change 79 (1–2), 73–88.

Kennett, J., 1982. Marine Geology. Prentice-Hall, Inc., p. 813

Kennett, J.P., Barker, P.F., 1990. Latest Cretaceous to Cenozoic climate and oceanographic developments in the Weddell Sea, Antarctica: an ocean-drilling perspective. Proc. Ocean Drill. Program. Sci. Res. 113, 937–960.

Kinnaird, T.C., 2008. Tectonic and Sedimentary Response to Oblique and Incipient Continental–Continental Collision in the Easternmost Mediterranean (Cyprus). PhD thesis,. University of Edinburgh.

Knutz, P.C., 2008. Palaeoceanographic significance of contourite drifts. In: Rebesco, M., Camerlenghi, A. (Eds.), ContouritesDevelopments in Sedimentology, 60. Elsevier, Amsterdam, pp. 511–535.

Kominz, M.A., Browning, J.V., Miller, K.G., Sugarman, P.J., Mizintseva, S., Scotese, C.R., 2008. Late Cretaceous to Miocene sea-level estimates from the New Jersey and Delaware coastal plain coreholes: an error analysis. Basin Res 20 (2), 211–226.

Krapp, M., Jungclaus, J.H., 2011. The Middle Miocene climate as modelled in an atmosphere–ocean biosphere model. Clim. Past 7, 1169–1188.

Krijgsman, W., Hilgen, F.J., Raffi, I., Sierro, F.J., Wilson, D.S., 1999. Chronology, causes and progression of the Messinian salinity crisis. Nature 400, 652–655. https://doi.org/10.1038/23231.

Lagabrielle, Y., Goddéris, Y., Donnadieu, Y., Malavieille, J., Suarez, M., 2009. The tectonic history of Drake Passage and its possible impacts on global climate. Earth Planet. Sci. Lett. 279 (3–4), 197–211.

Lapierre, H., et al., 2007. The Mamonia Complex (SW Cyprus) revisited: remnant of Late Triassic intraoceanic volcanism along the Tethyan southwestern passive margin. Geol. Mag. 144 (December 2006), 1.

Larter, R.D., Cunningham, A.P., 1993. The depositional pattern and distribution of glacial-interglacial sequences on the Antarctic Peninsula Pacific margin. Mar. Geol. 109, 203–219. https://doi.org/10.1016/0025-3227(93)90061-Y

Laskar, J., Fienga, A., Gastineau, M., Manche, H., 2011. La 2010: a new orbital solution for the long-term motion of the Earth. Astron. Astrophys. 532, A89. https://doi.org/10.1051/0004-6361/201116836.

Lawver, L.A., Gahagan, L.M., 2003. Evolution of Cenozoic seaways in the circum-Antarctic region. Palaeogeogr. Palaeoclimatol. Palaeoecol. 198, 11–37. https://doi.org/10.1016/S0031-0182(03)00392-4.

Lear, C.H., Coxall, H.K., Foster, G.L., Lunt, D.J., Mawbey, E.M., Rosenthal, Y., et al., 2015. Neogene ice volume and ocean temperatures: insights from infaunal foraminiferal Mg/Ca paleothermometry. Paleoceanography 30 (11), 1437–1454.

Lee, I., Ogawa, Y., 1998. Bottom-current deposits in the Miocene-Pliocene Misaki Formation, Izu forearc area, Japan. Island Arc 7, 315–329.

Lee, S.H., Stow, D.A.V., 2007. Laterally contiguous, concave-up basal shear surfaces of submarine landslide deposits (Miocene), southern Cyprus: differential movement of sub-blocks within a single submarine landslide lobe. Geosci. J. 11, 315–321.

Leslie, S.C., Mann, P., 2020. Structure, stratigraphy, and petroleum potential of the deepwater Colombian Basin, offshore northern Colombia. Interpretation 8 (4), ST1–ST14. https://doi.org/10.1190/INT-2020-0028.1.

Leutert, T.J., Auderset, A., Martínez-García, A., Modestou, S., Meckler, A.N., 2020. Coupled Southern Ocean cooling and Antarctic ice sheet expansion during the middle Miocene. Nat. Geosci. 13 (9), 634–639.

Levy, R.H., Dolan, A.M., Escutia, C., Gasson, E.G.H., McKay, R.M., Naish, T., Patterson, M.O., Pérez, L.F.G., Shevenell, A.E., van de Flierdt, T., Dickinson, W., Kowalewski, D.E., Meyers, S.R., Ohneiser, C., Sangiorgi, F., Williams, T., Chorley, H. K., De Santis, L., Florindo, F., Golledge, N.R., Grant, G.R., Halberstadt, A.R.W., Harwood, D.M., Lewis, A.R., Powell, R., Verret, M., 2022. Chapter 9 - Antarctic environmental change and ice sheet evolution through the Miocene to Pliocene – a perspective from the Ross Sea and George V to Wilkes Land Coasts. In: Florindo, Fabio, Siegert, Martin, De Santis, Laura, Naish, Tim (Eds.), Antarctic Climate Evolution (Second Edition). Elsevier, pp. 389–521. https://doi.org/10.1016/B978-0-12-819109-5.00014-1.

Li, H., van Loon, A.J., He, Y., 2020. Cannibalism of contourites by gravity flows: explanation of the facies distribution of the Ordovician Pingliang Formation along the southern margin of the Ordos Basin, China. Can. J. Earth Sci. 57 (3), 331–347. https://doi.org/10.1139/cjes-2018-0225.

Liebrand, D., de Bakker, A.T.M., Beddow, H.M., Wilson, P.A., Bohaty, S.M., Ruessink, G., et al., 2017. Evolution of the early Antarctic ice ages. Proc. Natl. Acad. Sci. 114 (15), 3867–3872.

Liu, S., 2019. Contourite depositional system in the Le Danois Bank region, southern Bay of Biscay: Sedimentary, tectonic and paleoceanographic implications. PhD thesis,. Ghent University, Ghent, Belgium.

Llave, E., Hernández-Molina, F.J., Somoza, L., Díaz-del-Río, V., Stow, D.A.V., Maestro, A., Alveirinho Dias, J.M., 2001. Seismic stacking pattern of the faro-albufeira contourite system (gulf of Cadiz): a quaternary record of paleoceanographic and tectonic influences. Mar. Geophys. Res. 22, 487–508.

Llave, E., Schonfeld, J., Hernández-Molina, F.J., Mulder, T., Somoza, L., del Rio, V.D., Sanchez-Almazo, I., 2006. High-resolution stratigraphy of the Mediterranean

outflow contourite system in the Gulf of Cadiz during the late Pleistocene: the impact of Heinrich event. Mar. Geol. 227, 241–262.
Lonsdale, P., 1981. Drifts and ponds of reworked pelagic sediment in part of the Southwest Pacific. Mar. Geol. 43, 153–193. https://doi.org/10.1016/0025-3227(81)90180-8.
Lonsdale, P., Malfait, B., 1974. Abyssal dunes of foraminiferal sand on the Carnegie Ridge. GSA Bull. 85 (11), 1697–1712. https://doi.org/10.1130/0016-7606(1974)85<1697:ADOFSO>2.0.CO;2.
Lord, A.R., Harrison, R.W., BouDagher-Fadel, M., Stone, B.D., Varol, O., 2009. Miocene mass-transport sediments, Troodos Massif, Cyprus. Proc. Geol. Assoc. 120 (2–3), 133–138. https://doi.org/10.1016/j.pgeola.2009.08.001.
Lourens, L.J., Hilgen, F.J., 1997. Long-periodic variation in the earth's obliquity and their relation to third-order eustatic cycles and late Neogene glaciations. Quat. Int. 40, 43–52.
Lovell, B., 2010. A pulse in the planet: regional control of high-frequency changes in relative sea level by mantle convection. J. Geol. Soc. Lond. 167 (4), 637–648.
Lowe, D.R., 1982. Sediment gravity flows; II, Depositional models with special reference to the deposits of high-density turbidity currents. J. Sediment. Res. 52, 279–297.
Lucchi, R.G., Rebesco, M., 2007. Glacial contourites on the Antarctic Peninsula margin: insight for palaeoenvironmental and palaeoclimatic conditions. In: Viana, A.R., Rebesco, M. (Eds.), Economic and Palaeoceanographic Significance of Contourite Deposits, Geol. Soc. London Spec. Publ., 276, pp. 111–127. https://doi.org/10.1144/GSL.SP.2007.276.01.06.
Lucchi, R.G., Rebesco, M., Camerlenghi, A., Busetti, M., Tomadin, L., Villa, G., Persico, D., Morigi, C., Bonci, M.C., Giorgetti, G., 2002. Mid-late Pleistocene glacimarine sedimentary processes of a high-latitude, deep-sea sediment drift (Antarctic Peninsula Pacific margin). Mar. Geol. 189, 343–370. https://doi.org/10.1016/S0025-3227(02)00470-X.
Maclennan, J., Lovell, B., 2002. Control of regional sea level by surface uplift and subsidence caused by magmatic underplating of earth's crust. Geology 30 (8), 675–678.
Magyar, I., Geary, D.H., Müller, P., 1999. Paleogeographic evolution of the Late Miocene Lake Pannon in Central Europe. Palaeogeogr. Palaeoclimatol. Palaeoecol. 147, 151–167.
Malanotte-Rizzoli, P., Manca, B.B., Ribera d'Alcala, M., Theocharis, A., Brenner, S., Budillon, G., Ozsoy, E., 1999. The Eastern Mediterranean in the 80s and in the 90s: the big transition in the intermediate and deep circulations. Dyn. Atmos. Oceans 29, 365–395. Elsevier. https://doi.org/10.1016/S0377-0265(99)00011-1.
Maldonado, A., Barnolas, A., Bohoyo, F., Galindo-Zaldivar, J., Hernandez-Molina, J., Lobo, F., et al., 2003. Contourite deposits in the central Scotia Sea; the importance of the Antarctic Circumpolar Current and the Weddell Gyre flows Antarctic Cenozoic palaeoenvironments; geologic record and models. ANTOSTRAT Symp. Geol. Record Antarctic Ice Sheet from Drill. Coring Seism. Stud. 198 (1-2), 187–221.
Maldonado, A., Bohoyo, F., Galindo-Zaldívar, J., Hernández-Molina, F.J., Jabaloy, A., Lobo, F., Rodríguez-Fernández, J., Suriñach, E., Vázquez, J.T., 2006. Ocean basins near the Scotia–Antarctic plate boundary: influence of tectonics and paleoceanography on the Cenozoic deposits. Mar. Geophys. Res. 27 (2), 83–107.
Maldonado, A., Bohoyo, F., Galindo-Zaldívar, J., Hernández-Molina, F.J., Lobo, F.J., Lodolo, E., Martos, Y.M., Pérez, L.F., Schreider, A.A., Somoza, L., 2014. A model of oceanic development by ridge jumping: opening of the Scotia Sea. Glob. Planet. Chang. 123, 152–173.
Manzi, V., Lugli, S., Roveri, M., De la Pierre, F., Gennari, R., Lozar, F., Natalicchio, M., Schreiber, B.C., Taviani, M., Turco, E., 2016. The Messinian salinity crisis in Cyprus: a further step towards a new stratigraphic framework for Eastern Mediterranean. Basin Res. 28 (2), 207–236. https://doi.org/10.1111/bre.12107.
Martín-Chivelet, J., Fregenal-Martínez, M.A., Chacón, B., 2003. Mid-depth calcareous contourites in the latest Cretaceous of Caravaca (Subbetic Zone, SE Spain). Origin Paleohydrol. Significe. Sediment. Geol. 163, 131–146.
Martín-Chivelet, J., Fregenal Martínez, M.A., Chacón, B., 2008. Traction structures in contourites. In: Rebesco, M., Camerlenghi, A. (Eds.), Contourites. Developments in Sedimentology, 60. Elsevier, Amsterdam, pp. 159–181.
Martini, E., 1971. Standard Tertiary and Quaternary calcareous nannoplankton zonation. In: Proc. 2 Int. Conf. Plank. Microfoss., Roma, 2, pp. 739–785.
Martorelli, E., Bosman, A., Casalbore, D., Chiocci, F., Conte, A.M., Bella, L.D., Ercilla, G., Falcini, F., Falco, P., Frezza, V., Gaglianone, G., Giaccio, B., Mancini, M., 2021. Mid-to-late Holocene upper slope contourite deposits off Capo Vaticano (Mediterranean Sea): high-resolution record of contourite cyclicity, bottom current variability and sandy facies. Mar. Geol. 431, 106372 https://doi.org/10.1016/j.margeo.2020.106372.
Martos, Y.M., Maldonado, A., Lobo, F.J., Hernández-Molina, F.J., Pérez, L.F., 2013. Tectonics and palaeoceanographic evolution recorded by contourite features in southern Drake Passage (Antarctica). Marine Geol. 343, 76–91.
Mather, B.R., Müller, R.D., Seton, M., Ruttor, S., Nebel, O., Mortimer, N., 2020. Intraplate volcanism triggered by bursts in slab flux. Sci. Adv. 6 (51), eabd0953 https://doi.org/10.1126/sciadv.abd0953.
McCaltum, J.E., 1989. Sedimentation and Tectonics of the Plio-Pleistocene of Cyprus. PhD thesis. University of Edinburgh, p. 263 (unpublished).
McCave, I.N., 2008. Size sorting during transport and deposition of fine sediments: sortable silt and flow speed. Dev. Sedimentol. 60, 121–142.
McCave, I.N., Hall, I.R., 2006. Size sorting in marine muds: Processes, pitfalls, and prospects for paleo-flow speed proxies. Geochem. Geophys. Geosyst. 7, Q10N05. https://doi.org/10.1029/2006GC001284.
McCave, I.N., Tucholke, B.E., 1986. Deep current controlled sedimentation in the western North Atlantic. Geol. Soc. Am M, 451–468.
McCave, I.N., Lonsdale, P.F., Hollister, C.D., Gardner, W.D., 1980. Sediment transport over the Hatton and Gadar contourite drifts. J. Sediment. Petrol. 50, 1049–1062.
McCave, I.N., Thornalley, D.J.R., Hall, I.R., 2017. Relation of sortable silt grain-size to deep-sea current speeds: calibration of the 'Mud Current Meter'. Deep-Sea Res. 127, 1–12. https://doi.org/10.1016/j.dsr.2017.07.003.
McKay, R.M., Escutia, C., De Santis, L., Donda, F., Duncan, B., Gohl, K., Gulick, S., Hernández-Molina, F.J., Hillenbrand, C.-D., Hochmuth, K., Kim, S., Kuhn, G., Larter, R., Leitchenkov, G., Levy, R.H., Naish, T.R., O'Brien, P., Pérez, L.F., Shevenell, A.E., Williams, T., 2022. Chapter 3 - Cenozoic history of Antarctic glaciation and climate from onshore and offshore studies. In: Florindo, F., Siegert, M., De Santis, L., Naish, T. (Eds.), Antarctic Climate Evolution, 2nd Edition. Elsevier, pp. 41–164. https://doi.org/10.1016/B978-0-12-819109-5.00008-6.
Mestdagh, T., 2020. Late Quaternary stratigraphic and sedimentary evolution of the northern Gulf of Cadiz continental margin: New perspectives from shelf-to-slope correlation and borehole-seismic integration. PhD thesis,. Ghent University, Ghent, Belgium.
Mestdagh, T., Lobo, F.J., Llave, E., Hernández-Molina, F.J., van Rooij, D., 2019. Review of the late Quaternary stratigraphy of the northern Gulf of Cadiz continental margin: new insights into controlling factors and global implications. Earth Sci. Rev. 198, 102944.
Meulenkamp, J.E., Sissingh, W., 2003. Tertiary palaeogeography and tectonostratigraphic evolution of the northern and southern Peri-Tethys platforms and the intermediate domains of the African-Eurasian convergent plate boundary zone. Palaeogeogr. Palaeoclimatol. Palaeoecol. 196, 209–228. https://doi.org/10.1016/S0031-0182(03)00319-5.
Miguez-Salas, O., Rodríguez-Tovar, F.J., 2019a. Stable deep-sea macrobenthic trace maker associations in disturbed environments from the Eocene Lefkara Formation, Cyprus. Geobios 52, 37–45.
Miguez-Salas, O., Rodríguez-Tovar, F.J., 2019b. Ichnofacies distribution in the Eocene-Early Miocene Petra Tou Romiou outcrop, Cyprus: sea level dynamics and palaeoenvironmental implications in a contourite environment. Int. J. Earth Sci. 108, 2531–2544. https://doi.org/10.1007/s00531-019-01775-x.
Miguez-Salas, O., Rodríguez-Tovar, F.J., 2021. Ichnofabric analysis as a tool for characterization and differentiation between calcareous contourites and calciturbidites. J. Sediment. Res. 91, 1–15.
Miguez-Salas, O., Rodríguez-Tovar, F.J., Uchman, A., 2019. A new teichichnoid trace fossil Syringomorpha cyprensis from the Miocene of Cyprus. Palaios 34, 506–514.
Miguez-Salas, O., Dorador, J., Rodríguez-Tovar, F.J., Linares, F., 2021. X-ray microtomography analysis to approach bioturbation's influence on minor-scale porosity distribution: a novel approach in contourite deposits. J. Pet. Sci. Eng. https://doi.org/10.1016/j.petrol.2021.109251.
Miguez-Salas, O., Rodríguez-Tovar, F.J., Dorador, J., 2022. Multi-technique comparison to assess the effect of bioturbation on porosity: a study case for reservoir quality in contourites. Facies 68, 11. https://doi.org/10.1007/s10347-022-00650-7.
Miller, K.G., Browning, J.V., Schmelz, W.J., Kopp, R.E., Mountain, G.S., Wright, J.D., 2020. Cenozoic sea-level and cryospheric evolution from deep-sea geochemical and continental margin records. Sci. Adv. 6 (20), eaaz1346. Available from: https://doi.org/10.1126/sciadv.aaz1346.
Millot, C., 1999. Circulation in the Western Mediterranean Sea. J. Mar. Syst. 20 (1–4), 423–442.
Millot, C., 2009. Another description of the Mediterranean Sea outflow. Prog. Oceanogr. 82, 101–124.
Millot, C., Taupier-Letage, I., 2005. Circulation in the Mediterranean Sea. The Mediterranean Sea. In: Handbook of Environmental Chemistry, 5k. Springer, Berlin, pp. 29–66.
Miramontes, E., Jorry, S.J., Jouet, G., Counts, J.W., Courgeon, S., Le Roy, P., Guerin, C., Hernández-Molina, F.J., 2019. Deep marine dunes on drowned isolated carbonate terraces (Mozambique Channel, SW Indian Ocean). Sedimentology 66, 1222–1242.
Miramontes, E., Jouet, G., Thereau, E., Bruno, M., Penven, P., Guerin, C., Le Roy, P., Droz, L., Jorry, S.J., Hernández-Molina, F.J., Thiéblemont, A., Silva Jacinto, R., Cattaneo, A., 2020. The impact of internal waves on upper continental slopes: insights from the Mozambican margin (southwest Indian Ocean). Earth Surf. Process. Landf. 45, 1469–1482. https://doi.org/10.1002/esp.4818.
Miramontes, E., Thiéblemont, A., Babonneau, N., Penven, P., Raisson, F., Droz, L., Jorry, S.J., Fierens, R., Counts, J.W., Wilckens, H., Cattaneo, A., Jouet, G., 2021. Contourite and mixed turbidite-contourite systems in the Mozambique Channel (SW Indian Ocean): link between geometry, sediment characteristics and modelled bottom currents. Mar. Geol. 437, 106502 https://doi.org/10.1016/j.margeo.2021.106502.
Mitchum, R.M., Vail, P.R., Sangree, J.B., 1977. Stratigraphic interpretation of seismic reflection patterns in depositional sequences. In: Payton, C.E. (Ed.), Seismic Stratigraphy-Application to Hydrocarbon Exploration, AAPG Mem, 26, pp. 117–133.
Mjelde, R., Wessel, P., Müller, R.D., 2010. Global pulsations of intraplate magmatism through the Cenozoic. Lithosphere 2 (5), 361–376.
Modestou, S.E., Leutert, T.J., Fernandez, A., Lear, C.H., Meckler, A.N., 2020. Warm middle Miocene Indian Ocean bottom water temperatures: comparison of clumped isotope and Mg/Ca-based estimates. Paleoceanogr. Paleoclimatol. 35 (11), e2020PA003927.
Molina, E., Gonzalvo, C., Keller, G., 1993. The Eocene-Oligocene planktic foraminiferal transition: extinctions, impacts and hiatuses. Geol. Mag. 130 (4), 483–499. https://doi.org/10.1017/S0016756800020550.
Montadert, N., Nicolaides, S., Semb, P.H., Lie, O., 2010. Petroleum systems offshore Cyprus. In: Search and Discovery Article #10279. American Association of Petroleum Geologist Cyprus, Eastern Mediterranean.
Morel, S.W., 1960. The geology and mineral resources of the Apsiou-Akrotiri area. Mem. Geol. Surv. Dept. Cyprus 7, 51–88.
Mulder, T., 2011. Gravity processes and deposits on continental slope, rise and abyssal plains. Deep-sea Sed. 25–148.

Mulder, T., Alexander, J., 2001. The physical character of subaqueous sedimentary density flows and their deposits. Sedimentology 48, 269–299.
Mulder, T., Hüneke, H., 2014. Turbidite. Encyclop. Mar. Geosci. 1–7 https://doi.org/10.1007/978-94-007-6644-0_145-1.
Mullins, H.T., Neumann, A.C., Wilber, R.J., Hine, A.C., Chinburg, S.J., 1980. Carbonate sediment drifts in Northern Straits of Florida. AAPG Bull. 64 (10), 1701–1717. https://doi.org/10.1306/2F9196ED-16CE-11D7-8645000102C1865D.
Mutti, E., 1992. Turbidite Sandstones. Agip, Istituto di Geologia, Università di Parma, p. 275.
Mutti, E., 2011. Turbidites. Search Discovery Article #30214.
Mutti, E., Carminatti, M., 2012. Deep-water sands of the Brazilian offshore basins: search and discovery. In: AAPG Annual Convention & Exhibition.
Mutti, E., Bernoulli, D., Ricci Lucchi, F., Tinterri, R., 2009. Turbidites and turbidity currents from Alpine 'flysch' to the exploration of continental margins. Sedimentology 56 (1), 267–318. https://doi.org/10.1111/j.1365-3091.2008.01019.x.
Mutti, E., Cunha, R., Bulhões, E., Arienti, L., Viana, A., 2014. Contourites and turbidites of the Brazilian Marginal Basins. Search Discovery Article #90189, 43.
Nader, F.H., 2011. The petroleum prospectivity of Lebanon: an overview. J. Pet. Geol. 34 (2), 135–156.
Naish, T.R., Woolfe, K.J., Barrett, P.J., Wilson, G.S., Atkins, C., Bohaty, S., et al., 2001. Orbitally induced oscillations in the East Antarctic ice sheet at the Oligocene/Miocene boundary. Nature 413, 719723.
Newkirk, D.R., Martin, E.E., 2009. Circulation through the Central American Seaway during the Miocene carbonate crash. Geology 37 (1), 87–90.
Ng, Z.L., 2017. Contourites in the Agios Konstantinos and Petra Tou Romiou sections, Lefkara and Pakhna Formations, Cyprus: Conceptual and economic consideration. MSc project. Department of Earth Sciences, Royal Holloway University of London, p. 150.
Ng, Z.L., Hernández-Molina, F.J., Duarte, D., Roque, C., Sierro, F.J., Llave, E., Manar, M. A., 2021. Late Miocene contourite depositional system of the Gulf of Cádiz: the sedimentary signature of the paleo-Mediterranean Outflow Water. Mar. Geol. 106605 https://doi.org/10.1016/j.margeo.2021.106605.
Ng, Z.L., Hernández-Molina, F.J., Ledesma, S., Sierro, F.J., Duarte, D., Llave, E., Roque, C., Arnáiz, A., 2022. Late Miocene evolution of the eastern Deep Algarve basin: interaction of bottom currents and gravitational processes in a foredeep setting. Mar. Pet. Geol. 141, 105695 https://doi.org/10.1016/j.marpetgeo.2022.105695.
Nisancioglu, K.H., Raymo, M.E., Stone, P.H., 2003. Reorganization of Miocene deep water circulation in response to the shoaling of the Central American Seaway. Paleoceanography 18, 1006–1018. https://doi.org/10.1029/2002pa000767.
O'Brien, N.R., Nakazawa, K., Tokuhashi, S., 1980. Use of clay fabric to distinguish Turbiditic and Hemipelagic Siltstones and Silts. In: Stow, D.A.V. (Ed.), Deep-Water Turbidite Systems, 27. Sedimentology, pp. 47–61.
Omta, A.W., Dijkstra, H.A., 2003. A physical mechanism for the Atlantic-Pacific flow reversal in the early Miocene, Global Planet. Change 36, 265–276.
Øvrebø, L.K., Haughton, P.D.W., Shannon, P.M., 2006. A record of fluctuating bottom currents on the slopes west of the Porcupine Bank, offshore Ireland — implications for Late Quaternary climate forcing. Mar. Geol. 225, 279–309.
Papadimitrioua, N., Gorini, C., Nadera, F.H., Deschampsa, R., Symeou, V., Lecomtea, J. C., 2018. Tectono-stratigraphic evolution of the western margin of the Levant Basin (offshore Cyprus). Mar. Pet. Geol. 91, 683–705.
Pearce, J.A., Lippard, S.J., Roberts, S., 1984. Characteristics and tectonic significance of supra-subduction zone ophiolites. In: Kokelaar, B.P., Howells, M.F. (Eds.), Marginal Basin Geology. Geol. Soc. Spec. Publ. London, 16, pp. 74–94.
Pekar, S., DeConto, R.M., 2006. High-resolution ice-volume estimates for the early Miocene: evidence for a dynamic ice sheet in Antarctica. Palaeogeogr. Palaeoclimatol. Palaeoecol. 231, 101109.
Pérez, L.F., Hernández-Molina, F.J., Lodolo, E., Bohoyo, F., Galindo-Zaldívar, J., Maldonado, A., 2019. Oceanographic and climatic consequences of the tectonic evolution of the southern scotia sea basins, Antarctica. Earth Sci. Rev. 198, 102922 https://doi.org/10.1016/j.earscirev.2019.102922.
Pérez, L.F., Martos, Y.M., García, M., Weber, M.E., Raymo, M.E., Williams, T., Bohoyo, F., Armbrecht, L., Bailey, I., Brachfeld, S., Glüder, A., Guitard, M., Gutjahr, M., Hemming, S., Hernández-Almeida, I., Hoem, F.S., Kato, Y., O'Connell, S., Peck, V.L., Reilly, B., Ronge, T.A.S., Tauxe, L., Warnock, J., Zheng, X., 2021. Miocene to present oceanographic variability in the Scotia Sea and Antarctic ice sheets dynamics: insight from revised seismic-stratigraphy following IODP Expedition 382. Earth Planet. Sci. Lett. 553, 116657 https://doi.org/10.1016/j.epsl.2020.116657.
Pérez-Díaz, L., Eagles, G., 2017. South Atlantic paleobathymetry since early cretaceous. Sci. Rep. 7, 11819-16 https://doi.org/10.1038/s41598-017-11959-7.
Peybernes, B., Fondecave-Wallez, M.J., Cugny, P., 2005. Diachronism in the sedimentary cover around the Troodos ophiolitic massif (Cyprus). Bull. Soc. Geol. Fr. 176, 161–169.
Pfuhl, H.A., McCave, I.N., 2005. Evidence for late Oligocene establishment of the Antarctic Circumpolar Current. Earth Planet. Sci. Lett. 235 (3), 715–728.
Pickering, K.T., Hiscott, R.N., 2016. Deep Marine Systems. Processes, Deposits, Environments, Tectonics and Sedimentation. AGU and Wiley, p. 657.
Pickering, K.T., Hiscott, R.N., Hein, F.J., 1989. Deep Marine Environments. Clastic Sedimentation and TectonicsUnwin Hyman Ltd, London.
Piper, D.J.W., Stow, D.A.V., 1991. Fine-grained turbidites. In: Einsele, G., Ricken, W., Seilacher, A. (Eds.), Cycles and Events in Stratigraphy, pp. 360–376.
Popov, S.V., Rögl, F., Rozanov, A.Y., Steininger, F.F., Shcherba, I.G., Kováč, M., 2004. Lithological–Paleogeographic maps of Paratethys. 10. Maps Late Eocene to Pliocene. Courier Forschungsinst. Senckenberg. 250, 1–46.
Popov, S.V., Shcherba, I.G., Ilyina, L.B., Nevesskaya, L.A., Paramonova, N.P., Khondkarian, S.O., Magyar, I., 2006. Late Miocene to Pliocene palaeogeography of the Paratethys and its relation to the Mediterranean. Palaeogeogr. Palaeoclimatol. Palaeoecol. 238, 91–106. https://doi.org/10.1016/j.palaeo.2006.03.020.
Postma, G., 1986. Classification for sediment gravity flow deposits based on flow conditions during sedimentation. Geology 14, 291–294.
Potter, P.E., Szatmari, P., 2009. Global Miocene tectonics and the modern world. Earth Sci. Rev. 96, 279–295.
Praeg, D., Stoker, M.S., Shannon, P.M., Ceramicola, S., Hjelstuen, B., Laberg, J.S., Mathiesen, A., 2005. Episodic Cenozoic tectonism and the development of the NW European "passive" continental margin. Mar. Pet. Geol. 22, 1007–1030.
Pudsey, C.J., Camerlenghi, A., 1998. Glacial-interglacial deposition on a sediment drift on the Pacific margin of the Antarctic Peninsula. Antarct. Sci. 10, 286–308. https://doi.org/10.1017/S0954102098000376.
Rampino, M.R., Caldeira, K., Zhu, Y., 2021. A pulse of the Earth: A 27.5-Myr underlying cycle in coordinated geological events over the last 260 Myr. Geosci. Front. 12, 6, 101245 https://doi.org/10.1016/j.gsf.2021.101245.
Rebesco, M., 2005. Contourites. In: Selley, R.C., Cocks, L.R.M., Plimer, I.R. (Eds.), Encyclopedia of Geology. Elsevier, Oxford, pp. 513–527.
Rebesco, M., Hernández-Molina, F.J., Van Rooij, D., Wåhlin, A., 2014. Contourites and associated sediments controlled by deep-water circulation processes: state of the art and future considerations. Mar. Geol. 352, 111–154. https://doi.org/10.1016/j.margeo.2014.03.011.
Reed, D.L., Meyer, A.W., Silver, E.A., Prasetyo, H., 1987. Contourite sedimentation in an intraoceanic forearc system: eastern Sunda Arc. Indonesia. Mar. Geol. 76, 223–241. https://doi.org/10.1016/0025-3227(87)90031-4.
Reiche, S., Hübscher, C., 2015. The Hecataeus Rise, easternmost Mediterranean: a structural record of Miocene-Quaternary convergence and incipient continentcontinent-collision at the African-Anatolian plate boundary. Mar. Pet. Geol. 67, 368–388. https://doi.org/10.1016/j.marpetgeo.2015.04.021.
Reid, J.L., 1979. On the contribution of the Mediterranean Sea outflow to the Norwegian-Greenland Sea. Deep Sea Res. Part A. Ocean. Res. Pap. 26 (11), 1199–1223.
Renema, W., Bellwood, D.R., Braga, J.C., et al., 2008. Hopping hotspots: global shifts in marine biodiversity. Science 321, 654–657.
Reuter, M., Piller, W., Harzhauser, M., Mandic, O., Berning, B., Rögl, F., Kroh, A., Aubry, M.-P., Wielandt-Schuster, U., Hamedani, A., 2009. The Oligo-/Miocene Qom Formation (Iran): evidence for an early Burdigalian restriction of the Tethyan Seaway and closure of its Iranian gateways. Int. J. Earth Sci. 98, 627–650. https://doi.org/10.1007/s00531-007-0269-9.
Robertson, A.H.F., 1976. Pelagic chalks and calciturbidites from the Lower Tertiary of the Troodos Massif. Cyprus. J. Sediment. Petrol. 46, 1007–1016.
Robertson, A.H.F., 1977. Tertiary uplift history of the Troodos massif. Cyprus. Bull. Geol. Soc. Am. 88, 1763–1772.
Robertson, A.H.F., 1990. Tectonic evolution of Cyprus. In: Malpas, J., Moores, E.M., Panayiotou, A., Xenophontos, C. (Eds.), Ophiolites: Oceanic Crustal Analogues. Proc. Symp. "Troodos 1987," Nicosia, Cyprus, pp. 235–250 (Geol. Surv. Dep., Minist. Agric. Nat. Resour.),.
Robertson, A.H.F., 1998a. Lithofacies evidence for the Cretaceous-paleogene sedimentary history of Eratosthenes seamount, eastern Mediterranean, in its regional tectonic context (sites 966 and 967). Proc. Ocean Drill. Program Sci. Results 160, 403–417.
Robertson, A.H.F., 1998b. Mesozoic-Tertiary tectonic evolution of the easternmost Mediterranean area: integration of marine and land evidence. Proc. Ocean Drilling Program 160, 723–782. https://doi.org/10.2973/odp.proc.sr.160.061.1998.
Robertson, A.H.F., Hudson, J.D., 1974. Pelagic sediments in the Cretaceous and Tertiary history of Cyprus. In: Hsu, K.J., Jenkyns, H.C. (Eds.), Pelagic Sediments: On Land and Under the Sea: Internat. Assoc. Sedimentologists Spec. Pub., 1, pp. 403–436.
Robertson, A.H.F., Woodcock, N.H., 1986. The geological evolution of the Kyrenia Range: a critical lineament in the Eastern Mediterranean. In: Reading, H.G., Watterson, J., White, S.H. (Eds.), Major Crustal Lineaments and their Influence on the Geological History of the Continental Lithosphere. Proc. R. Soc. London Discussion Meeting, A317, pp. 141–178.
Robertson, A.H.F., Xenophontos, C., 1993. Development of concepts concerning the Troodos ophiolite and adjacent units in Cyprus. In: Prichard, H.M., Alabaster, T., Harris, N.B., Neary, C.R. (Eds.), Magmatic Processes and Plate Tectonics. Geol. Soc. Spec. Publ. London, 70, pp. 85–120.
Robertson, A.H.F., Eaton, S., Follows, E.J., McCallum, J.E., 1991. The role of local tectonics versus global sea-level change in the Neogene evolution of the Cyprus active margin. Spec. Publ. Intern. Assoc. Sedimentol. 12, 331–369.
Robertson, A.H.F., Eaton, S., Follows, E.J., Payne, A.S., 1995. Depositional processes and basin analysis of Messinian evaporites in Cyprus. Terra Nova 7, 233–253.
Robertson, A.H.F., Parlak, O., Ustaömer, T., 2012. Overview of the Palaeozoic-Neogene evolution of Neotethys in the Eastern Mediterranean region (southern Turkey, Cyprus, Syria). Pet. Geosci. 18, 381–404.
Robinson, A.R., Golnaraghi, M., Leslie, W.G., Artegiani, A., Hecht, A., Lazzoni, E., Michelato, A., Sansone, E., Theocharis, A., Ünlüata, Ü., 1991. The eastern Mediterranean general circulation: features, structure and variability. Dyn. Atmos. Oceans 15 (3–5), 215–240.
Robinson, A.R., Leslie, W.G., Theocharis, A., Lascaratos, A., 2001. Ocean currents: mediterranean sea circulation. Academic Press. https://doi.org/10.1006/rwos.2001.0376.
Rodrigues, S., Hernández-Molina, F.J., Kirby, A., 2021. A Late Cretaceous mixed (turbidite-contourite) system along the Argentine Margin: paleoceanographic and conceptual implications. Mar. Pet. Geol. 123, 104768 https://doi.org/10.1016/j.marpetgeo.2020.104768.

Rodrigues, S., Hernández-Molina, F.J., Hillenbrand, C.-D., Lucchi, R.G., Rodríguez-Tovar, F.J., Rebesco, M., Larter, R.D., 2022a. Recognizing key sedimentary facies and their distribution in mixed turbidite-contourite systems: the case of the Pacific margin of the Antarctic Peninsula. Sedimentology. https://doi.org/10.1111/sed.12978.

Rodrigues, S., Hernández-Molina, F.J., Fonnesu, M., Miramontes, E., Rebesco, M., Campbell, D.C., 2022b. A new classification system for mixed (turbidite-contourite) depositional systems: examples, conceptual models and diagnostic criteria for modern and ancient records. Earth Sci. Rev. 104030 https://doi.org/10.1016/j.earscirev.2022.104030.

Rodrigues, S., Deptuck, M., Kendell, K., Campbell, C., Hernández-Molina, F.J., 2022c. Cretaceous to Eocene mixed turbidite-contourite systems offshore Nova Scotia (Canada): spatial and temporal variability of down- and along-slope processes. Mar. Pet. Geol. 138, 105572 https://doi.org/10.1016/j.marpetgeo.2022.105572.

Rodríguez-Tovar, F.J., 2014. Orbital climate cycles in the fossil record: from semidiurnal to million-year biotic responses. Annu. Rev. Earth Planet. Sci. 42, 69–102.

Rodríguez-Tovar, F.J., 2022. Ichnological analysis: a tool to characterize deep-marine processes and sediments. Earth Sci. Rev. 238, 104014.

Rodríguez-Tovar, F.J., Hernández-Molina, F.J., 2018. Ichnological analysis of contourites: past, present and future. Earth-Sci. Rev. 182, 28–41.

Rodríguez-Tovar, F.J., Hernández-Molina, F.J., Hüneke, H., Llave, E., Stow, D., 2019a. Contourite facies model: improving contourite characterization based on the ichnological analysis. Sediment. Geol. 384, 60–69. https://doi.org/10.1016/j.sedgeo.2019.03.010.

Rodríguez-Tovar, F.J., Hernández-Molina, F.J., Hüneke, H., Chiarella, D., Llave, E., Mena, A., Miguez-Salas, O., Dorador, J., de Castro, S., Stow, D.A.V., 2019b. Key evidence for distal turbiditic- and bottom-current interactions from tubular turbidite infills. Palaeogeogr. Palaeoclimatol. Palaeoecol. 533, 109233 https://doi.org/10.1016/j.palaeo.2019.109233.

Rodríguez-Tovar, F.J., Miguez-Salas, O., Dorador, J., 2020. Image processing techniques to improve characterization of composite ichnofabrics. Ichnos 27 (3), 258–267.

Rodríguez-Tovar, F.J., Miguez-Salas, O., Dorador, J., 2021. Mercury intrusion porosimetry to evaluate the incidence of bioturbation on porosity of contourites. Riv. Ital. Paleotol. https://doi.org/10.13130/2039-4942/15208.

Rogerson, M., Rohling, E.J., Bigg, G.R., Ramirez, J., 2012. Palaeoceanography of the Atlantic-Mediterranean exchange: overview and first quantitative assessment of climatic forcing. Rev. Geophys. 50, RG2003. https://doi.org/10.1029/2011RG000376.

Rögl, F., 1998. Palaeogeographic considerations for Mediterranean and Paratethys Seaways (Oligocene to Miocene). Ann. Naturhist. Mus. Wien 99A, 279–310.

Rögl, F., 1999. Mediterranean and paratethys. Facts and hypotheses of an Oligocene to Miocene Paleogeography (short overview). Geol. Carpath. 50 (4), 339–349. Bratislava.

Rosenbaum, G., Lister, G.S., Duboz, C., 2002. Reconstruction of the tectonic evolution of the western Mediterranean since the Oligocene. En: Rosenbaum, G. and Lister, G. S. 2002. Reconstruction of the evolution of the Alpine-Himalayan Orogen. J. Virtual Explor. 8, 107–130.

Roveri, M., Flecker, R., Krijgsman, W., Lofi, J., Lugli, S., Manzi, V., Sierro, F.J., Bertini, A., Camerlenghi, A., De Lange, G., Govers, R., Hilgen, F.J., Hübscher, C., Meijer, Pth, Stoica, M., 2014. The Messinian salinity crisis: past and future of a great challenge for marine sciences. Mar. Geol. 352, 25–58. https://doi.org/10.1016/j.margeo.2014.02.002.

Rudge, J.F., Shaw Champion, M.E., White, N., McKenzie, D., Lovell, B., 2008. A plume model of transient diachronous uplift at the earth's surface. Earth Planet. Sci. Lett. 267, 146–160.

Saffer, D.M., Wallace, L.M., Petronotis, K., Barnes, P.B., Bell, R.B., Crundwell, M.C., De Oliveira, C.H.E., Fagereng, A., Fulton, P.F., Greve, A., Harris, R.H., 2018. International ocean discovery program expedition 375 preliminary report: Hikurangi subduction margin coring and observatories unlocking the secrets of slow slip through drilling to sample and monitor the forearc and subducting plate, 8 March-5 May 2018, pp. 1–38.

Salabarnada, A., Escutia, C., Röhl, U., Nelson, C.H., McKay, R., Jiménez-Espejo, F.J., et al., 2018. Paleoceanography and ice sheet variability offshore Wilkes Land, Antarctica - Part 1: insights from late Oligocene astronomically paced contourite sedimentation. Clim. Past 14 (7), 991–1014.

Sangiorgi, F., Bijl, P.K., Passchier, S., Salzmann, U., Schouten, S., McKay, R., et al., 2018. Southern Ocean warming and Wilkes Land ice sheet retreat during the mid-Miocene. Nat. Commun. 9 (1), 317.

Scher, H.D., Martin, E.E., 2006. Timing and climatic consequences of the opening of Drake Passage. Science 312, 428–430.

Scher, H.D., Whittaker, J.M., Williams, S.E., Latimer, J.C., Kordesch, W.E., Delaney, M.L., 2015. Onset of Antarctic circumpolar current 30 million years ago as Tasmanian Gateway aligned with westerlies. Nature 523, 580–583. https://doi.org/10.1038/nature14598.

Schiller, D.M., Seubert, B.W., Musliki, S., Abdullah, M., 1994. The reservoir potential of Globigerina Sands in Indonesia In Indonesian Petroleum Association 23rd Annual Convention Proceedings I, pp. 191–212.

Scotese, C.R., Wright, N.M., 2018. PALEOMAP Paleodigital Elevation Models (PaleoDEMS) for the Phanerozoic. PALEOMAP Project [online] Available from: https://www.earthbyte.org/paleodem-resource-scotese-and-wright-2018.

Shanmugam, G., 2000. 49 years of the turbidite paradigm (1950s-1990s): deep-water processes and facies models a critical perspective. Mar. Pet. Geol. 17, 174–231.

Shanmugam, G., 2006. Deep-Water Processes and Facies Models: Implications for Sandstone Petroleum Reservoirs: 5 (Handbook of Petroleum Exploration and Production). Elsevier Science, p. 496.

Shanmugam, G., 2012. New perspectives on deep-water sandstones: origin, recognition, initiation, and reservoir quality. In: Handbook of Petroleum Exploration and Production, 9. Elsevier, Amsterdam, p. 524.

Shanmugam, G., 2014. Modern internal waves and internal tides along oceanic pycnoclines: challenges and implications for ancient deep- marine baroclinic sands: reply. AAPG Bull. 98, 858–879.

Shanmugam, G., 2017. The contourite problem. In: Mazumder, R. (Ed.), Sediment Provenance. Elsevier, pp. 183–254.

Shanmugam, G., 2019. Slides, slumps, debris flows, turbidity currents, and bottom currents. In: Cochran, J. Kirk, Bokuniewicz, Henry J., Yager, Patricia L. (Eds.), Encyclopedia of Ocean Sciences (Third Edition). Academic Press, pp. 228–257. https://doi.org/10.1016/B978-0-12-409548-9.10884-X.

Shanmugam, G., Spalding, T.D., Rofheart, D.H., 1993a. Process sedimentology and reservoir quality of deep-marine bottom-current reworked sands (sandy contourites): an example from the Gulf of Mexico. Am. Assoc. Pet. Geol. Bull. 77, 1241–1259.

Shanmugam, G., Spalding, T.D., Rofheart, D.H., 1993b. Traction structures in deep-marine bottom-current reworked sands in the Pliocene and Pleistocene, Gulf of Mexico. Geology 21, 929–932.

Shevenell, A.E., Kennett, J.P., Lea, D.W., 2004. Middle Miocene Southern Ocean Cooling and Antarctic Cryosphere Expansion. Science 305 (5691), 1766–1770.

Shevenell, A.E., Kennett, J.P., Lea, D.W., 2008. Middle Miocene ice sheet dynamics, deep-sea temperatures, and carbon cycling: a Southern Ocean perspective. Geochem. Geophys. Geosyst. 9 (2), Q02006.

Shimamura, K., 1995. Where are the terrigenous sediments going in the Japanese Island Arc? In: Tokuyama, H., Shcheka, S.A., Isezaki, N. (Eds.), Geology and Geophysics of the Philippine Sea. Terra Scientific Publishing, Tokyo, pp. 241–249.

Sierro, F.J., Hodell, D.A., Andersen, N., Azibeiro, L.A., Jiménez-Espejo, F.J., Bahr, A., Flores, J.A., Ausin, B., Rogerson, M., Lozano-Luz, R., Lebreiro, S., Hernández-Molina, F.J., 2020. Mediterranean overflow over the last 250 ky. Freshwater forcing from the tropics to the ice sheets. Paleoceanogr. Paleoclimatol. 35, e2020PA003931.

Sijp, W.P., England, M.H., Huber, M., 2011. Effect of the deepening of the Tasman Gateway on the global ocean. Paleoceanography 26 (4), 1–18. Available from: https://doi.org/10.1029/2011PA002143.

Sijp, W.P., von der Heydt, A.S., Dijkstra, H.A., Flögel, S., Douglas, P.M.J., Bijl, P.K., 2014. The role of ocean gateways on cooling climate on long time scales. Glob. Planet. Chang. 119, 1–22.

Smith, A.G., Pickering, K.T., 2003. Oceanic gateways as a critical factor to initiate icehouse Earth. J. Geol. Soc. 160, 337–340.

Sparks, R.S.J., Bonnecaze, R.T., Huppert, H.E., Lister, J.R., Hallworth, M.A., Mader, H., Phillips, J., 1993. Sediment-laden gravity currents with reversing buoyancy. Earth Planet. Sci. Lett. 114 (2–3), 243–257. https://doi.org/10.1016/0012-821X(93)90028-8.

Stampfli, G.M., Borel, G.D., 2002. A plate tectonic model for the Palaeozoic and Mesozoic constrained by dynamic plate boundaries and restored synthetic oceanic isochrones. Earth Planet. Sci. Lett. 169, 17–33.

Stampli, G.M., Borel, G.D., 2002. A plate tectonic model for the Paleozoic and Mesozoic constrained by dynamic plate boundaries and restored synthetic oceanic isochrones. Earth Plan. Sci. Letters 196, 17–33.

Stanley, D.J., 1987. Turbidite to current-reworked sand continuum in Upper Cretaceous rocks, U.S. Virgin Islands. Mar. Geol. 78, 143–151. https://doi.org/10.1016/0025-3227(87)90073-9.

Stanley, D.J., 1988. Turbidites reworked by bottom currents: upper Cretaceous examples from St. Croix, U.S. Virgin Islands. In: Smithsonian Contributions to the Marine Sciences, 33, p. 79. https://doi.org/10.5479/si.01960768.33.

Stanley, D.J., 1993. Model for turbidite-to-contourite continuum and multiple process transport in deep marine settings: examples in the rock record. Sediment. Geol. 82, 241–255.

Steininger, F.F., Wessely, G., 2000. From the Tethyan Ocean to the Paratethys Sea: Oligocene to Neogene Stratigraphy, Paleogeogra- phy and Paleobiogeography of the circum-Mediterranean region and the Oligocene to Neogene Basin evolution in Austria. Mitteilungen der Österreichischen Geologischen Gesellschaft 92, 95–116.

Stickley, C.E., Brinkhuis, H., Schellenberg, S.A., Sluijs, A., Röhl, U., Fuller, M., Grauert, M., Huber, M., Warnaar, J., Williams, G.L., 2004. Timing and nature of the deepening of the Tasmanian Gateway. Paleoceanography 19, PA4027. https://doi.org/10.1029/2004PA001022.

Stow, D.A.V., 1982. Bottom currents and contourites in the North Atlantic. Bulletin de l'Institut Géologique Bassin d'Aquitaine 31, 151–166.

Stow, D.A.V., Faugères, J.C., 2008. Contourite facies and the facies model. In: Rebesco, M., Camerlenghi, A. (Eds.), Contourites. Developments in Sedimentology, 60. Elsevier, Amsterdam, pp. 223–256.

Stow, D.A.V., Holbrook, J.A., 1984. North Atlantic contourites: an overview. In: Stow, D. A.V., Piper, D.J.W. (Eds.), Fine Grained Sediments, Deep-water Processes and Facies. Geological Society, London, Special Publication, 15, pp. 245–256.

Stow, D.A.V., Lovell, J.P.B., 1979. Contourites: their recognition in modern and ancient sediments. Earth-Sci. Rev. 14, 251–291.

Stow, D.A.V., Piper, D.J.W., 1984. Deep-water fine-grained sediments: facies models. In: Stow, D.A.V., Piper, D.J.W. (Eds.), Fine Grained Sediments, Deep-water Processes and Facies. Geological Society, London, Special Publication, 15, pp. 611–646.

Stow, D.A.V., Shanmugam, G., 1980. Sequence of structures in fine-grained turbidites: comparison of recent deep-sea and ancient flysch sediments. Sediment. Geol. 25, 23–42.

Stow, D.A.V., Smillie, Z., 2020. Distinguishing between deep-water sediment facies: turbidites, contourites and hemipelagites. Geoscience 10, 68.

Stow, D.A.V., Tabrez, A.R., 1998. Hemipelagites: processes, facies and model. Geol. Soc. Spec. Publ. 129, 317–337.

Stow, D.A.V., Wetzel, A., 1990. Hemiturbidite: a new type of deep-water sediment. In: Proceedings of the ocean drilling program, scientific results. In: Ocean Drilling Program College Station, TX, 116, pp. 25–34.
Stow, D.A.V., Faugéres, J.C., Howe, J.A., Pudsey, C.J., Viana, A.R., 2002a. Bottom currents, contourites and deepsea sediment drifts: current state-of-the-art. Geo. Soc. London Mem. 22, 7–20.
Stow, D.A.V., Kähler, G., Reeder, M., 2002b. Fossil contourites: type example from an Oligocene palaeoslope system, Cyprus. In: Stow, D.A.V., Pudsey, C.J., Howe, J.A., Faugères, J.-C., Viana, A.R. (Eds.), Deep-water Contourite Systems: Modern Drifts and Ancient Series, Seismic and Sedimentary Characteristics. Geological Society, London, Memoir, 22, pp. 443–455.
Stow, D.A.V., Ogawa, Y., Lee, I.T., Mitsuzawa, K., 2002c. Neogene contourites, Miura-Boso forearc basin, SE Japan. In: Stow, D.A.V., Pudsey, C.J., Howe, J.A., Faugères, J.-C., Viana, A.R. (Eds.), Deep-Water Contourite Systems: Modern Drifts and Ancient Series, Seismic and Sedimentary Characteristics, Geological Society, London, Memoirs, 22, pp. 409–419.
Stow, D.A.V., Hunter, S., Wilkinson, D., Hernández-Molina, F.J., 2008. The nature of contourite deposition. In: Contourites (Eds Rebesco, M. and Camerlenghi, A.), Dev. Sedimentol, 60, pp. 143–156.
Stow, D.A.V., Hernández-Molina, F.J., Llave, E., Sayago-Gil, M., Díaz del Rio, V., Branson, A., 2009. Bedform-velocity matrix: the estimation of bottom current velocity from bedform observations. Geology 37, 327–330. https://doi.org/10.1130/G25259A.1.
Stow, D.A.V., Hernández-Molina, F.J., Llave, E., Bruno, M., García, M., Díaz del Río, V., Somoza, L., Brackenridge, R.E., 2013a. The Cadiz Contourite Channel: sandy contourites, bedforms and dynamic current interaction. Mar. Geol. 343, 99–114.
Stow, D.A.V., Hernández-Molina, F.J., Alvarez Zarikian, C.A., The Expedition 339 Scientists, 2013b. Proceedings IODP, 339. Integrated Ocean Drilling Program Management International, Tokyo. https://doi.org/10.2204/iodp.proc.339.2013.
Straume, E.O., Gaina, C., Medvedev, S., Nisancioglu, K.H., 2020. Global Cenozoic Paleobathymetry with a focus on the Northern Hemisphere Oceanic Gateways. Gondwana Res. 86, 126–143. https://doi.org/10.1016/j.gr.2020.05.011.
Street, C., Bown, P.R., 2000. Palaeobiogeography of Early Cretaceous (Berriasian–Barremian) calcareous nannoplankton. Mar. Micropaleont. 39 (1–4), 265–291.
Super, J.R., Thomas, E., Pagani, M., Huber, M., O'Brien, C., Hull, P.M., 2018. North Atlantic temperature and pCO2 coupling in the early-middle Miocene. Geology 46 (6), 519–522. https://doi.org/10.1130/G40228.1.
Super, J.R., Thomas, E., Pagani, M., Huber, M., O'Brien, C.L., Hull, P.M., 2020. Miocene evolution of North Atlantic sea surface temperature. Paleoceanogr. Paleoclimatol. 35 (5), e2019PA003748.
Sykes, T.J.S., Ramsay, T.S., Kidd, R.B., 1998. Southern hemisphere Miocene bottom-water circulation: a palaeobathymetric analysis. In: Cramp, A., MacLeod, C.J., Lee, S. V., Jones, E.J.W. (Eds.), Geological Evolution of Ocean Basin: Results from the Ocean Drilling Program. Geological Society of London, 131, pp. 43–54.
Symeou, V., Homberg, C., Nader, F.H., Darnault, R., Lecomte, J.-C., Papadimitriou, N., 2018. Longitudinal and temporal evolution of the tectonic style along the Cyprus Arc system, assessed through 2-D reflection seismic interpretation. Tectonics 37, 30–47. https://doi.org/10.1002/2017TC004667.
Takano, O., Itoh, Y., Kusumoto, S., 2013. Variation in Forearc Basin Configuration and Basin-filling Depositional Systems as a Function of Trench Slope Break Development and Strike-Slip Movement: examples from the Cenozoic Ishikari–Sanriku-Oki and Tokai-Oki–Kumano-Nada Forearc Basins, Japan. In: Mechanism of Sedimentary Basin Formation - Multidisciplinary Approach on Active Plate Margins. IntechOpen. https://doi.org/10.5772/56751.
Thieblemont, A., Hernández-Molina, F.J., Miramontes, E., Raisson, F., Penven, P., 2019. Contourite depositional systems along the Mozambique Channel: the interplay between bottom currents and sedimentary processes. Deep-Sea Res. I 147, 79–99. https://doi.org/10.1016/j.dsr.2019.03.012.
Thiéblemont, A., Hernández-Molina, F.J., Ponte, J.-P., Robin, C., Guillocheau, F., Cazzola, C., Raisson, F., 2020. Seismic stratigraphic framework and depositional history for Cretaceous and Cenozoic contourite depositional systems of the Mozambique Channel. SW Indian Ocean. Mar. Geol. 425, 106192 https://doi.org/10.1016/j.margeo.2020.106192.
Thran, A.C., Dutkiewicz, A., Spence, P., Müller, R.D., 2018. Controls on the global distribution of contourite drifts: Insights from an eddy-resolving ocean model. Earth Planet. Sci. Lett. 489, 228–240. https://doi.org/10.1016/j.epsl.2018.02.044.
Torfstein, A., Steinberg, J., 2020. The Oligo–Miocene closure of the Tethys Ocean and evolution of the proto-Mediterranean Sea. Sci. Rep. 10, 13817. https://doi.org/10.1038/s41598-020-70652-4.
Uenzelmann-Neben, G., Weber, T., Grützner, J., Thomas, M., 2017. Transition from the cretaceous ocean to Cenozoic circulation in the western South Atlantic – a twofold reconstruction. Tectonophysics 716, 225–240. https://doi.org/10.1016/j.tecto.2016.05.036.
Underwood, M., Moore, G., 1995. Trenches and Trench-slope basins. In: Busby, C.J., Ingersoll, R.V. (Eds.), Tectonics of Sedimentary Basins. Blackwell Science, Cambridge, Massachusetts, pp. 179–219.
Utescher, T., Bruch, A.A., Micheels, A., Mosbrugger, V., Popova, S., 2011. Cenozoic climate gradients in Eurasia—a palaeo-perspective on future climate change? Palaeogeogr. Palaeoclimatol. Palaeoecol. 304 (3-4), 351–358.
Val, J., Bádenas, B., Aurell, M., 2018. Sedimentary architecture of a prograding oolitic-siliciclastic wedge: Response to changes in wave-base oscillation (Kimmeridgian, Iberian Basin). Mar. Pet. Geol. 96, 113–127. https://doi.org/10.1016/j.marpetgeo.2018.05.03.
van de Lagemaat, S.H.A., Swart, M.L.A., Vaes, B., Kosters, M.E., Boschman, L.M., Burton-Johnson, A., Bijl, P.K., Spakman, W., van Hinsbergen, D.J.J., 2021. Subduction initiation in the Scotia Sea region and opening of the Drake Passage: When and why? Earth Sci. Rev. 215, 103551 https://doi.org/10.1016/j.earscirev.2021.103551.
Van Rooij, D., De Mol, B., Huvenne, V., Ivanov, M.K., Henriet, J.-P., 2003. Seismic evidence of current-controlled sedimentation in the Belgica mound province, upper Porcupine slope, southwest of Ireland. Mar. Geol. 195, 31–53.
Van Rooij, D., Iglesia, J., Hernández-Molina, F.J., Ercilla, G., Gómez-Ballesteros, M., Casas, D., Llave, E., De Hauwere, A., García-Gil, S., Acosta, J., Henriet, J.-P., 2010. The Le Danois Contourite depositional system: interactions between the Mediterranean Outflow Water and the upper Cantabrian slope (North Iberian margin). Mar. Geol. 274, 1–20.
Vence, E., Mann, P., 2020. Subsurface basement, structure, stratigraphy, and timing of regional tectonic events affecting the Guajira margin of northern Colombia. Interpretation 8 (4), ST69–ST105. https://doi.org/10.1190/INT-2020-0016.1.
Vergés, J., Fernàndez, M., 2012. Tethys–Atlantic interaction along the Iberia–Africa plate boundary: the Betic–Rif orogenic system. Tectonophysics 579, 144–172.
Viana, A., 2008. Economic relevance of contourites. In: Rebesco, M., Camerlenghi, A. (Eds.), Contourites. Dev. Sedimentol, 60. Elsevier, Amsterdam, pp. 493–510. https://doi.org/10.1016/S0070-4571(08)10023-1.
Viana, A.R., Faugères, J.C., 1998. Upper slope sand deposits: the example of Campos Basin, a latest Pleistocene-Holocene record of the interaction between along slope and down slope currents. In: Stoker, M.S., Evans, D., Cramp, A. (Eds.), Geological Processes on Continental Margins: Sedimentation, Mass-Wasting and Stability, Geol. Soc. Spec. Publ, 129, pp. 287–316.
Viana, A.R., Faugères, J.-C., Stow, D.A.V., 1998. Bottom current controlled sand deposits – a review of modern shallow- to deep-water environments. Sediment. Geol. 115, 53–80. https://doi.org/10.1016/S0037-0738(97)00087-0.
Viana, A.R., Almeida Jr., W., Nunes, M., Bulhoes, E.M., 2007. The Economic importance of contourites. In: Viana, A.R., Rebesco, M. (Eds.), Economic and Palaeoceanographic Significance of Contourite Deposits, 276. Geol. Soc. London Spec. Publ, pp. 1–23. https://doi.org/10.1144/GSL.SP.2007.276.01.01.
von der Heydt, A., Dijkstra, H.A., 2005. Flow reorganizations in the Panama Seaway: a cause for the demise of Miocene Corals? Geophys. Res. Lett. 32, 15. https://doi.org/10.1029/2004gl020990.
von der Heydt, A., Dijkstra, H.A., 2006. Effect of ocean gateways on the global ocean circulation in the late Oligocene and early Miocene. Paleoceanography 21, PA1011. https://doi.org/10.1029/2005PA001149.
Wade, B.S., Pearson, P.N., Berggren, W.A., Pälike, H., 2011. Review and revision of Cenozoic tropical planktonic foraminiferal biostratigraphy and calibration to the geomagnetic polarity and astronomical time scale. Earth Sci. Rev. 104, 111–142.
Walker, R.G., 1965. The origin and significance of the internal sedimentary structures of turbidites. Proc. Yorks. Geol. Soc. 35, 1–32.
Westerhold, T., Marwan, N., Drury, A.J., Liebrand, D., Agnini, C., Anagnostou, E., et al., 2020. An astronomically dated record of earth's climate and its predictability over the last 66 million years. Science (New York, N.Y.) 369 (6509), 1383–1387. https://doi.org/10.1126/science.aba6853.
Wetzel, A., Werner, F., Stow, D.A.V., 2008. Bioturbation and biogenic sedimentary structures in contourites. In: Rebesco, M., Camerlenghi, A. (Eds.), Contourites. Developments in Sedimentology, 60, pp. 183–202.
White, R.S., McKenzie, D.P., 1989. Magmatism at rift zones: the generation of volcanic continental margins and flood basalts. J. Geophys. Res. 94, 7685–7729.
Whyte, N., Lovell, B., 1997. Measuring the pulse of a plume with the sedimentary record. Lett. Nat. 387, 888–891.
Wright, R., Anderson, J.B., 1982. The importance of sediment gravity flow to sediment transport and sorting in a glacial marine environment: Eastern Weddell Sea. Antarctica. GSA Bull. 93, 951–963. https://doi.org/10.1130/0016-7606(1982)93<951:TIOSGF>2.0.CO;2.
Wüst, G., 1961. On the vertical circulation of the Mediterranean Sea. Deep-Sea Res., 16; 171-178. In: Kamel, M.S. & Maiyza, I.A. 2000. On the formation of intermediate & deep water masses in the eastern Mediterranean. Qatar Univ. Sci. J. 20, 197–204.
You, Y., 2010. Climate-model evaluation of the contribution of sea-surface temperature and carbon dioxide to the Middle Miocene Climate Optimum as a possible analogue of future climate change. Austral. J. Earth Sci. Intern. Geosci. J. Geol. Soc. Austral. 57 (2), 207–219.
Yu, X., Stow, D.A.V., Smillie, Z., Esentia, I., Brackenridge, R.E., Xie, X., Bankole, S., Ducassou, E., Llave, E., 2020. Contourite porosity, grain size and reservoir characteristics. Mar. Pet. Geol. 117, 104392.
Zachos, J., Pagani, H., Sloan, L., Thomas, E., Billups, K., 2001. Trends, rhythms, and aberrations in global climate 65 Ma to present. Science 292, 686–693.
Zachos, J., Dickens, G., Zeebe, R., 2008. An early Cenozoic perspective on greenhouse warming and carbon-cycle dynamics. Nature 451, 279283. Available from: https://doi.org/10.1038/nature06588.
Zhang, L.F., Dong, D.Z., 2020. Thickening-upward cycles in deep-marine and deep-lacustrine turbidite lobes: examples from the Clare Basin and the Ordos Basin. J. Palaeogeogr. 9, 11. https://doi.org/10.1186/s42501-020-00059-9.
Zhang, Y.G., Pagani, M., Liu, Z., Bohaty, S.M., DeConto, R., 2013. A 40-million-year history of atmospheric CO2. Phil. Trans. R. Soc. A 371, 20130096. Available from: https://doi.org/10.1098/rsta.2013.0096.
Zhang, X., Zhang, T., Lei, B., Zhang, J., Yong, J., 2020. A giant sandy sediment drift in early Silurian (Telychian) and its multiple sedimentological process. Mar. Pet. Geol. 113, 1040.